UNIVERSITÀ DEGLI STUDI DI PADOVA

Dipartimento di Fisica e Astronomia "Galileo Galilei"

Master Degree in Astrophysics and Cosmology

Final Dissertation

Modelling of the broad band emission of the AGN PG 1553+113

Thesis supervisor
Dr.Elisa Prandini
Thesis co-supervisor
Dr. Davide Miceli
Dr. Axel Arbet Engels

Candidate
Giuseppe Silvestri

Academic Year 2022/2023

Abstract

Aims. The BL Lac PG 1553+113 is known for its high variability and exhibits periodic behaviour with a 2.2-year cycle, showing a significant 3-sigma significance in its Fermi gamma emission. This periodicity is characterized by a simultaneous flaring state at all energy levels. This thesis focuses on reporting the 2019 flare of PG 1553+113, analysing multiwavelength data, and modelling the emission from this source.

Methods. Data from multiple instruments, ranging from radio to gamma-rays, were analysed with a specific emphasis on the highest energies, such as the MAGIC telescopes. Subsequently, the emission of PG 1553+113 was divided into a flaring state (April 2019) and enhanced state (June-August 2019) and then modelled using the `agnpy` software.

Results and findings. During this project, multiple models were applied to analyse this source. Initially, a one-zone Synchrotron-Self Compton (SSC) model was utilized; however, evidence from correlation studies and the emission shape suggested a preference for a two-zone SSC model. The new model exhibits a good agreement with the dataset, and its application to PG 1553+113 represents a novel contribution in this work. The two-zone model found in this work does not explain the weak correlation between HE and the other energy bands. New types of models will be tested in the future.

Summary

This work of thesis, titled "modelling of the broad band emission of the AGN PG 1553+113", regards the multi-frequency data analysis and interpretation of the emission from the bright active galactic nucleus PG 1553+113.

In *Chapter 1*, I firstly introduced AGNs, describing their structure and classification, and then I focused on the blazar category, giving a detailed description of their physical properties. After this I proceeded with a brief description of cosmic rays and neutrino astronomy, due to the relevance that blazars have in the emerging field of multimessenger astronomy, being one of the most suitable candidates for high energy cosmic rays production. I then described the production of non-thermal radiation, ranging from the radio band up to γ-rays, emitted by blazars, and presented in detail both hadronic and leptonic processes. Moreover I characterized the broad band emission by giving an explanation of the physical parameters of a blazar spectral energy distribution. Furthermore I gave an observational overview on the instruments and techniques used to detect γ-ray from blazars. Lastly, I described the source main subject of this work, named PG 1553+113, a BL Lac object.

In *Chapter 2*, I proceeded with a very detailed description of the MAGIC telescopes and how they work. I started with a characterization of the technical components of the two IACTs going from the mirror up to the readout electronics and trigger system. Then I characterized MAGIC software components, safety conditions for observations and pointing configurations. Afterwards I went into detail regarding MAGIC standard analysis, describing how from the information measured by the telescopes it is possible to reconstruct the energy, direction and nature of the primary particle, and from these parameters, generate physical high-level analysis outputs, like lightcurves and spectra.

In *Chapter 3*, I described the standard MAGIC analysis that I have performed on PG 1553+113. Going from intermediate up to the high level results. In particular I have shown lightcurves, SEDs, θ^2 plots and skymaps obtained from two observational periods (2019-2020) that I've analyzed.

Chapter 4 is dedicated to the multiwavelength analysis performed on PG 1553+113 observations during 2019. I described each energy band and the relative instrument that has been used in this work going from VHE γ-ray to the radio band. Furthermore at each band I showed the results obtained from the available datasets. In the end I show a comparison between the lightcurves at each energy, giving a description of the properties of the broad band PG 1553+113 emission during 2019.

Chapter 5 is focused on the modelling that has been performed on the source emission. I

started with the characterization of two different states of PG 1553+113 in 2019: flaring and enhanced. This division has been performed based on temporal and intensity properties of the source flux. Then I proceeded with the description of `agnpy`, the software that I've used to model the spectral energy distribution and perform the fits, focusing on the different modules that compose it. After this, I started applying different models to the broad band spectral energy distributions of both flaring and enhanced state. Beginning with the one-zone syncrothron self compton model I show the results of the fit and the parameters that I've used to describe the electron energy distribution. Through correlation studies, I find that the one-zone model is not the best choice in order to describe the emission of PG 1553+113. So I proceeded with a two-zone syncrothron self compton model, and even as it was previously done, and I showed its results and downsides. Lastly I tested the wobbling jet to explain the source periodicity.

In *Chapter 6* I discussed the standard MAGIC analysis that I have performed on the observation of PG 1553+113 from June 2022 up to June 2023. Then I showed the high level results of my analysis.

The final chapter topic is an overview of the conclusions of my work and includes an outlook that will guide my future studies on this source.

Contents

Chapter 1

Introduction

1.1 AGNs

Active Galactic Nuclei, AGNs for short, are structures located at the center of most galaxies, typically composed of:

- Supermassive black hole, with masses between ($10^6\,M_\odot \leq M_{BH} \leq 10^{10}\,M_\odot$), that most likely is rotating;
- an accretion disk of matter that is gravitationally attracted to the central black hole and spiraling around it;
- an X-ray corona, whose origin is still unclear, likely a hot layer or an ensemble of very active clusterized regions in the inner part of the accretion disk. The X-ray corona is divided in half by the disk;
- a dusty torus, located at several parsecs from the black hole, it blocks the radiation coming from the center and it re-emits it in the infrared;
- Broad Line Region (BLR), a zone with small clouds that at $\sim 10^{12} - 10^{15}\,\mathrm{Km}$ from the center characterized by their high speed ($\sim 3000\,\frac{Km}{s}$). These clouds block part of the incoming ionizing radiation and then emit lines that are Doppler shifted;
- Narrow Line Region (NLR), a zone with less dense clouds than BLR and located further from the central black hole ($\sim 100\,\mathrm{pc}$);
- $\sim$ 10% of AGNs emits a jet of ultrarelativistic particles in two opposite directions;

From several physical properties (e.g. variability, emission lines, spectral features) AGNs can be classified as:

- **Seyfert Galaxies**, characterized by low luminosity and strong emission lines, the latter are due to the coupling between highly ionized gas and high-energy radiation. They're divided into Seyfert I or II depending on the angle at which we see them;
- **Quasars**, very luminous point-like objects located at very high redshifts;
- **Blazars**, jetted AGNs that show extreme variability. The direction of the jet has a small angle compared to our line of sight;
- **Radio Galaxies**, jetted AGNs with large angles with respect to the observer and with the peculiarity of having a strong emission in the radio band due to the interaction of high-energy particles with magnetic fields. Depending on their morphology they're further divided into Faranoff-Ryley type I and type II.

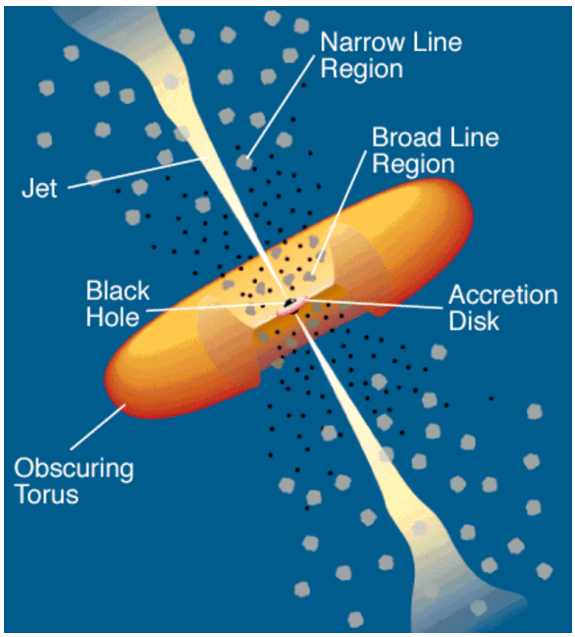

Figure 1.1: Structure of a jetted AGN. The supermassive black hole, with an accretion disk of hot material, then there is the Broad Line region and further out the Narrow Line region. Far away from the center there's the obscuring torus and in the perpendicular direction there's the jet of ultrarelativistic particles. Image from (Urry and Padovani, 1995).

The AGN population is composed of different types of sources. This characterization can be explained with the so called Unification model of AGNs, proposed for the first time in (Urry and Padovani, 1995). It says that differences among the AGN population can be described by a difference in the viewing angle, so for example radio galaxies are the same type of object as blazars, but the angle at which we see the former is greater than the one for blazars.
The difference though does not lay just on the viewing angle but also on the strength of the jet that for example in Seyfert galaxies is less than for quasars or blazars.

1.1.1 Blazars

Blazars are sources that point their jet towards us. A way of classifying them is to use a quantity called equivalent width of a line (EW) with units of Angstrom () and defined as:

$$EW = \int \frac{F_0 - F_\lambda}{F_0} d\lambda \tag{1.1}$$

with F_λ being the flux of the continuum and that of the line, while F_0 is the flux of just the continuum. After having defined this quantity, the classification of blazars is:

- BL Lacs, if they have very weak lines $EW < 5$;
- Flat Spectrum Radio Quasars (FSRQs), if they have strong emission lines $EW > 5$.

Their spectral energy distributions (SED), i.e. the flux of energy density, have the same double-peaked shape. The first hump has a position that is around $\sim 10^{12} - 10^{15}\, Hz$ and it is due to synchrotron emission by the electrons in the jet.
The second peak is located at higher frequencies $\sim 10^{21} - 10^{25}\, Hz$ and its origin is still not certain, it can be due to leptonic processes like Inverse Compton between the synchrotron

electrons and either the same synchrotron photons (synchrotron-Self Compton) or the photons from the emission lines (External Compton), or it could be caused by hadronic processes like proton synchrotron or photoproduction.

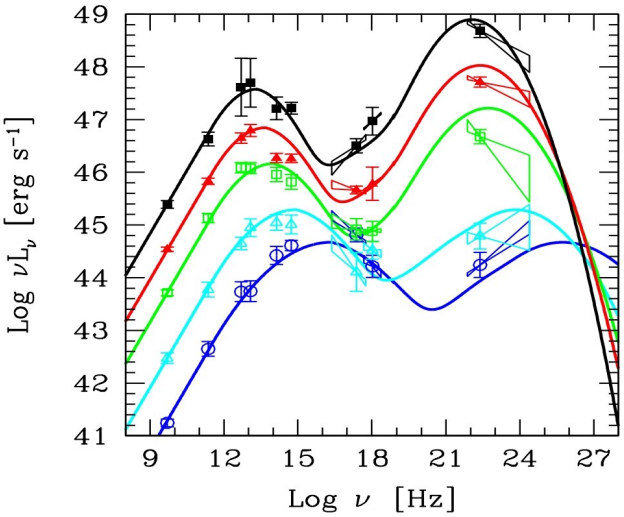

Figure 1.2: Blazar sequence, image from (Donato, D. et al., 2001; Fossati et al., 1998). From top to bottom, the first three (black, red and green) are SEDs from FSRQs while the last two (light blue and blue) are typical SEDs of a BL Lac

An important plot that displays the similarities and the differences between FSRQs and BL Lacs SEDs is called Blazar sequence, and is shown in Fig. 1.2, the first two SEDs from top to bottom are from FSRQs while the last three in light blue and blue are from BL Lacs. They're both double peaked, but while BL Lacs' are even for Flat spectra's there's a difference in height of 1 or 2 orders of magnitude and the bolometric luminosity is higher. For BL Lacs the peaks are located at higher frequencies while it's the opposite for FSRQs. From the position of the synchrotron peak of BL Lacs, they are classified as:

- Low synchrotron peak BL Lacs (LSPs), if $\nu_{syncr}^{peak} < 10^{14}\,Hz$;
- Intermediate synchrotron peak BL Lacs (ISPs), if $10^{14}\,Hz < \nu_{syncr}^{peak} < 10^{15}\,Hz$;
- High synchrotron peak BL Lacs (HSPs), if $10^{15}\,Hz < \nu_{syncr}^{peak} < 10^{17}\,Hz$;
- Extremely high synchrotron peak BL Lacs (HSPs), if $10^{17}\,Hz < \nu_{syncr}^{peak}$.

1.2 Cosmic-rays and Multimessenger astrophysics

Cosmic rays (CRs) are energetic particles composed mainly of protons, helium nuclei, electrons and heavier nuclei, the latter two are in small amount though.
They were first discovered by Victor Hess in 1912 (Hess, 1912) with a balloon experiment, finding that the source of this radiation did not originate from the Earth but instead had extraterrestrial origins. CRs are divided into two categories: primary and secondary. The former are the ones directly produced by the sources and the latter are the byproducts of the interaction between primary CRs and Earth's atmosphere.
Secondary CRs are part of Extensive Air Shower (EAS), due to the fact that the primary particle is highly energetic so the products of its collision with the atmosphere can then further interact with the medium generating a cascade.
Auger demonstrated in 1939 (Auger et al., 1939) that the dimensions of these EAS can be

greater than 100m.
The CR's spectrum ranges between $10^9 eV$ up to $10^{21} eV$, it is considered to start at GeV energies because below this threshold we get the so called solar modulation, the magnetic field produced by the Sun deflects the CRs meaning that we observe only the particles ejected by our star. The spectrum locally follows a power-law shape

$$\frac{dN}{dE} \propto E^{-\alpha} \tag{1.2}$$

with α varying depending on the E range, meaning that there are different processes responsible for its production at different energy ranges. From GeV to $E \sim 10^{15} eV$ $\alpha \simeq 2.7$, then we have a break in the spectrum, called the knee, whose origin is still largely debated i. Then up to $E \sim 10^{18} eV$ we have a spectral index of $\simeq 3.1$ and we reach the ankle, a second break due to the transition from galactic to extragalactic origin. From it and $E \sim 10^{19} eV$ the index is ~ 2.6, then we have the so called Greisen, Zatsepin, Kuzmin (GZK) cut-off due to the interaction between CRs and the cosmic microwave background. Fig reports the most recent map of the CR flux above 41 EeV produced by the Auger collaboration.

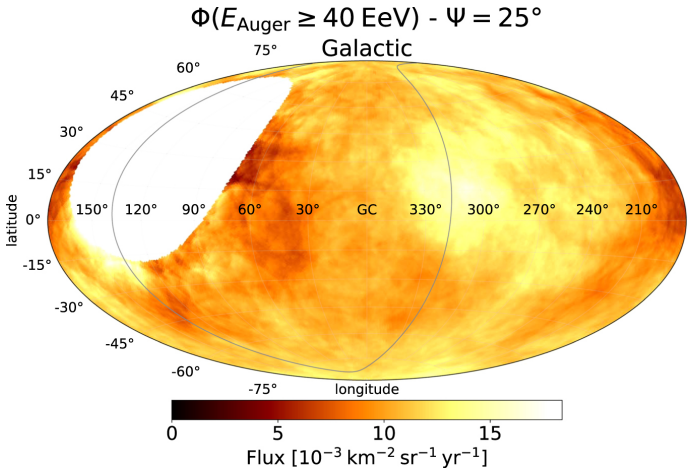

Figure 1.3: Li-Ma significance map at energies above 41 EeV, shown in galactic coordinates from (Abreu et al., 2022)

During the last decades cosmic ray studies have become more and more important, in particular due to a multimessenger approach to possible candidates as CR sources. Neutral mediators such as γ-rays, neutrinos and gravitational waves are key messenger for this purpose.

1.2.1 Neutrinos

Neutrinos are particles first theorized by Pauli in 1930 to explain the continuum energy spectrum of the β decay. The difficulty in their detection arises from the fact that their main type of interaction is the weak one. The first neutrino, emitted in a nuclear reactor, was observed 26 years after their theorization (Cowan et al., 1956), while in 1965 and 1968 were observed respectively the first atmospheric and solar neutrinos. Currently to observe astrophysical neutrinos there's the IceCube observatory, operating since 2011, located in the South Pole, and composed of an array of photomultipliers in 1 km^3 of pure ice to compensate for the small cross sections of neutrino interactions. In 2018 there was the first detection of an astrophysical neutrino from the source TXS 0506+056 (Aartsen et al., 2018) as shown in Fig. 1.4

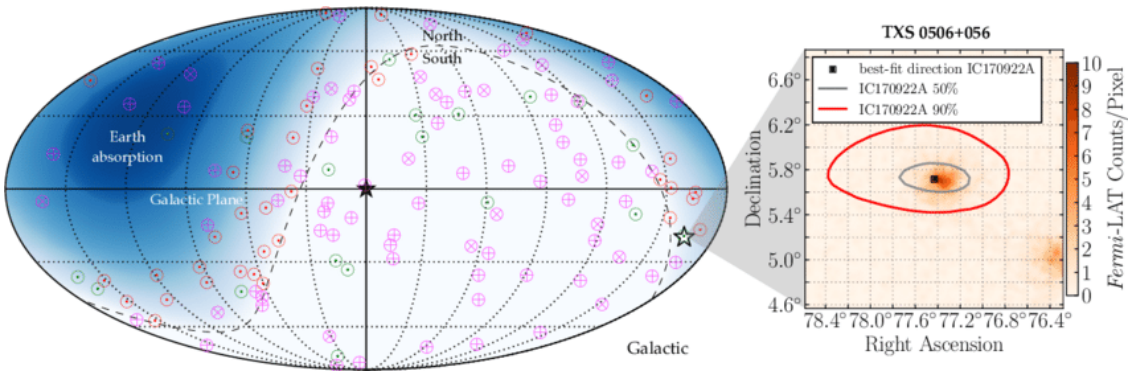

Figure 1.4: Neutrino map, from (Aartsen et al., 2019)

In the next years there will be not only an upgrade of Ice Cube called Ice Cube Gen 2, but even the operation of new astrophysical neutrino detectors like K3MNet.

1.3 Broad Band emission from Blazars

1.3.1 Production of non-thermal elctromagnetic radiation

The production of non-thermal electromagnetic radiation in a blazar is divided into 2 categories depending on the particles involved in the process:

- Leptonic;
- Hadronic;

Typical leptonic processes are Inverse Compton (IC), bremmstrahlung and synchrotron emission (Rybicki and Lightman, 1979), while hadronic ones are pion decay, proton syncroton emission, and photoproduction ((Mannheim and Biermann, 1992), (Mannheim, 1993), (Rachen and Mészáros, 1998), (Aharonian, 2000)).

Leptonic processes

Sychrotron radiation

It is the radiation emitted by a charged relativistic particle moving in a magnetic field. In this case the motion of a relatistic particle can be written as:

$$\frac{d\left(m\gamma\vec{v}\right)}{dt} = \frac{q\vec{v}\times\vec{B}}{c} \tag{1.3}$$

and having null electric field

$$\frac{d\left(m\gamma c^2\right)}{dt} = q\vec{v}\cdot\vec{E} = 0 \tag{1.4}$$

Eq. 3 implies that γ is a constant so eq. 2 can be rewritten as:

$$m\gamma\frac{d\vec{v}}{dt} = \frac{q\vec{v}\times\vec{B}}{c} \tag{1.5}$$

Decomposing the velocity vector into its parallel and perpendicular components with respect to the magnetic field, then two equations are formed:

$$\frac{d\vec{v_\perp}}{dt} = \frac{q\vec{v} \times \vec{B}}{cm\gamma} \tag{1.6}$$

$$\frac{dv_\parallel}{dt} = 0 \tag{1.7}$$

So these two equations imply that the parallel component of the velocity vector is constant, and the module of the perpendicular component is constant too, resulting in an helicoidal motion of the particle as shown in Fig. 1.5.
The frequency of this rotation is given by:

$$\omega_B = \frac{qB}{m\gamma c} \tag{1.8}$$

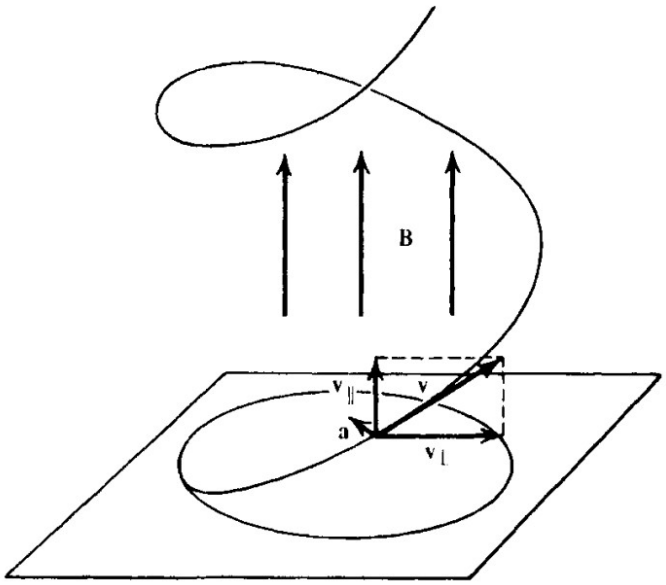

Figure 1.5: Helicoidal trajectory of a relativistic charged particle in a magnetic field from (Rybicki and Lightman, 1979)

After some calculations the total emitted power is found to be:

$$P = \frac{4}{3}\sigma_T \beta^2 \gamma^2 U_B \tag{1.9}$$

with U_B being the magnetic energy density $U_B = \frac{B^2}{8\pi}$ and σ_T is the Thompson cross section $\sigma_T = \frac{8}{3}\pi r_o^2$.

Bremmstrahlung

From German language, meaning "braking radiation", it is the emission from a charged particle either accelerating or decelerating in an electric field, usually due to the interaction with another particle or an atomic nucleus. As the charged particle changes its velocity, it emits photons.
The total power emitted per unit frequency by the charged particle is give by:

$$P(\omega) = \frac{2}{3}\frac{a^2 q^2}{c^3}\frac{\omega^2}{4\pi c} \tag{1.10}$$

with a being the acceleration of the particle, q its charge and ω its angular frequency.
The number of photon per unit frequency, called differential energy spectrum, is instead given by the Bethe-Heitler formula:

$$\frac{dN}{d\omega} = \frac{16Z^2\alpha r_e m_e c}{3\pi}\left[\frac{1-\beta^2}{\beta}\right]\left[\frac{ln(\gamma^2) - ln(\frac{1}{\omega^2}) + \frac{1}{3}}{\omega}\right] \tag{1.11}$$

with Z being the atomic number of the target, α the fine-structure constant, r_e classical electron radius, m_e classical electron mass, β is the velocity of the electron divided by the speed of light, γ is the Lorentz factor.The second factor represents the relativistic effect, while the third factor is the screening effect of the atomic nucleus by the orbiting electrons.

Inverse Compton
It is the scattering phenomenon between an electron and a photon, and due to momentum conservation the photon gains more energy. The variation of the photon energy in the rest frame can be considered negligible with respect to the one in the comoving frame, then the power gained by the photon is:

$$P_{compton} = \frac{dE_{rad}}{dt} = \frac{4}{3}c\sigma_T\beta^2\gamma^2 U_{ph} \tag{1.12}$$

with $\beta = \frac{v}{c}$ and U_{ph} is the photon energy density.
The cross section of the process is dependent on the ratio between the photon's energy and electron's rest mass energy, such that:

$$\sigma_{IC} = \sigma_{Thomson} = \frac{8}{3}\pi r_e^2 \tag{1.13}$$

in the Thompson regime ($\frac{h\nu}{m_e c^2} << 1$), and

$$\sigma_{IC} = \frac{m_e c^2}{h\nu}\pi r_e^2\left(\ln\frac{2h\nu}{m_e c^2} + 0.5\right) \tag{1.14}$$

in the Klein-Nishima regime ($\frac{h\nu}{m_e c^2} >> 1$).

Hadronic Processes

Photoproduction

Photoproduction is a process where a high-energy photon interacts with a target particle or nucleus, modifying or creating particles. It happens when the photon transfers energy and momentum to the target. This process is described by the conservation of energy and momentum, so:

$$E_i + E_\gamma = E_f + E_{part} \tag{1.15}$$

with E_i being the initial energy of the system, E_γ that of the photon, E_f is the energy of the system after the collision and E_{part} is that of the newly produced particles.
While for the conservation of momentum:

$$p_i + p_\gamma = p_f + p_{part} \tag{1.16}$$

with p_i being the initial energy of the system, p_γ that of the photon, p_f is the energy of the system after the collision and p_{part} is that of the newly produced particles.

Another outcome of photoproduction is the excitation of a target particle or nucleus. When a photon is absorbed by a nucleus, it can impart enough energy to raise the nucleus to an excited state. This excitation process provides valuable information about the structure and properties of atomic nuclei.

Neutral pion decay

Neutral piondecay (Fig. 1.6) is a process during which a neutral pion (π_0) decays mostly into a pair of photons due to its lack of electric charge.

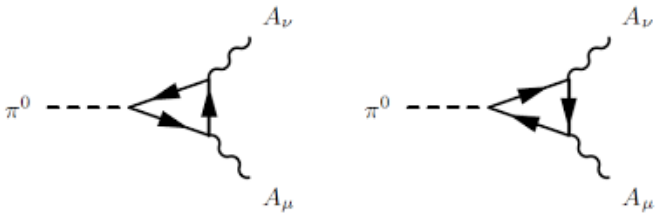

Figure 1.6: Feymann diagrams of the neutral pion decay

The neutral pion decay into photons occurs through the interaction of the pion's electric charge distribution with the electromagnetic field. In the decay process, the energy and momentum of the initial neutral pion are distributed between the two photons according to conservation laws. The π_0 can't directly decay into two photons because it doesn't posses any electrical charge, thus the neutral pions must undergo a strong decay to charged mesons or baryon-antibaryon pair.

1.3.2 Broad Band emission of Blazars and important parameters

As shown in Fig. 1.1 the typical emission from both blazar subcategories is characterized by a two peaked shape that ranges from radio up to γ-rays. In this kind of sources, the jet emission is largely amplified by relativistic effects due to the small angle to the observer, and outshines all the other emitting components.
The emission within the first peak is due to electron synchrotron radiation, i.e. electrons spiraling in the magnetic field of the jet. For FSRQs, there are ofthen additional components (BLRs, accretion disk, torus).
The second peak instead is usually explained with the IC process, in particular for BL Lacs a synchrotron-Self Compton model seems to describe better the observations. According to this model, synchrotron photons are scattered to higher energies by the electrons themselves. For FSRQs, the typical model is the External Compton, electrons scatter photons from an external photon field, for example the BLRs.

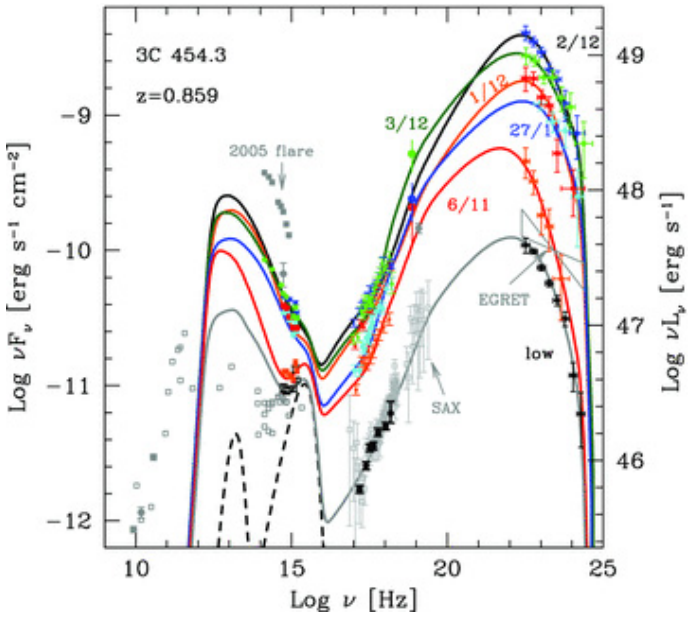

Figure 1.7: Daily SED of the blazar 3C454.3 from (Bonnoli et al., 2010)

A property of the broad band emission of blazars is, as shown in Fig. 1.7, the high variability of the SED, that can range from minutes up to years. This phenomenon is amplified by the so called Doppler factor δ_D. Applying simply special relativity to the emission from the jet is not enough, if photons are used to determine time intervals then it must be taken into account the fact that the first and the last photon are emitted in two different places. Normally in special relativity, so without considering photons, time dilation is given by $\Delta t_{obs} = \Gamma \Delta t'_e$ with Δt_{obs} being the observed time interval, $\Delta t'_e$ is the one in the source rest frame and Γ is the bulk Lorentz factor. Instead if time intervals are measured with photons it is found that:

$$\Delta t_{obs} = \Delta t_e - \beta\, cos\theta\, \Delta t_e = \Delta t_e(1 - \beta\, cos\theta) = \Gamma \Delta t'_e(1 - \beta\, cos\theta) = \frac{\Delta t'_e}{\delta_D} \tag{1.17}$$

with Δ_e being the emitted time interval in the laboratory rest frame, θ is the angle between the jet direction and our line of sight, while $\boldsymbol{\delta_D}$ is the **Doppler factor**, that is defined as:

$$\delta_D = \frac{1}{\Gamma(1 - \beta\, cos\theta)} \tag{1.18}$$

Thanks to this factor, with typical values ranging from 10 up to 60, the jet emission dominates over the other component and is highly variable.
Another important parameter for blazar γ-ray emission is their distance, usually computed in terms of **redshifts z**, that relates with the distance of the source with a first approximation using the Hubble law:

$$z = \frac{dH_0}{c} \tag{1.19}$$

with d being the comoving distance of the source, c the speed of light and H_0 is the current value of Hubble constant, that is $H_0 \simeq 68 km\, s^{-1}\, Mpc^{-1}$. It is very useful for understanding the VHE emission from a source because photons at hundreds of GeV undergo pair production with other photons from the Extragalactic Background Light (EBL). It is the optical and IR light emitted throughout the history of the universe mostly by galaxies, and the second most intense background of electromagnetic radiation, second only to the Cosmic Microwave Background light (CMB) as shown in Fig. 1.8.

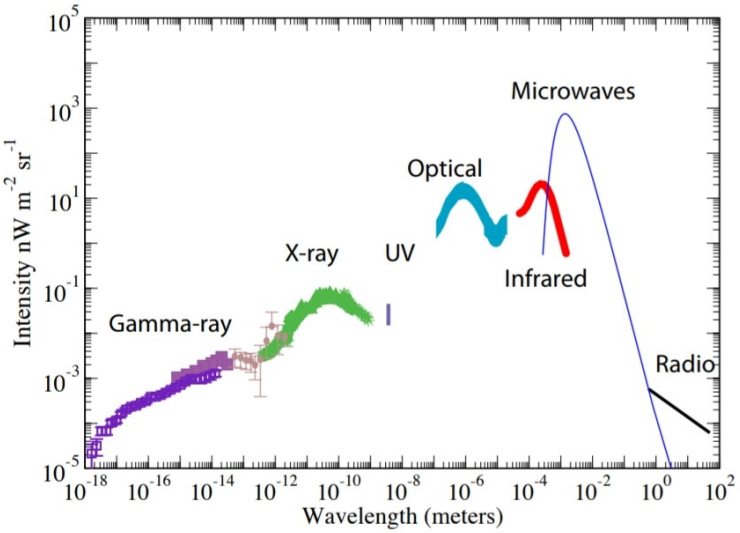

Figure 1.8: Electromagnetic background spectrum. Image taken from (Cooray, 2016)

Its interaction with VHE γ-rays reduces the flux emitted by a source by a quantity that is:

$$\frac{dN_{obs}}{dE} = \frac{dN_{emi}}{dE} e^{-\tau(E,z)} \tag{1.20}$$

with $\frac{dN_{obs}}{dE}$ being the observed flux, $\frac{dN_{emi}}{dE}$ is the one emitted by the source and τ is the absorption factor, that is both energy and redshift dependent. The dependency with the

former is due to the fact that increasing the energy of the γ photon means increasing the cross section of the pair production process. The dependency with the latter instead is because at larger distances, the probability of an interaction between a VHE γ-ray photon and an EBL one increases, meaning a more dim observed flux.

A quantity that can be extracted from observational data, and holds an important value for blazar emission interpretation, is the **variability time** denoted as $\boldsymbol{t_{var}}$. It is the significant variability of the flux of a source, and it is an indicator of the **emitting region size ($\boldsymbol{R}$)** being related by:

$$R \simeq c\, t_{var} \frac{\delta_D}{1+z} \tag{1.21}$$

The determination of t_{var} depends on the type of instrument that performing the measurements, as it cannot be smaller than the integration time for the fluxes of the instruments. Another dependency is on the model that is used for the emission, if there is more than one emitting zone, then the t_{var} can be different between one zone and the others.

There are other parameters that are used to describe the population of electrons responsible for the electromagnetic emission. They depend on the type of source that it is observed, and usually for blazars a broken power law model is used to describe the electron energy distribution. This type of model is described by:

$$n_e = \begin{cases} k_e \gamma^{-p1} & \text{for } \gamma_b \geq \gamma > \gamma_{min} \\ k_e \gamma_b^{-p1-p2} \gamma^{-p2} & \text{for } \gamma_{max} \geq \gamma > \gamma_b \end{cases} \tag{1.22}$$

with $\boldsymbol{k_e}$ being the **electron number density** expressed in units of cm^{-3}, **p1** and **p2** are the two **spectral indices** of the distribution, $\boldsymbol{\gamma_{min}}$ and $\boldsymbol{\gamma_{max}}$ are respectively the **Lorentz factor minimum** and **maximum** values that are allowed, $\boldsymbol{\gamma_b}$ is the **breaking value** of the **Lorentz factor** that separates the two power law distributions.

The last parameter that is necessary in order to describe the broad band emission of a blazar is the **magnetic field B** of the jet. It is important for the description of the height and position of both peaks.

1.4 γ-ray blazars

Blazars are characterized by a broad band emission, ranging from radio up to γ-rays. The latter cover a wide range of energies and need different observational techniques to be detected. Gamma rays are divided into four categories depending on their energy:

- High Energy (HE) (0.5 MeV - 100 GeV);
- Very High Energy (VHE) (100 GeV - 100 TeV);
- Ultra High Energy (UHE) (100 TeV - 100 PeV);
- Extreme High Energy (EHE) ($>$ 100 PeV).

The first one can be directly observed using space satellites, while the last three need indirect measurements due to the limited effective area of space instruments. Current generation instruments are able to detect photons up to $\sim O(1\,PeV)$ energies.

1.4.1 Direct measurements

Performing direct γ-ray measurements is currently possible in the HE regime. The phenomenon behind the detection of these γ-rays is the pair production: the incident photon collides with a high Z material creating an electron-positron pair that then emits again a photon and the process repeats obtaining an electromagnetic cascade. The most recent instrument to detect high energy radiation is the *Fermi*-LAT satellite.

Fermi-LAT telescope

The *Fermi*-LAT satellite[1] was launched in 2008 by NASA, it is composed of two instruments, the Gamma-ray Burst Monitor (GBM) and the Large Area Telescope (LAT).
The former, with an energy range between 8 keV and 30 MeV, consists of 12 NaI scintillators and 2 cylindrical BGO detectors. It works in two time resolution modes depending on the event, the normal one of $\sim 0.256\,s$ and the burst mode of $\sim 0.064\,s$ to be able to observe almost 200 gamma ray burst events a year.
The LAT instrument is an array of 4x4 towers each with a surface of 40x40 cm^2 and composed of 18 layers of Si strip detectors, a calorimeter (12 CsI bars), photodiodes and everything is covered by an anti coincidence shield to distinguish among a gamma event or a background one. It has an energy range between 20 MeV and 300 GeV, with a total effective area of $\sim 1\,m^2$.

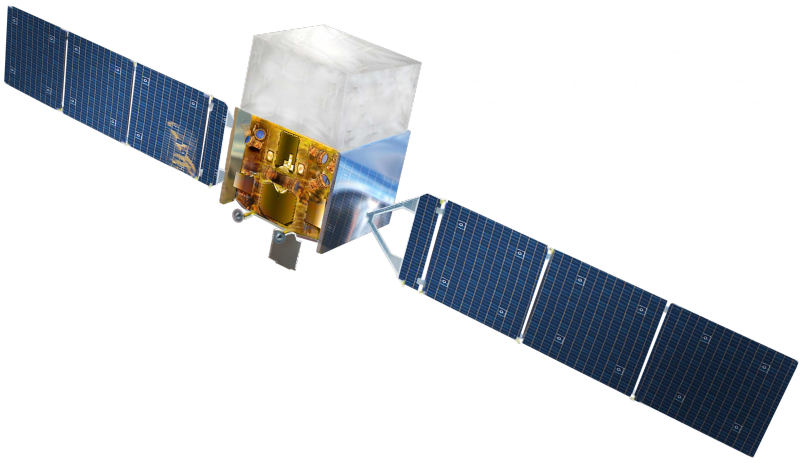

Figure 1.9: Structure of the *Fermi*-LAT telescope.

Blazars are particulary active sources in the *Fermi* energy range, according to the latest catalogue 4FGL-DR3 (Abdollahi et al., 2022) this instrument has detected more than 3000 blazars between 50 MeV and 1 TeV

1.4.2 Indirect measurements

At energies above $\sim 100\,GeV$ space instruments become too inefficient, the flux of energetic photons dims and creating telescopes with bigger effective areas becomes difficult due to the

[1] https://fermi.gsfc.nasa.gov/

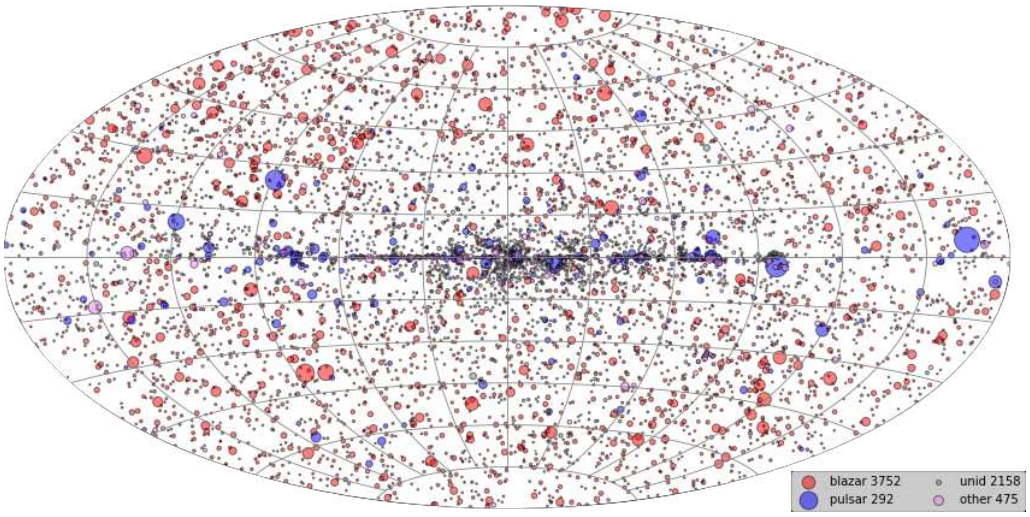

Figure 1.10: *Fermi* map showing all of the sources included in the latest catalog (Abdollahi et al., 2022).

fact that space satellites need to be transported with rockets, so they shouldn't be heavy. The only possibility is to perform indirect measurements from the ground. The VHE photon interacting with our atmosphere produces a positron-electron pair that both then emit a photon via bremmstrahlung, creating this way a cascade of particles called electromagnetic shower. The electrons in the shower, being faster than light, polarize the atmosphere that they are traversing, emitting Cherenkov radiation. This type of emission is characterized by its frequency $\sim 420\,nm$, and by its emission angle, being:

$$cos\,\theta_C = \frac{1}{n\,(\lambda)\,\beta} \tag{1.23}$$

with $\beta = \frac{v}{c}$. The number of Cherenkov photons emitted per unit length and energy by a particle of charge $Z_p e$ is given by:

$$\frac{d^2 N_{ph}}{dEdx} = \frac{2\pi\alpha Z_p^2}{hc} sin^2\theta_C \tag{1.24}$$

that can be rewritten in terms of wavelength as:

$$\frac{d^2 N_{ph}}{d\lambda dx} = \frac{2\pi\alpha Z_p^2}{\lambda} sin^2\theta_C \tag{1.25}$$

There are two techniques used to indirectly measure VHE gamma rays, both using Cherenkov light, the Extensive Air Shower (EAS) array and the Imaging Air Cherenkov Telescopes (IACTs).

Imaging Air Cherenkov Telescopes

Imaging Air Cherenkov Telescopes (IACTs) are ground based instruments that image the Cherenkov light emitted by a cascade in the atmosphere, enabling the reconstruction of the direction end energy of the incident particle.
IACTs have very large mirrors in order to collect as much Cherenkov light as possible and

focus it into a camera composed of several hundreds of photo multipliers (PMTs) that need to record these fast flashes of light. These telescopes are very sensible to the Night Sky Background (NSB), that limits the sensitivity at lower energy.
The key aspect of the imaging technique is to capture the image of the shower on the camera and try to parametrize it and distinguish among a γ-ray event and a background one due to hadronic showers, muons or NSB. This distinction is very difficult, due to the fact that background events exceed by several orders of magnitude the gamma ones, in te next chapter this topic will be treated in more detail.
An important quantity for IACTs is the sensitivity, defined as the minimum flux detectable from a γ-ray source with a significance of $5\,\sigma$ in 50 hrs. This sensitivity can even be integral if it is computed by integrating or summing over an energy range, while differential if it is computed in energy bins.

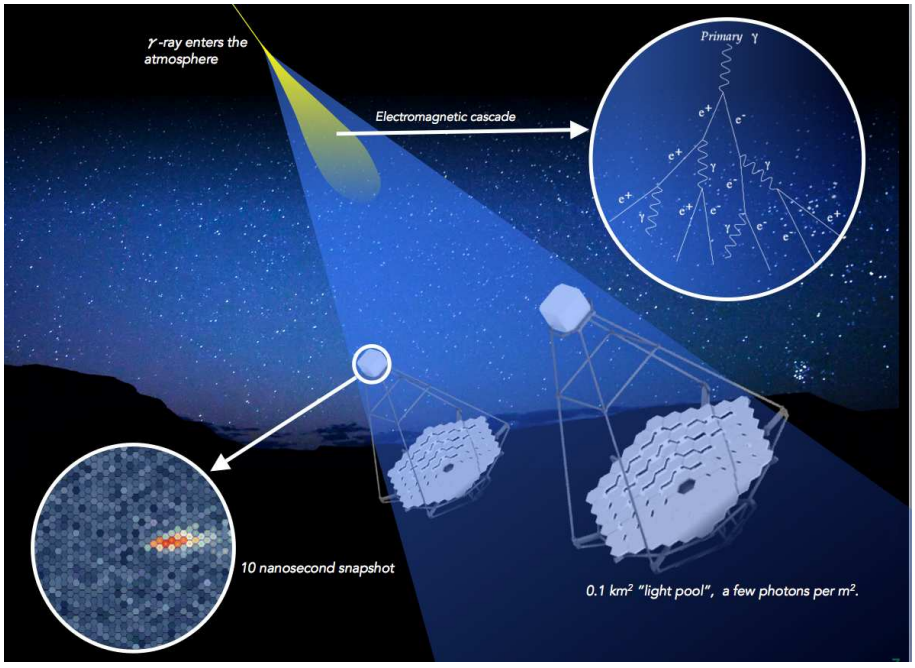

Figure 1.11: Scheme of the imaging atmospheric Cherenkov technique. Image from (Mangano, 2017)

Nowadays there are 3 main IACTs fully working:

- High Energy Stereoscopic System (H.E.S.S.), operating since 2004 and located in the Namibia desert. It is composed of 5 IACTs displaced in a square shape, 4 telescope have a diameter of 13 m with a FoV of 5^o and are placed at the corners, while the fifth one, build in 2012, has a diameter of 28 m and a smaller Fov compared to the other 4 (3.5^o). The HESS energy range is now between $\sim 30\,GeV$ reaching up to $\sim 10\,TeV$ (Giavitto et al., 2018).

- Very Energetic Radiation Imaging Telescope Array System (VERITAS), operating since 2007 and located in Arizona, USA. It is composed of 4 telescopes each with a diameter of 12 m. The FoV is of $\sim 3.5^o$ and the system has an energy range between $\sim 80\,GeV$ up to $\sim 30\,TeV$ (Park, 2015).

- Major Atmospheric Gamma-ray Imaging Cherenkov telescope (MAGIC) will be discussed in the esecond chapter.

A new generation of IACT is in construction, named Cherenkov Telescope Array (CTA). It will consist of two arrays, one in the northern hemisphere, specifically in the island of La Palma, and will cover an energy range between $\sim 20\,GeV$ and $20\,TeV$, while the other in the southern hemisphere in Chile will span the $20\,GeV$ to $300\,TeV$ interval. The peculiarity of this future of observatory is that it will be composed of 3 different types of telescopes:

- Large Sized Telescopes (LSTs), with a diameter of 23 m. They have a FoV of 4.5^o and cover an energy range between $20\,GeV$ up to $200\,GeV$. The first prototype (LST I), completed in 2018, is already operating in La Palma and in the next few years another 3 LSTs will be constructed (LST II-IV).

- Medium Sized Telescopes (MSTs), with a diameter of 12 m, will mount Davis-Cotton reflectors. They have a FoV of 8^o and cover an energy range between $150\,GeV$ up to $20\,TeV$.

- Small Sized telescopes (SCTs), with a dual mirror Schwarzschild-Couder aplanatic displacement of the reflectors, with the primary mirror of 4.3 m in diameter and a secondary mirror with a diameter of 1.8 m. They have a FoV of 9^o covering an energy range between $5\,TeV$ up to $300\,TeV$.

Extensive Air Shower array

Extensive Air Shower arrays are ground based instruments that measure the charged particles of the shower arriving on the ground, a technique called particle sampling. An EAS usually consists of hundreds of Water Cherenkov tanks coupled with scintillators or resistive plate chambers, spread throughout an area of $\sim O(1\,km^2)$. They are located at high altitudes because they collect just the front shower particles so they need to observe as many of them as possible, and combined with the fact that the production of secondary particles is more effective at higher energies, it makes the EAS energy threshold to be of the order of TeV. On the other hand these particles continously arrive so EAS can operate day and night and adding their wide effective area and field of view, then they can perform all-sky monitors.

Currently there are two EAS arrays working, the High Altitude Water Cherenkov (HAWC) (Abeysekara et al., 2017) and the Large High Altitude Air Shower Observatory (LHAASO) (Cao et al., 2022).
The former has been operating since 2015 and is located at an altitude of 4100m in Mexico. It is composed of 300 water Cherenkov tanks with 3 PMTs each distributed in an area of $20000m^2$.

The latter instead started taking data in 2019, is located in China at 4410 m above the sea level. It is composed of 4 types of instruments:

- 5159 scintillators, $1\,m^2$ each with a 15 m spacing;

- 1171 muon detectors, $36\,m^2$ each with a 30 m spacing;

- 3000 water Cherenkov tanks, $25\,m^2$ each and covering a total area of $7800\,m^2$;

- 12 wide field Cherenkov telescopes.

The energy range of LHAASO is quite wide reaching even above $10^{15}\,eV$, being able to measure the most energetic photon in history of 1.4 PeV (Cao et al., 2021).

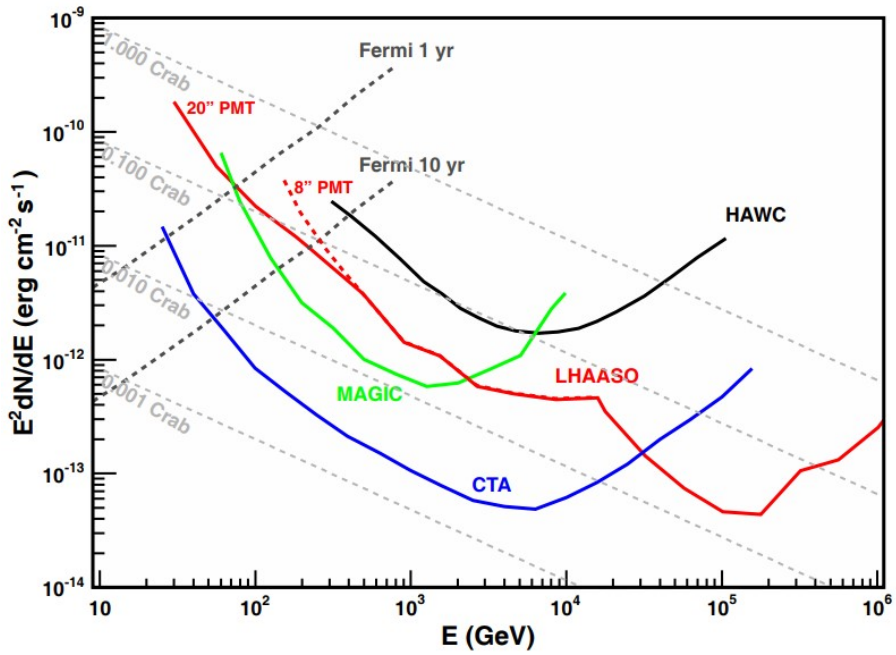

Figure 1.12: Sensitivity curves of IACTs and EAS, image from Cao et al. (2022).

1.5 PG 1553+113

PG 1553+113 is a BL Lac object located at $z = 0.433$ (Dorigo Jones et al., 2022) in the constellation of Serpens [RA $15^h55'43''.04$, Dec $+11^h11'24''.4$]. It was first discovered in 1986 in the Palomar-Green survey of UV stellar objects (Green et al., 1986), its VHE emission was found by both the MAGIC collaboration (Albert et al., 2006) and the H.E.S.S. collaboration (Aharonian et al., 2006). Since then it has been constantly monitored by other observatories (Middei and et al., 2023).
Its SED, as shown in Fig. 1.13, is characterized by the typical double-peaked shape, with a very broad synchrotron emission and a narrow IC one, this particular feature will be discussed in more detail in the next sections.
The most recent work on the broad band emission modelling is (Aleksić et al., 2015). In Fig. 1.13 shows the SED during the flare episode that happened in 2012, the parameters used for this model are shown in Tab. 1.1. The model used in this paper is a one-zone synchrotron self Compton, that I have tested with a more recent dataset, and a comparison between my work and that of (Aleksić et al., 2015) will be shown and discussed later.

z	δ_D	γ_{min}	γ_{max}	γ_b	p1	p2	B (G)	K (cm^{-3})	R (cm)
0.4	40	3700	$8 \cdot 10^5$	36000	1.6	3.83	0.045	19.5	$6 \cdot 10^6$

Table 1.1: Parameters of the model represented in (Aleksić et al., 2015).

1.5.1 Binary system of supermassive black holes

A characteristic feature of PG1553+113, as shown in Fig. 1.14 is a periodic emission of ∼2.2 yrs in the *Fermi* energy range with a significance of $\sim 3\sigma$ (Ackermann et al., 2015). This periodicity, even though it is seen in other bands such as radio and opical, it is significantly detected only in the *Fermi* energy range. This periodic emission can be related to a very peculiar phenomenon in the AGN world, which is the presence of a binary system of supermassive black holes (SMBH) at the center of the galaxy.

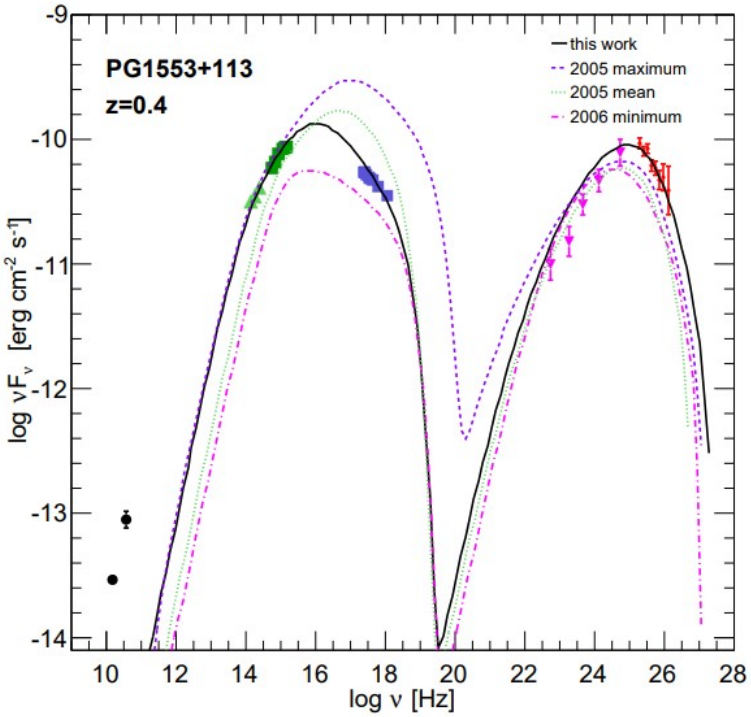

Figure 1.13: SED of PG 1553+113. Image from (Aleksić et al., 2015).

The most probable cause for the appearance of a pair of black holes in the center is the collision between two galaxies (Begelman et al., 1980). It is a rare phenomenon even to observe due to its short timescale but it is of great relevance in several fields, in particular that of gravitational waves, because the two black holes during their spiraling orbits, emit GWs that should contribute significantly to the GW stochastic background (Broadhurst et al., 2023). Other relevant topics in which the presence of binary systems of SMBH is important are that of galaxy structure and evolution because the presence of the couple could change the stellar population in its proximity and can generate instabilities and turbulence in the accretion disk.

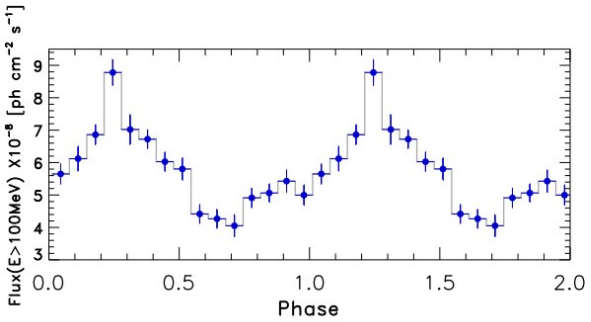

Figure 1.14: Pulse shape of the γ-ray flux above 100 MeV. This plot shows the periodicity of 2.18 years. Image from (Ackermann et al., 2015).

Chapter 2

MAGIC Telescopes

The Major Atmospheric Gamma-ray Imaging Cherenkov telescopes(MAGIC) is a system composed of two telescopes MAGIC I (2003) and MAGIC II (2009). They are both located at 2200 m above the sea level in the Observatorio Roque de los Muchachos (ORM) in La Palma, Canary Island. They detect the Cherenkov light emitted during an electromagnetic shower using the imaging technique, described in the previous section.

Figure 2.1: Photo of the two MAGIC telescopes, MAGIC II is the one on the left while MAGIC I is on the right. Credit: Giovanni Ceribella

2.1 MAGIC hardware

2.1.1 Telescope structure and drive system

One of the goal of this telescope is to observe transient events. In order to do so it was built with both a solid and light structure. It has a weight of $\sim 67\,t$ that is distributed into several components: the camera ($\sim$ 0.89 t), the towers ($\sim$ 20.2 t), the active mirror control ($\sim$ 9 t), the camera bow and the counterweights($\sim$ 3.4 t), the six carriages ($\sim$ 25 t) and

lastly the carbon fiber dish ($\sim$ 8 t) to avoid any deformation of the telescope.
In order to perform transient event measurements, the telescopes should not only be light and robust but even fast. For this reason the driving system works in three ways:

- **repositioning mode**: during common observations it is used to point from a source to another. It can be either done at normal speed so $\sim 7°/s$ or at $4°/s$ in this last case it is called fast repositioning mode;
- **tracking mode**: its purpose is to track the objects during observations
- **parking mode**: when the telescope is not performing any measurements during the day. Screws are applied to secure the telescope.

The telescopes have a range in elevation axis between -73° and 100° while in azimuthal axis is 400°. When either the weather conditions are not good or after the sunset, the telescopes are secured to the ground by inserting some bolts.

2.1.2 Mirrors

MAGIC I and II have different sets of mirrors due to technical reasons:

- MAGIC I has Al honeycomb sandwich 50x50 cm^2 mirrors produced by both INFN Padova and MPI, on the edges of the telescope instead 1x1 m^2 mirrors and recently with the same area but Al honeycomb sandwich by INFN and cold sluped by INAF have been installed;
- MAGIC II instead has only 1x1 m^2 mirrors, 143 of the Al honeycomb sandwich type produced by INFN and 104 cold slumped by INAF.

The choise of parabolic mirrors instead of spherical ones is due to the fact that the former, eventhough are more expensive, are isochronous.
The Point Spread Function (PSF)is a quantity that gets estimated every night that tells the amount of deformations and performance of the mirrors. It is useful to know because the PSF is what limits low energy observations.

2.1.3 Active Mirror Control (AMC)

The Active Mirror control (AMC) is a system used to correct the mirror alignment and focusing due to the different gravitational load at which the telescope is subject during the observations. It is necessary due to the fact that moving the telescopes causes some deformations that need to be taken into account and correct. The AMC consists of several actuators in axial and cardan joints. The distribution is slightly different for the two telescopes:

- MAGIC I: eight independent chains that are aligned in the horizontal direction, each chain has 8 active Mirror Control electronic boxes;
- MAGIC II: seven independent chains with nine or eight AMC electronic boxes.

2.1.4 SBIG camera

The SBIG camera is a CCD with the purpose of measuring the PSF of each mirror and that of the reflector to estimate in the end the reflectivity of the reflectors at different frequencies. It takes the star field in the camera and its reflection.

Figure 2.2: AMC lasers activated on MAGIC I, photo taken from (Biland et al., 2007)

2.1.5 Camera

The Camera is the part of the telescopes with the purpose of collecting the Cherenkov light. It is composed of 1039 photomultipliers for each telescope. The total FoV of the camera is of 3.5° with the structure divided into 169 clusters, with 7 pixels each.
The structure of the cluster and the pixel is shown in Fig. 2.3, the latter is constituted by several components, the first one is the PMT, which collect the Cherenkov radiation and convert it into photoelectrons. Then, these electrons travel through a voltage that can reach up to 1250 V thanks to a Cockroft-Walton voltage multiplier. The signal is amplified by a AC coupled pre amplifier, and in the end it passes through a Vertical Cavity Surface Emiting Laser (VCSEL) a component that converts an electrical signal into an optical analog signal that is then transported using 160 m long optical fibers.

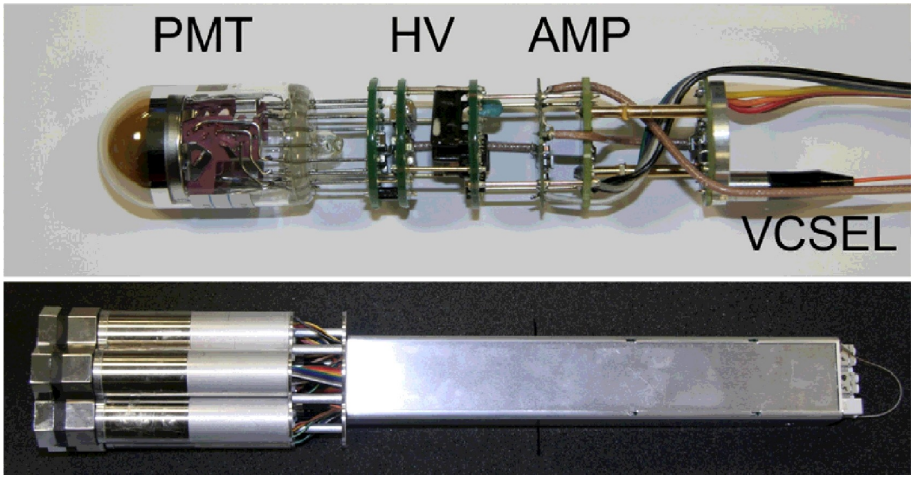

Figure 2.3: MAGIC pixel structure (top figure). Side view of MAGIC pixel cluster (bottom figure). Image taken from (Aleksić et al., 2016)

The camera has other components that have different purposes:

- temperature control system: composed of two Al plates with water running in horizontal channels. It keeps the temperature at 20°C;
- drying unit: it removes humidity from the camera, it's available just for MAGIC II;
- lids: they are shutters used to cover the camera during the day;
- spectralon plate: It is used to focus star images, so that gamma events can be focused on the PMT plane;
- Starguider LED: their purpose is to obtain the position of the camera with respect to the observed stars;
- low voltage power supply;
- temperature and humidity sensor: respectively eight and four sensors to check the conditions of the camera;
- moon filters: used to perform strong moon observations.

2.1.6 Calibration system

The calibration system is the hardware component responsible for the calibration of the camera. It is composed of two calibration boxes, one for each telescope, that receive a specific light pulse.
Each calibration box has several instruments inside:

- a pulsed UV passively Q-switched Nd-YAG laser of 355 nm wavelength. The main property of this pulse is that it has a similar frequency to Chrenkov photons and a pulse width of 300 ns;
- two filters to estimate the linearity of the amplification chain;
- an Ulbricht sphere to obtain an homogeneous radiation;
- temperature and humidity sensor to check the status of the system.

These two boxes have several purposes.

- obtain the PMT HV flat fielding;
- obtain the conversion factor from Flash Analog to Digital Counts (FADC) and photoelectrons, via the calibration runs and intervealed calibration runs;
- see the linearity of the system from PMTs to readout.

2.1.7 Readout electronic system

After the electron to photon conversion thanks to the VCSEL, the signal is transported to the counting house, where the readout electronics, the trigger system and the data storage units are placed. As soon as the signal arrives in the counting house it is divided into two channels:

- a trigger branch: here the signal goes through different trigger levels;
- a readout branch: here the signal is stored waiting for a decision from the trigger branch.

If the signal passes the trigger checks is then stored first in a Domino Ring Sampler 4 and then sent to the Data AcQuisition system (DAQ).

Digital Trigger system

The Digital trigger system consists of three data filters:

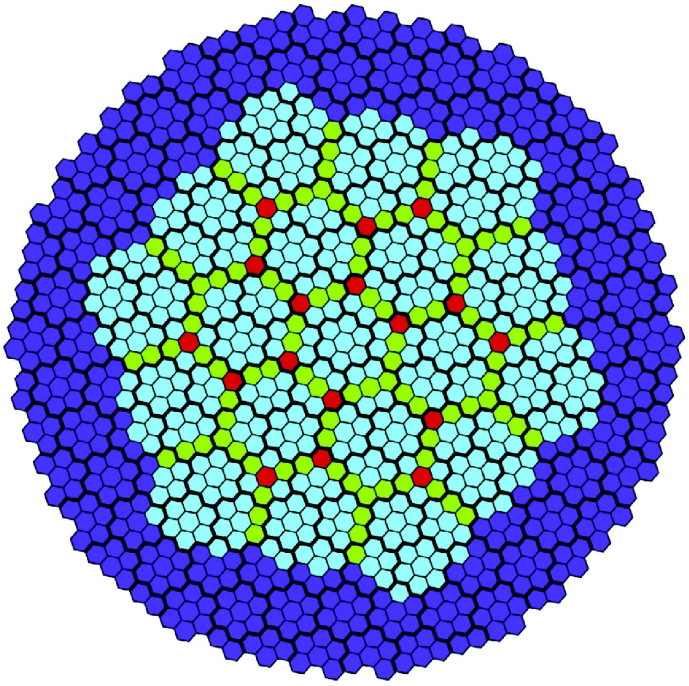

Figure 2.4: MAGIC pixel macrocell division. Image taken from (Aleksić et al., 2016)

- Level Trigger 0: it converts the signal from analog to digital only if it is above a certain threshold level. The signal is the syncronized due to the presence of some delays due to intrinsic differences in the position of the PMTs or even due to the physical event.
- Level Trigger 1: it is used to avoid the contamination from the NSB and consists in dividing the camera in 19 regions called macrocells, each containing 37 pixels. The purpose of this trigger level is to detect close compact clusters activity in each macrocell, using different neighbouring pixels configurations (NN). After this the signal is transferred to the Trigger Processing Unit (TPU) for the stereo trigger.
- Stereo Trigger: it is a logical combination trigger (AND) that combines syncronized signals from both telescopes.

Observations can be performed under different sky conditions and different types of sources, a factor that needs to be changed is the Discrimation Treshold (DT), to have an instrument as optimal as possible. The DT is 4.25 photoelectrons if the source is extragalactic or 4.89 phe if the source is of galactic origins.

Topological trigger and Sum trigger

There are other two trigger systems in MAGIC, the topological trigger and the sum trigger.
The former is a substitute to the LT3 stereo trigger and uses the information about the positions of the 19 macrocells. It consists of fixing a macrocell in one telescope that recorded a γ event and guessing the position of the macrocell in the other telescope, because gammas trigger the same macrocells in both telescope or adjacent ones. This type of trigger allows

to go lower energy thresholds and obtain better effective areas.
The Sum trigger instead is an analog trigger and it's based on adding neighbouring macrocells and applying a threshold on the sum of these macrocells. Then the output of both telescopes is sent to the L3 Stereo trigger. Both these triggers are typically used to perform low energy observations of pulsars and with the Sum trigger the Crab Nebula was observed with energies as low as 25 GeV.

Readout System
While the signal is recorded and waiting to pass through the trigger branch, it is also stored for a short period in the readout branch. It is made of several hardware components responsible for data storing and processing, in total there are 48 receiver boards, 12 analog PULSer And Recorder (PULSAR) and 2 digital boards.
The MAGIC Optical NanoSecond Trigger and Event Receiver (MONSTER), known as receiver boards, is where the journey of the signal in the readout system begins. Composed of multilayer 9U boards that can receive a maximum 24 channels, performing several tasks:

- Give the output of LT0 to the LT1s via the Mini Delta Ribbon (MDR) cables;
- Monitoring of the L0 counter rate of every pixel by integrating the Individual Pixel Rates (IPR) counts;
- Conversion from an optical to an analog electronic signal;
- Digitalize the analog signal using the DRS4;
- Generate the LT0 individual pixel trigger signals;
- Read a copy of the signal to the Sum trigger.

Then from the receiver boards the signal goes to the PULSAR boards located in two 9U VME crates for each telescope. There are then two other PULSAR boards:

- DIGI PULSAR: its purpose is to send to the other PULSAR boards the infos about the trugger arrival for the data readout;
- BUSY PULSAR: it stops the triggers when the system is full and it is busy processing data.

The Domino Rings Sampler 4 (DRS4) are mounted on a Domino mezzanine board. Its goal is to sample the signal and store with a sampling frequency is 1.64 GHz. The DRS4 is an array of 1024 capacitors connected to the receiver boards, actually just 60 if those capacitors are used for the read out to lower the deadtime of this instrument.

Data Acquisition System
After the signal is digitalized in the DRS4 it goes to the Four Input Links for Atlas Readout (FILAR PCI) hosted in the Data AcQuisition computers. Then, the Domino4Readout, a multithread C/C++ program has the following aims:

- reads the data and creates the packets with the events;
- corrects the data from pedestal noises and applies the online;
- storing data into .raw files that are the standard initial MAGIC data format.

Finally the data are stacked into bunches of 100 and then stored into raw files, each containing $\sim$14000 events.

2.1.8 Weather instrumentation

MAGIC, as all the other IACTs, is very sensitive to the weather conditions. These should be good in order to have an optimal data taking. There are several auxiliary instruments that serve this purpose:

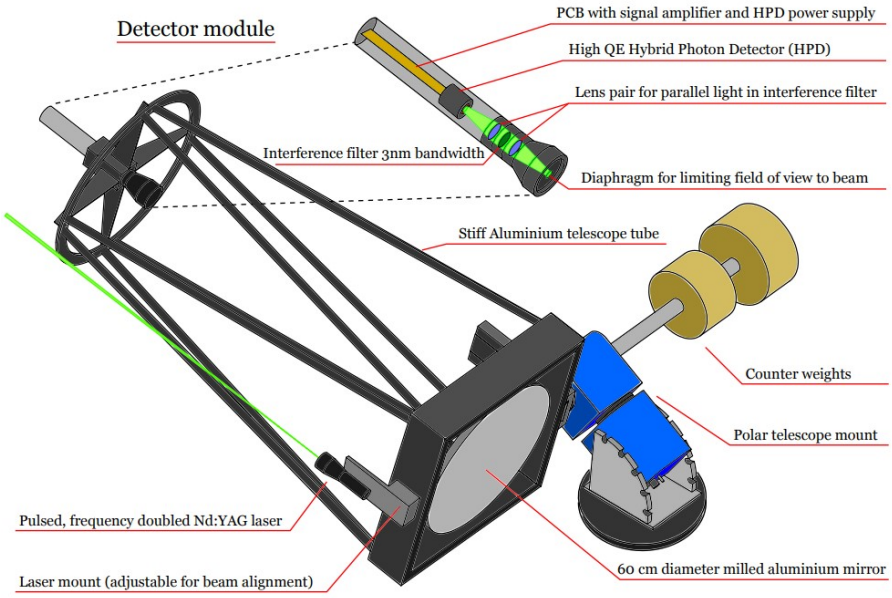

Figure 2.5: LIDAR structure. Image taken from (Fruck et al., 2014)

- pyrometer: it measures the presence of clouds in the sky, usign the so called so the **Cloudiness** parameter. In order to do so the pyrometer observes the temperature of the sky, taht is higher in case of clouds passing by due to the reflection of earth's thermal radiation by the same clouds;

- all Sky Camera: It takes pictures of the sky once every 2 minutes and has a FoV of 150°. These photos are then taken into account to consider the quality of the sky;

- weather station: it measure humidity, wind speed and direction, and temperature. If the weather conditions are above the safety ones, it sends automatic alert to stop telescope observations;

- TNG Dust particle counter: It measures, thanks to a laser, the density of the dust in units of $\frac{\mu g}{m^3}$. It is particularly useful in case of calima a wind typical of La Palma that brings the sand from Africa;

- LIDAR: it measures the scattering of aerosol particles in the air with a Nd:YAG laser. It has a wavelength of 532 nm, energy of 5 μ J, a width of 0.5 ns and the telescope has an Al mirror of 60 cm in diameter with a focal length of 1.5 cm and lastly an Hybrid Photo Detector (HPD) with a peak of 55% in quantum efficiency. By registering the arrival time of the scattered photons it measure the transparency of the atmosphere, expressed using a quantity called Transmission that goes from 0 (bad transparency) up to 1 (fully transparent) and it is computed at different altitudes;

- rain sensor: an IR LED provided by the First G-APD Cherenkov Telescope (FACT). It is taken into account in the weather report but does automatic reactions.

2.1.9 Cooling system

Having a lot of hardware an electric components, MAGIC needs a cooling system, that is composed of:

- several water circuits that distribute this liquid to cool the heat exchangers and the air inside the racks;
- ten heat exchangers each for a rack. They keep a temperature between 10-20°C if electronic is off or 22-32°C if it is on;
- three Rital chillers that cool down the water for the heat exchangers.

2.2 MAGIC software

2.2.1 Central Control

As discussed before, the telescopes have several subsystems that need to be controlled, from the drive system to the AMC and even some weather related instruments like the LIDAR or the pyrometer. All these subsystems are controlled by the MAGIC Central Control (CC). The program behind the CC is called SuperArehucas (SA), that is a Graphical User Interface (GUI) used to operate these telescopes. The link between the CC and all of these subsystems happens via TCP/IP sockets, so each subsystem opens a read socket to obtain informations from the CC and a write socket to send back infos to the CC. Both the CAmera COntrol (CaCo)and the LIDAR comunicate even with the weather station, just in case of some automatic action that needs to be taken quickly.

2.2.2 Automatic Alert System

In order to observe transient events (e.g. Gamma-Ray Bursts), MAGIC needs some external trigger system. The MAGIC Automatic Alert system is a multithread C program that is connected to the Gamma-ray Coordinates Network (GCN). If there is an alert, the program, that runs always in background in La Palma, handles the alert applying some observational criteria. If it observable, it automatically repoints the telescopes by sending a message to the CC.

2.2.3 On site data analysis

MOLA

MAGIC OnLine Analysis (MOLA), it is a program that runs during night data-taking. It performs an analysis from low up to high level obtaining preliminary results. It is especially important for the follow up of Target of Opportunities (ToOs), transient events and flaring sources.

OSA

The On-Site Analsysis (OSA) is program that performs the low level analysis of the data taken during the night. Raw data from the DAQ and the reports from the CC are both copied and then moved in the GF2 common storage and then put in a MySQL database. The OSA proceeds with the analysis and sends the results to Port d'Infromacio Cientifica (PIC) in Barcelona where the data is finally stored. This is done to reduce the

data size of a factor 500, allowing analyzers to perform the high level analysis in a faster way.

Data Check System

The Data Check System is composed of a series of scripts that run at the end of the night and produce a graphical output to check the conditions that might affect data quality. One of the most important plots produced by the Data Check System is the so called Superplot, it contains infos about the following quantities:

- Zenith angle distribution as a function of time for each source;
- The current of the M2 camera, as a function of time;
- L3 trigger rate as a function of time;
- the Transmission coefficient at 9km (T_{9km}), at 3km (T_{3km}), and cloudiness as a function of time.

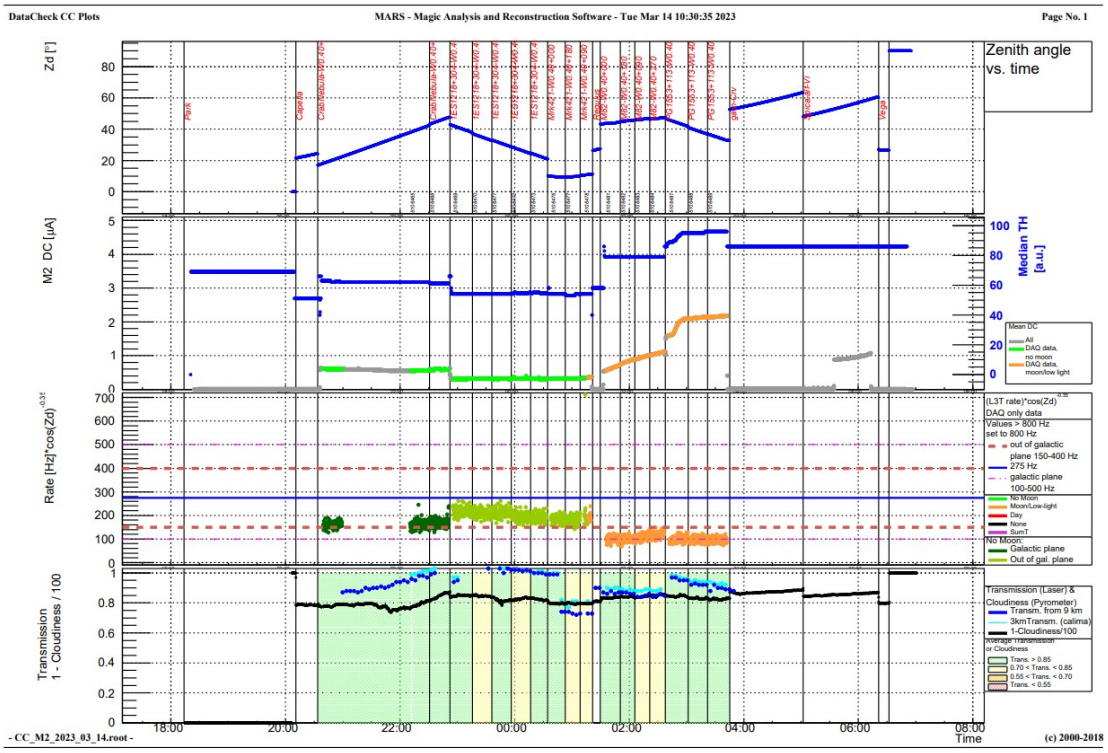

Figure 2.6: Superplot of the 14/03/2023

2.3 Night conditions and pointing

2.3.1 Night conditions

Every IACT, so even MAGIC, has a low duty cycle. The best night condition is the so called *dark-time*, when data are taken with no moon in the sky. It accounts for ∼1600 hours each year and the derived duty cycle is ∼18%. This value actually is lower because it can happen that there is bad weather during the night or there can be some technical problems. These issues can reduce the value of available hours of ∼40%.
Luckily MAGIC can also observe during the so called moon-time. Due to the presence of the moon, the NSB levels are higher than dark time and DTs should be increased and a

particular type of analysis is performed. In the period of full moon observations are not performed for a few nights.
In order to avoid any type of hardware damage there are *safety limits* that have been established:

- The current of each PMT < 47 μA;
- The average current of the PMTs < 30 μA;
- humidity $< 90\%$;
- minimum zenith distance 1.5°;
- wind speeds < 40 $\frac{\text{km}}{\text{h}}$.

Observations are not performed if these conditions are not satisfied.

2.3.2 Pointing configurations

MAGIC has two different types of pointings used for taking data:

- ON mode: it consists on observing in two different modes. First performing ON observation, pointing the center of the camera to the source, and then performing an OFF observation, pointing the camera elsewhere where there are no gamma sources and possibly at the same zenith and azimuth. The latter type of observation is used to get the background estimation;
- Wobble mode: it consists in observing a source with a certain offset from it, typically of 0.4°. It is a false source tracking method. Usually one or more OFF pointings are taken in a way that they are in the opposite direction with respect to the camera center. These pointings are then used to estimate the background in an unbiased way by taking them in a symmetric manner. Usually 4 pointings, called Wobble positions, are taken.

The usual data taking for MAGIC consists of performing observations with Wobble positions.

2.4 Data analysis

MAGIC has its own software for data analysis that is called MAGIC Analysis and Reconstruction Software (MARS), composed of several programs written in C++ and using ROOT libraries. There are three different level for the analysis:

- low level analysis: first the extention of the files is changed from binary raw to ROOT files and then image cleaning and parametrization is performed on the raw data. This level is usually done by the OSA except for moon data;
- intermediate level analysis: here the stereo images are produced and stereo parameters are computed. Then either Random Forest or Look-Up Tables algorithms are applied to real data.
- high level analysis: this is the final stage for the standard analysis where the graphical outputs are produced.

In order to calibrate and analyze γ-rays, the production of shower simulations are vital. The program used to perform this task is called COsmic Ray SImulation for KAscade (CORSIKA), that can simulate showers produced by different types of primary particles, their interactions in the atmosphere and all these characteristics. For MAGIC, there is a specific type of `CORSIKA` simulations called mmsc. Then another program, called

reflector, simulates the interaction between the Cherenkov photons in the atmosphere and the telescope response of the mirrors to the arrival of these photons. The last program used for these simulations is *camera*, that imitates the response of the camera and of the whole electronics.

2.4.1 Low level analysis

The first step of the low level analysis is the conversion from a binary raw file to ROOT one, this is done using a program called `merpp` (MeRging and Preprocessing Program). The program also merges the reports from the various subsystems to the data file.
After the creation of these ROOT files, then there is the calibration and signal extraction performed by the program `sorcerer` (Simple, Outright Raw Calibration; Easy, Reliable Extraction Routines). It collects two informations for each pixel: the charge, converted using the conversion factor from Analog to Digital Converter counts to the number of photoelectrons; the time of arrival of the signal. The pedestals are subtracted to the waveform and the sliding window algorithm is used to extract the signal that needs to be converted in number of photoelectrons. In order to do so, the F-factor method is used. It considers 1 readout count as C photoelectrons and the ammount of photoelectrons is Poissonian distributed, so:

$$C = \frac{N_{phe}}{\mu} = \frac{\mu}{\sigma^2_{sig} - \sigma^2_{noi}} F^2 \tag{2.1}$$

with C being the conversion factor, N_{phe} is the number of photoelectrons, μ is the readout counts, F^2 is the excess noise factor, σ^2_{sig} is the variance of the of the signal and σ^2_{noi} that of the noise. The flatfielding then is needed due to the different efficiencies of the PMTs, so C can be rewritten as:

$$C = \frac{N_{avgphe}}{\mu} \tag{2.2}$$

with N_{avgphe} being the average number of photoelectrons over all camera pixels.

The time of arrival of the signal is extracted by performing a weighted average of the time slices of the integrated window using the signal as a weigth, so:

$$t_{arr} = \frac{\sum_i i \times s_i}{\sum_i s_i} \tag{2.3}$$

with i being the number of the slice, s_i is the signal associated with the i-th slice.
When the calibration of the image is finished, the next step is to clean and parameterize the image. This is done using star (STandard Analysis and image Reconstruction), whose purpose is to find the pixels containing the signal from Cherenkov photons and not the ones due to NSB. The image cleaning is divided into two phases:

- sum image cleaning: it consists on summing different combinations of neighbour pixels and if the signal is higher than a certain value and has arrived in a certain interval of time, then that signal is considered to be part of a shower image.
- time constrained absolute image cleaning: it consists on classifying the pixels that survived the sum image cleaning into two categories, core and boundary pixels, depending on their charge and time information. The former are the ones that have as direct neighbour at least one pixel that survived the sum filter and its charge is above a threshold Q_{core}. If the arrival time of this core pixel is within a 4.5 ns time window from the mean arrival time of the island, then it is kept. The latter category

instead are pixels that survived the sum cleaning and are neighbours with a core pixel with a charge greater than Q_{bound}. The time of arrival of these boundary pixels should be less than 1.5 ns with respect to their core pixel.

In a standard analysis, the threshold in the number of photoelectrons that is used to select core and boundary pixels is respectively 6 phes and 3.5 phe.

The last part of the low level analysis is to parametrization of the images. This is done to distinguish gamma events from hadronic ones and characterize the primary particle properties. There are several types of parameters used:

- Hillas parameter: firstly introduced by Hillas (Hillas, 1985), they are defined by how the photons are positioned in pixels that are part of the image. Examples of Hillas parameters are *size*, *Center of Gravity* and *width*;
- directional parameters: to find the tail and the head of the island. Examples of directional parameters are *M3Long* and *asymmetry*;
- time parametrs: to check the arrival time of the photons. Examples of time parameters are *Time RMS* and *Time gradient*;
- source-dependent parameters: depend on both position of the source and physical property of the shower. Examples of source-dependent parameters are *alpha* and *dist*;
- image quality parameters: to check the quality of the image. Example of image quality parameters are *number of islands* and *leakageN*:

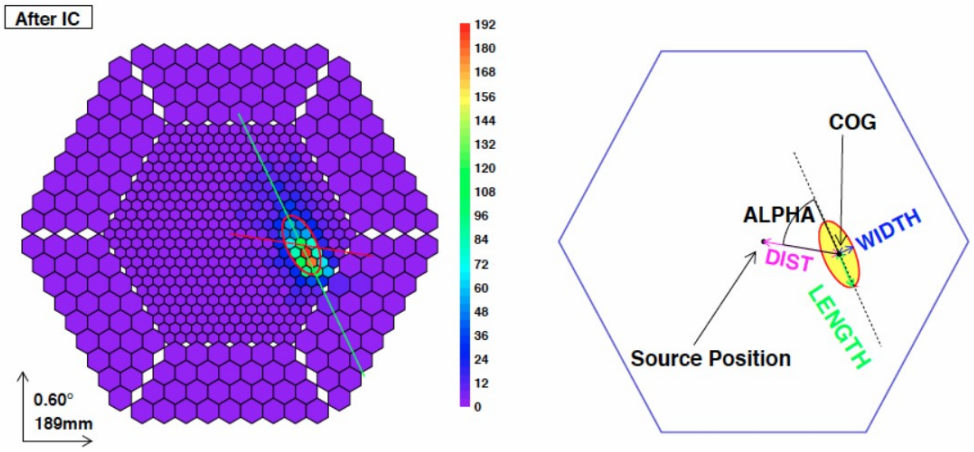

Figure 2.7: Typical image of a gamma shower in the camera and types of used parameters.

2.4.2 Intermediate level analysis

The first step of the intermediate level analysis is to perform the stereoscopic reconstruction. This is obtained by merging the informations of both telescopes into a single file, using a program called `superstar`. It reconstructs geometrically the 3-D shower and computes a set of parameters called stereo parameters. In order to do reconstruct these parameters, `superstar` merges two star files of MAGIC-I and MAGIC-II telescopes. Some of the stereo parameters are shown in Fig. 2.8.
An analyzer usually begins at the `superstar` level if the data is taken during dark time. A useful program to determine with extreme precision, the quality of the data, is `quate`. It can be applied to `star`, `superstar` or `melibea` files and cuts the data based on chosen filters set by the analyzer. Usually the cuts are applied to find data based on:

- Desired values for several quantities (e.g. Zenith range, Rates, DC current, etc...)
- To check if there were problems during observations
- To select data with good weather conditions (e.g. Trasmissivity, Cloudiness, etc..)

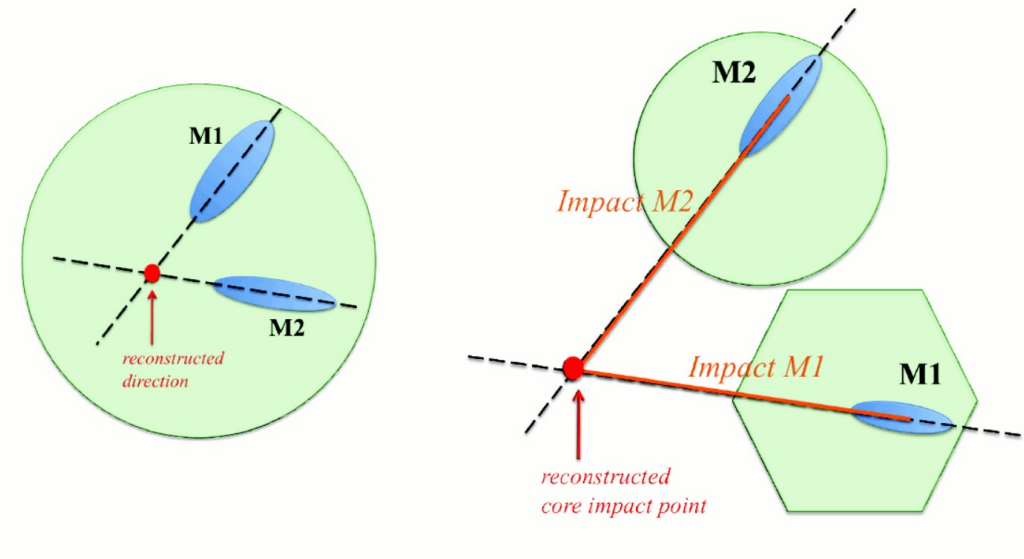

Figure 2.8: Geometrical reconstruction of the direction and impact point. Figure from the MAGIC wiki page

After the stereoscopic reconstruction, there is one of the most crucial phases, of the analysis: the γ-hadron separation, the direction and energy reconstruction of the primary photon. Most of the events recorded by MAGIC and any other IACTs are hadronic showers, while 1 out $\sim$1000 showers are of γ origin. In order to perform the γ-hadron separation MARS uses the Random Forest algorithm, that is a multi dimensional algorithm based on several decisional trees. First of all the RF trees are generated, the number can vary but usually is 100. Each tree is constructed following a scheme: first a parameter is chosen randomly, and a *cut value*, is searched by the RF algorithm in order to get the best division between hadron and γ events. Events are distributed into two subsamples, called branches, depending on the value of the parameter with respect to the cut value. The cut value is obtained by minimizing the Gini index (Gini, 1921):

$$Q_{gini} = \frac{4N_h N_\gamma}{(N_h + N_\gamma)^2} \tag{2.4}$$

with N_h being the number of hadronic events and N_γ the number of γ events. This procedure is then applied again to the subsamples creating more branches. The process stops in two cases, either in a subsample there are only gammas/hadrons or if the subsamples have number of events lower that a predetermined value. The resulting last subsamples, called leaves, get a value, called *hadronness*, that can be either 0 or 1 depending on whenever the event is due to a gamma or to an hadron. Such approach is applied both to the real data and the simulated MC ones. Furthermore, `coach` estimates both *reconstructed energy* and *direction* in a similar way.
The MC simulations are divided into two categories, MC *train* and MC *test*, the former will be used in the program `coach` to generate the RF while the latter in `melibea`. The program that creates the RFs is coach takes as input not only the MC train but even the so called OFF data, that consists of observations with sources that are not particularly strong (<1%C.U.), meaning that they contain almost no γ events. Another property of

train MCs and OFF data is that they should be of the same observational period as the data that is needed to be analyzed (called ON data). This is due to the fact that there can be some changes in the telescope performance that need to be taken into account with a new MC production. Lastly both train MC and OFFs should cover the same Zenith range as the ON data, and the OFF sources should be of the same type as the ON one, so either extragalactic or not.
The next step, successive to the production of the RF, is to apply it to the output of coach, the ON data. This is performed by using `melibea`, that takes as input both ON data and test MCs. The program estimates, from the ON data, different quantities. The first one is the hadronness, and is computed by averaging the values of hadronness of each leaf, so:

$$h = \frac{\sum_i h_i}{N} \tag{2.5}$$

with h_i being the hadronnes value of i-th leaf and N the total number of leaves.

The second quantity that is obtained is the energy estimation. It can be done in two different ways, by using either RFs or LUTs. The latter is based on the assumption that the squared energy of the primary γ is proportional to the amount of Cherenkov radiation emitted in the shower, so the size parameter. So the MCs are separated into bins of size and $\frac{\text{impact parameter}}{r_C}$, with r_C being the Cherenkov radius. Then, as shown in Fig. 2.9, a 2D table that has the mean energy and the Root Mean Square of the MC events for every bin is created and then corrected for some zenith angle dependencies. At the end the value of estimated energy of a real event is kept in the LUT.

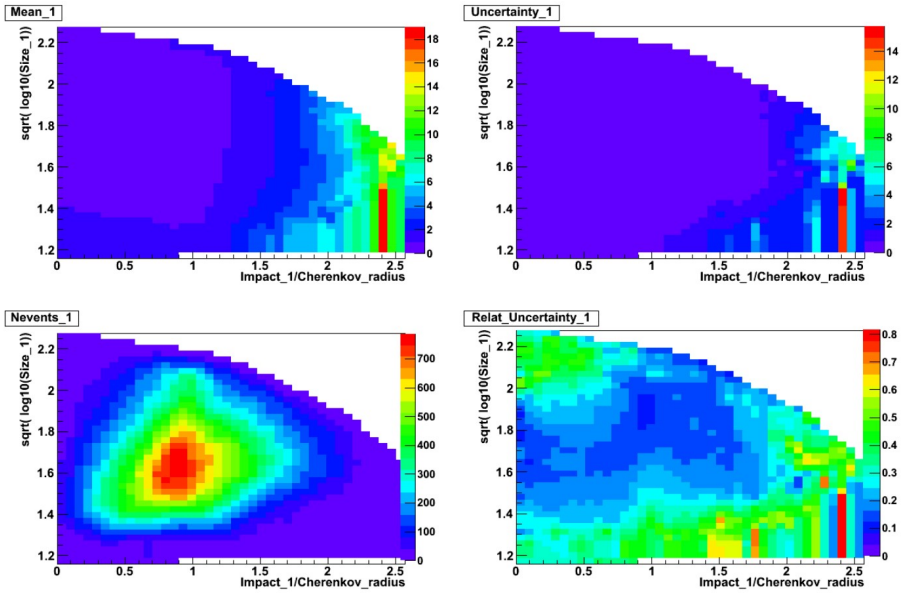

Figure 2.9: Energy reconstruction. Figure from the MAGIC wiki page

The third and last quantity estimated thanks to the RF are the DISP parameters, that are used to reconstruct the incidend direction of the primary photon. It is computed using the DISP RF method, that consists in using an RF algorithm on a continuous variable to retrieve the DISP parameters. They represent the length separation from the Center of Gravity of the image and the position of the source, that is given using:

$$DISP = A(\text{size}) + B(\text{size})\frac{\text{width}}{\text{length} + 2\eta(\text{size})\text{leakage}} \tag{2.6}$$

with A(size), B(size) and η(size) being second order polynomials of log(size). These three parameters are optimized using MCs and performing a regression on a continous quantity using a RF. So in the end one DISP value is obtained for each telescope and event, so two DISPs per event. As soon as this is done, the crossing method is applied to remove any degeneracy. There are four points as shown in Fig. 2.12, and the pair that is chosen is the one that is the closest between each other.

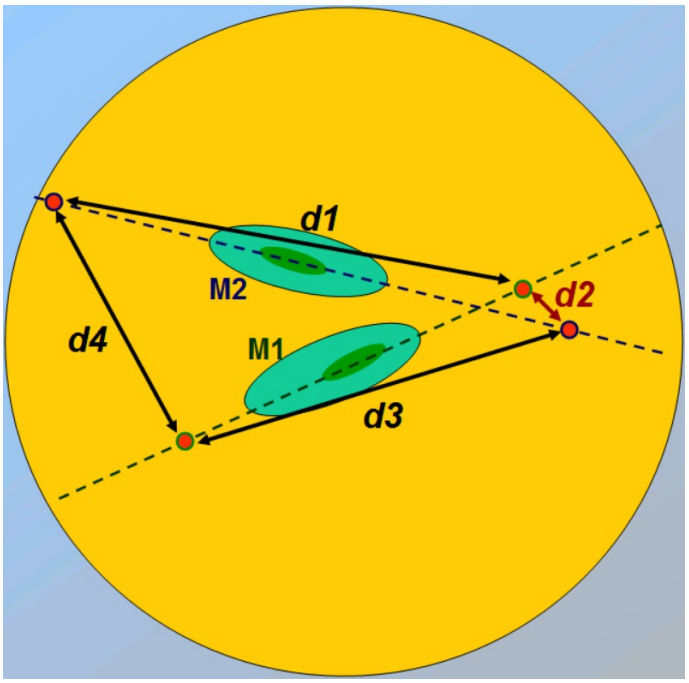

Figure 2.10: DISP parameters. Figure from the MAGIC wiki page

2.4.3 high level analysis

The purpose of the high level analysis is to produce several graphical outputs that give the information on the significance of the detection, the lightcurve and spectrum of the source and skymaps. The program that retrieves the significance of an observation is `odie`, having as output the so called θ^2 plot. θ^2 is the angular distance from the reconstructed position of the source to the real one. γ events are concentrated at low values of both θ^2 and hadronness, hadronic events are isotropically distributed along θ^2 and have larger values of hadronness. So in order to have an optimal significance, the cuts on hadroness and θ^2 have need to change depending on the energy range. There are three types of cuts:

- low energy: it has the best significance at around energies below 100 GeV, due to the low value of size that is required to count low energy events;
- Full range: has the best sensitivity for intermediate energy ranges due to stronger cuts;
- High energy cuts: they have the best sensitivity at energies above 1 TeV and introduce a cut in estimated energy.

These ranges are optimal for different types of sources, the first one for VHE-soft spectrum sources, the FR for Crab like soures, while the last one for sources that have a significant emission above 1 TeV. The different values of the cuts are shown in table.(fai tabella)

θ^2_{cut} is used to delimit the so called signal region. Two histograms are build, one for the

ON region, that should take into account mostly γ events, and one for the OFF region that is for the estimation of the background. From these two histograms the numbers of events N_{on} and N_{off} within the θ^2 cut value are computed. Then the number of excesses is:

$$N_{ex} = N_{on} - \alpha N_{off} \tag{2.7}$$

with α being the ratio between OFF and ON regions.

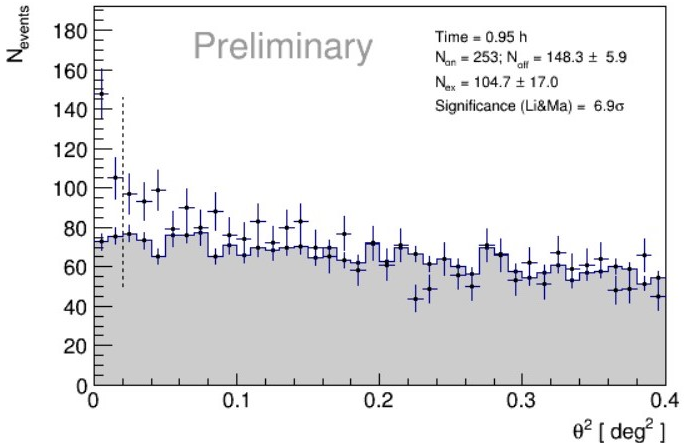

Figure 2.11: Example of a low energy θ^2 plot produced by me. The θ^2_{cut} is the dashed vertical line.

The significance is then calculated with the Li & Ma formula (Li and Ma, 1983):

$$\sigma_{\text{Li \& Ma}} = \sqrt{2\left[N_{\text{on}} \log\left(\frac{1+\alpha}{\alpha}\left(\frac{N_{\text{on}} - N_{\text{off}}}{N_{\text{on}}}\right)\right) - N_{\text{off}} \log\left((1+\alpha)\left(\frac{N_{\text{off}}}{N_{\text{on}} - N_{\text{off}}}\right)\right)\right]} \tag{2.8}$$

Conventionally a source is detected if $\sigma_{\text{Li \& Ma}}$ is above 5 σ.

In order to produce sky maps, the MARS program that is used is called `caspar`. It generates a 2-D reproduction of the arrival direction of photons that are registered during the measurements. There is a problem in doing so, the telescopes do not observe the primary photon position directly, they reconstruct it. This reconstruction has two consequences, the first one being that the γs are measured one by one, meaning that we get a list of photons that are needed to be mapped. The second consequence is that there is an intrinsic error in the photons' coordinates, which smears them around the source. This distribution is called Point Spread Function (PSF), that is a quantification of the telescope resolution.
In order to generate a skymap, first of all, a model of camera exposure is needed, due to the fact that the acceptance of the camera is not uniform. From this model an OFF background map is generated, while the ON map is based on real data. Both of these maps are then smoothed with the PSF and quadrature summed with a Gaussian kernel to even the N_{ex}. The typical values of the Gaussian kernel is:

$$\sigma_{smooth} = \sqrt{2}\sigma_{PSF} \tag{2.9}$$

Finally the significance of the sky map is computed with the Test Statistics method, a Li&Ma significance applied on a background that is both modelled and smoothed.

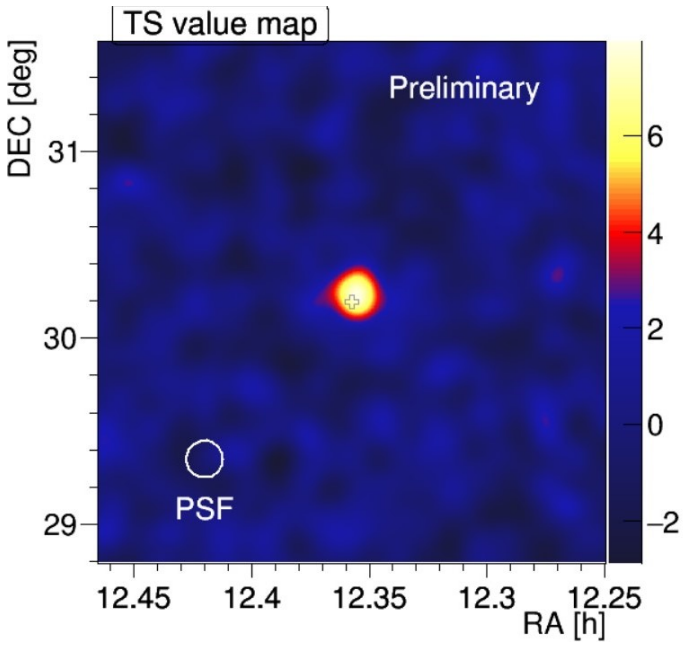

Figure 2.12: Example of a low energy skymap produced by me. The PSF is shown on the bottom left side of the plot.

The final outputs of the high level analysis can also be lightcurves and spectra. In order to produce them there are several programs that need to be run and several quantities that need to be calculates. In the first one, called `flute`, the differential flux is calculated as the number of photons per unit time, area and energy;

$$\frac{d\Phi}{dE} = \frac{dN_\gamma(E)}{dt\, dA\, dE} \tag{2.10}$$

The integral flux is computed in a determined energy interval $[E_{thr}, E_{max}]$:

$$\Phi_{E_{\rm thr}<E<E_{\rm max}} = \int_{E_{\rm thr}}^{E_{\rm max}} \frac{d\Phi}{dE}\, dE \qquad cm^{-2}\, s^{-1} \tag{2.11}$$

The lightcurve shows the evolution in time and energy of the integral flux. The last important quantity is the Spectral Energy Distribution, it is defined as:

$$E^2 \frac{d\Phi}{dE} = E \frac{d\Phi)}{d(logE)} \qquad TeV cm^{-2} s^{-1} \tag{2.12}$$

In order to calculate these quantities, three parameters are needed: the effective area A_{eff}, the number of γs and the effective time t_{eff}. The first one is the area within which a γ photon of energy E and angle θ can be detected by MAGIC, and usually it corresponds to the area of the Cherenkov light pool. It is computed using Monte Carlo simulations of γ-rays taht were able to pass the previous filters and it is given by:

$$A_{eff}(E; E + dE) = A_{sim} \frac{N_{sel}(E; E + dE)}{N_{sim}(E; E + dE)} \tag{2.13}$$

with A_{sim} being the simulated area, N_{sell} is the number of simulated events after analysis cuts with energy between E and E + dE and N_{sim} is the total number of simulated events

in the same E_{bin}. Considering a source with a certain spectrum $\frac{d\Phi}{dE}$, the effective area must be weighted on the assumed spectrum:

$$\langle A_{eff} \rangle_{[E_1;E_2]} = \frac{\int_{E_1}^{E_2} \frac{d\Phi}{dE} A_{eff}(E)\, dE}{\int_{E_1}^{E_2} \frac{d\Phi}{dE}\, dE} \tag{2.14}$$

So for the computation of the effective area, it is necessary to give a tentative energy spectrum.
The effective area can be computed in terms of zenith bins and the average value is:

$$\langle A_{eff} \rangle_{[Zd_1;Zd_2]} = \int_{Zd_1}^{Zd_2} A_{eff}(Zd) f(Zd)\, d(Zd) \tag{2.15}$$

with f(Zd) being the ratio between the time spent at a zenith angle Zd over the total time. The effective area depends on second order also on the azimuth.

The number of gamma events N_γ instead is the umber of excess events. The difference with the one computed with odie lays in the fact that the hadronness, θ^2 and size cuts are optimized for each energy bin and are not fixed.

Lastly the effective time of the observation is retrieved by subtracting the DAQ dead time d to the total observation time. If the arrival time of the photons is modelled with Poassonian statistics, the:

$$t_{eff} = \frac{t_{elapsed}}{1 + \lambda d} \tag{2.16}$$

with $t_{elapsed}$ being the time from the beginning to the end of the observation.

The differential spectrum is built in bins of E_{est}, while the effective area is in MC γ E_{true} bins. This can lead to a migration of events, meaning that some events in the bin $E_i < E_{true} < E_{i+1}$ are reconstructed in a different E_{bin} . The method used to solve this problem is the unfolding technique. The one used in flute is called poor man unfolding, the events number padding the cuts for the calculation of the effective area is E_{est} binned. This is good solution just in first approximation, there are several problem left:

- energy resolution is limited: it accounts for a 15% of statistical error;
- the detector's acceptance is limited;
- other secondary effects (e.g. the efficiency is not that of an ideal detector, systematic distortions, etc...).

The unfolding technique actually is able to overcome these issues. The problem can be mathematically formuled with the Fredholm integral equation:

$$g(y) = \int M(x,y) f(x)\, dx + b(y) \tag{2.17}$$

with f(x) being the distribution of the desired parameter (E_{true}), g(y) is that of the known parameter (E_{est}), M(x,y) is the migration matrix and b(y) is the random noise due to the

measurement. Instead of integrating, so using a continous variable, it is possible to dicretize the computation:

$$g_i = \sum_j M_{ij} f_j + b_i \tag{2.18}$$

In order to find f_j we need to invert the equation, but this is not always possible. Another approach is with the least square minimization. Starting with:

$$\chi_0^2 = \left(\vec{g} - \mathbf{M}\vec{f}\right)^T \mathbf{V}[\vec{g}\,] \left(\vec{g} - \mathbf{M}\vec{f}\right) \tag{2.19}$$

This method works only for points that are distributed following a Gaussian statistics and for bins with a large number of events. Furthermore, $\vec{f}$ oscillates a lot, needing then a regularization. The macro, in MAGIC, that applies these unfolding technique is called `CombUnfold.C`, in particular there are several methods available to perform the regularization (e.g. Bertero, Tikhonov, Schmelling). A simpler version of this technique is called forward unfolding, that sets a few parameters and then minimizes the χ_0^2. This method can be performed with either `CombUnfold.C` or `fold`. The latter is a MARS program that retrieves spectra with the forward-folding Poissonian likelihood maximization. It takes flute results as inputs and it computes the best parameters for the source intrinsic spectrum.

Chapter 3

PG 1553+113 MAGIC analysis

As discussed in the previous section, Monte Carlo simulations are divided into different observational periods to take into account hardware changes/issues and other factors in order to build an optimal Instrument Response Function. During this work the following observational periods have been analyzed:

- ST.03.12 (16/09/2019 - 22/02/2020)
- ST.03.11 (01/11/2018 - 15/09/2019)

In order to check the correctness of the produced Random Forest, the analysis on the Crab Nebula data is needed. In γ-ray astrophysics it is considered to be the standard candle, due to its stable and strong emission of VHE γ-rays.

3.1 ST0312

The ST.03.12 period is the one that extends from the 16^{th} of September 2019 up to the 22^{nd} of February 2020. No big hardware changes where performed from one period to the other. In order to build the RF I first selected the observations of the PG 1553+113, in order to look for the correct MCs in terms of Zenith angle distributions. During this period the PG1553+113 was observed just 4 times, as shown in Tab. 3.1

date	Zenith range (deg)	Observation time (hrs)
27/01/2020	30° - 50°	$\sim$ 1.2
30/01/2020	30° - 40°	$\sim$ 1.2
02/02/2020	30° - 45°	$\sim$ 2.3
06/02/2020	30° - 35°	$\sim$ 0.5

Table 3.1: Dates when PG 1553+113 was observed by MAGIC during the ST.03.12 period, the second column shows the zenith angle distribution while the third shows the time of the observation

The good quality data was chosen with the following criteria:

- Transmission at 9 km$>$ 0.8;
- Cloudiness $<$ 0.3;
- M2 DC $<$ 2200 μ A;

- L3 rates from 150*A up to 400*A, with A being $\cos(\mathrm{Zd})^{-0.35}$, a factor that takes into account the zenith angle dependency of the rates.

After the having found the good observational date, the next step was to directly download the corresponding superstar files in order to apply quate cuts to the data, with the result, having chosen already good measurements, that all the runs passed the filters.
The next step is to retrieve and separate the MC simulations. It is possible check these files on the MAGIC wiki page and obtain them from the PIC server. The one chosen by me where of the type wobblering mmcs699 and wobblering mmcs6500, and as previously discussed, they have been divided into train and test Monte Carlos. The zenith rage of the simulations spans from 5° up to 62° due to the fact that before performing the PG1553+113 analysis, I performed the one on the Crab in order to learn how to treat MAGIC data, and during one of the three days of crab observation, one had a zenith angle $> 50°$ so I had to use MC up to 62°.
The files where directly obtained in the superstar format, and for each zenith range, there are 2 files, one denoted with 1 and the other with 2, so in total 12 files 6 for train MC and 6 for test MC were downloaded. the distribution of the files is shown in Tab. 3.2.

mmcs	Zenith range (deg)	train	test
699	5° - 35°	2	1
6500	5° - 35°	2	1
699	35° - 50°	1	2
6500	35° - 50°	1	2
699	50° - 62°	2	1
6500	50° - 62°	2	1

Table 3.2: Distribution of the MCs between test and train. The label 1 and 2 is the same as the one done at the PIC.

After the selection of the Monte Carlo simulations, the next and longest step, is to choose the OFF data. Their properties should be of having good data quality conditions, being of the same type of the source that is analyzed, being observed during the same period, should not have a significant γ emission and cover the same zenith angle. The last three conditions are the ones that need to be followed strictly. Furthermore the amount of time that the OFFs cover should be at least equal to the observational time of the source. Three sources were selected: 4C+39.12, B2-1420+32 and GRB200216B with a total observation time of $\sim$ 13 hrs. By having both OFFs and train MCs, the follow up task is the RF production using coach. In order to check if the RF is correct or not, it is important to test it using a standard candle, that in the case of γ-ray astrophysics is the Crab Nebula.

3.1.1 ST.03.12 Crab check

The data selected for the Crab check of the RF were taken during three days of the ST.03.12 period, as shown in Tab. 3.3.

The data quality conditions are the same as the ones for PG 1553+113. Then melibea was run in order to produce the files ready to be analyzed up to the high level. The first important outputs that have been produced are the θ^2 plots at the three energy ranges

From both Fig. 3.1 and Fig. 3.2 it is possible to observe the significance of the signal from the Crab in two different energy ranges: LE adn FR. In all of these ranges the significance

date	Zenith range (deg)	Observation time (hrs)
17/01/2020	10° - 55°	~ 4
18/01/2020	5° - 50°	~ 3
19/01/2020	15° - 45°	~ 2.5

Table 3.3: Dates of Crab Nebula data chosen for the Crab check of the RF for the ST.03.12 period

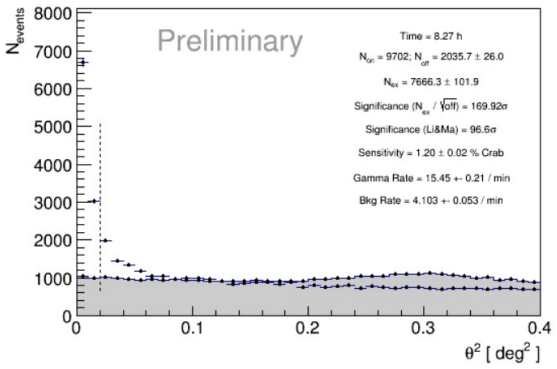

Figure 3.1: LE θ^2 plot for the Crab Nebula

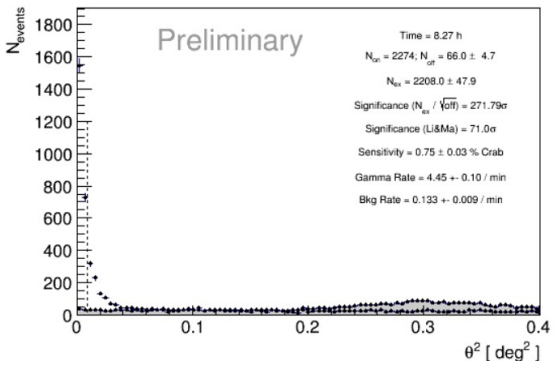

Figure 3.2: FR θ^2 plot for the Crab nebula

is very high, $\sim 100\sigma$ for the LE, while 71 σ for the FR. Another characteristic is the small bump at 0.3deg^2 at all ranges, this is due to the fact that the Crab is very bright so there is an excess in that region.

Another important plot is the skymap, and it is produced with caspar. Here it is shown in two different ways, the first one being the distribution of the TS value in the FoV while the second one is the number of events versus the TS values.

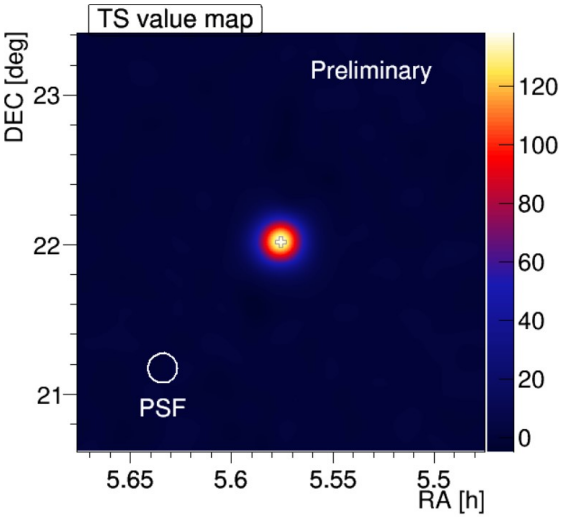

Figure 3.3: LE skymap for the Crab Nebula

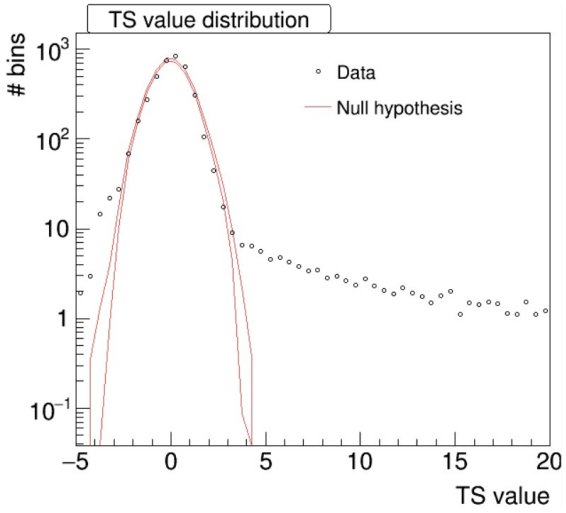

Figure 3.4: LE TS histogram

The Fig. 3.4 is very meaningful, the full red line is the null hypothesis that represents the background. It has ,as shown in the plot, a Gaussian profile. Then after TS ~ 4.5 there are some events that do not follow the trend anymore, and those bins represents the actual source emission. Furthermore, from Fig. 3.3, the TS distribution of the Crab emission on

the camera is actually bigger that the PSF itself, this is due to the fact that the Crab can eject numerous γ events. Lastly it is important to notice that in order to say if a source detection is significant or not, the only valid instrument is the θ^2 plot, skymaps are useful to check the PSF of the instrument.

Lastly the final graphical outputs are the LC and SED. Both of them are produced using flute, but just the latter can be further developed using either fold or CombUnfold.C. It is very important that, in both plots, there are reference values of the Crab emission, meaning that if something is wrong with the reconstruction through the RF, then it is visible in these plots.

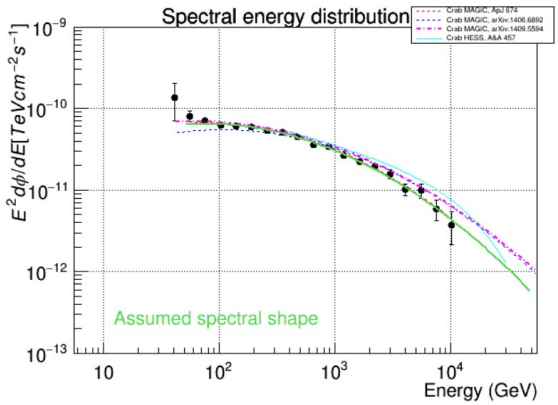

Figure 3.5: SED of the Crab Nebula

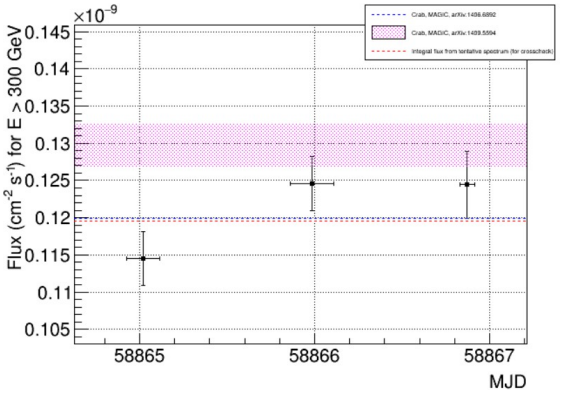

Figure 3.6: Night-binned lightcurve of the rab nebula

As shown in Fig. 3.5, the SED follows a LogParabola trend. This, as previously discussed is given as input in flute, and for the Crab is the default spectral shape that is:

$$\frac{d\Phi}{dE} = \left(\frac{E}{300\,GeV}\right)^{-2.31-0.61\,log10\left(\frac{E}{300\,GeV}\right)} \tag{3.1}$$

with the factor 300 GeV that is the normalization factor. The green line in the plot represents this shape, while the other lines describe the Crab behaviour analyzed in previous papers. Instead Fig. 3.6 shows the lightcurve above 300 GeV night-binned, not only that, even the integral flux from the tentative spectrum and other two from previous papers. If for both SED and LC, the data points match the previous results, impyling that the RFs are correct and they can be applied to real data.

3.1.2 PG 1553+113 high level results

As soon as the Crab check is finished, then I proceeded with the analysis of the PG 1553+113 data, by running first melibea. Then the θ^2 plots were produced. Unlike the previous θ^2s from the Crab Nebula that showed a much larger significance, here it is drastically lower and for the Full Range, Fig. 3.8, there is just background and nothing from the source. This is caused by the great distance of PG 1553+113, so the photons above ∼300 GeV pair product with EBL photons, reducing the observed flux.

Then the sky map was produced using caspar.The results are displayed in Fig. 3.9 and show the presence of the source at the center of the camera, as expected.

Lastly the final graphical outputs are the SED and lightcurve. There is a significant distinction when comparing these plots with those of the Crab. This distinction lies in the

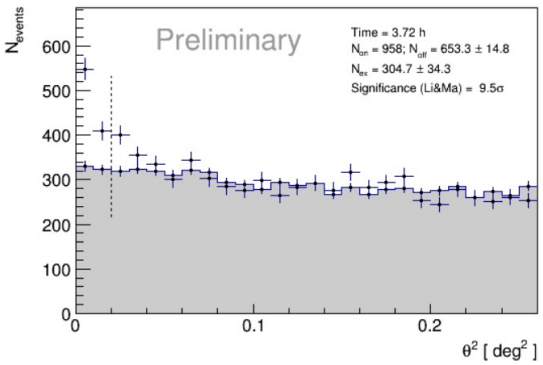

Figure 3.7: LE θ^2 plot for the PG1553+113

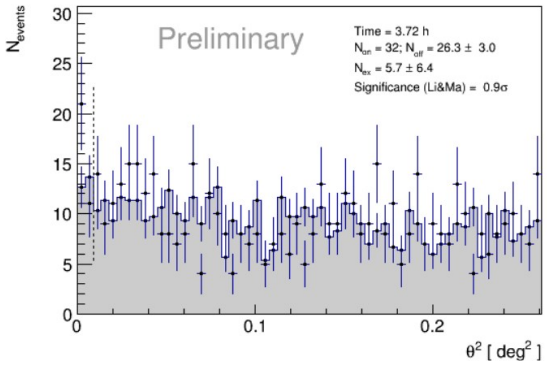

Figure 3.8: FR θ^2 plot for the PG1553+113

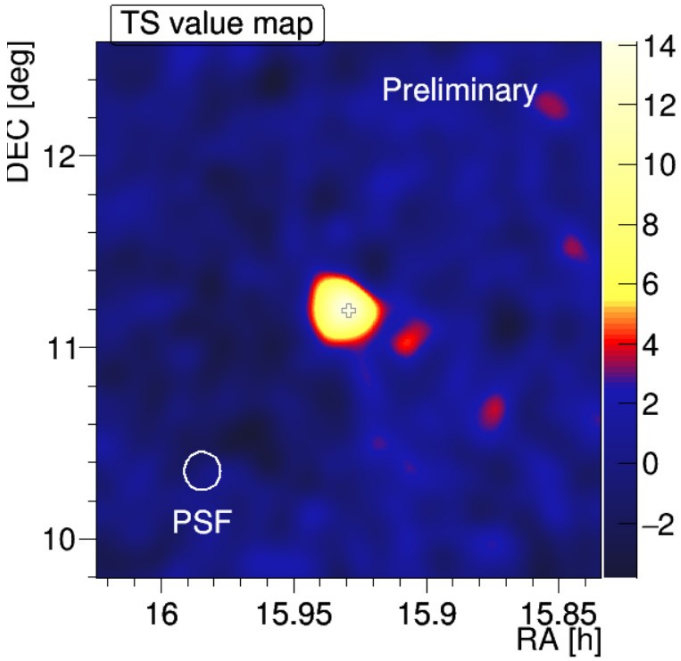

Figure 3.9: Low energy sky map of the source PG 1553+113

presence of upper limits in both figures. They are computed, when in a bin the signal is not enough for it to be significant. This can happen if the observation is not long enough or if the source is not strong. The imputed maximum relative error before the construction of an upper limit has been set to be the standard one, so 0.5 .In this case, the reason is that the PG 1553+113 is not in a particular high state, so the received signal is not enough. Furthermore, as shown in Fig. 3.11, the energy threshold for the integral flux computation (eq. 2.11) has been lowered to 150 GeV. The reason behind the choice of thi senergy threshold is not only because it is the standard one for this type of sources, but even to compare these results with previous works.

In order to produce better results, the unfolding technique has been applied. In particular the program fold was run, using the forward unfolding method. The program takes as input the flute output, and type of spectral shape, in this case the power law model was assumed so:

$$\frac{d\Phi}{dE} = f_0 \left(\frac{E}{E_0} \right)^{-p} \tag{3.2}$$

with E_0 being the normalization energy, f_0 normalization constant and p the spectral index.

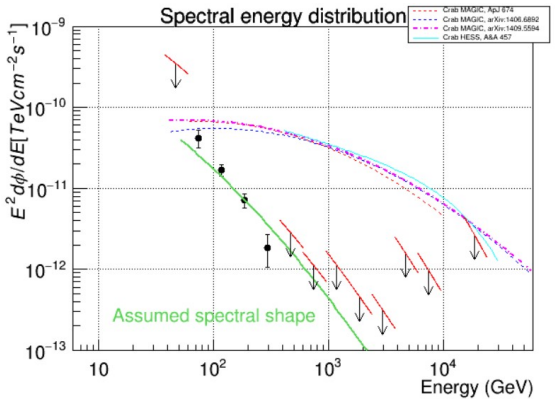

Figure 3.10: SED for the PG1553+113

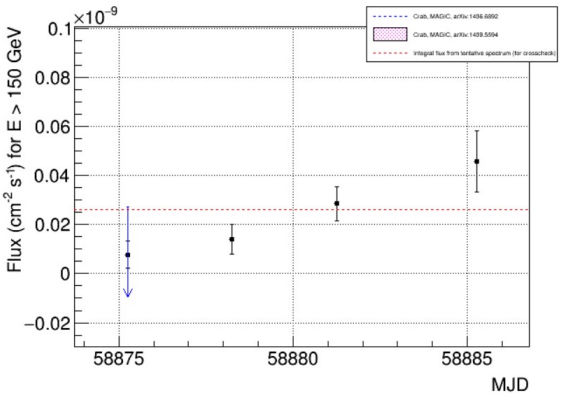

Figure 3.11: Lightcurve for the PG1553+113

In fold the normalization energy is suggested by the program itself in order to minimize the correlation between the spectral parameters, while the last two parameters are fitted with the data, the results are shown in table... . Other two important inputs of fold are the redshift and the EBL model, in this case the redshift of 0.433 has been chosen while the EBL model is that of Dominiguez (Domí nguez et al., 2010). The program fit the deabsorbed points with the power law shape, instead of the observed ones.

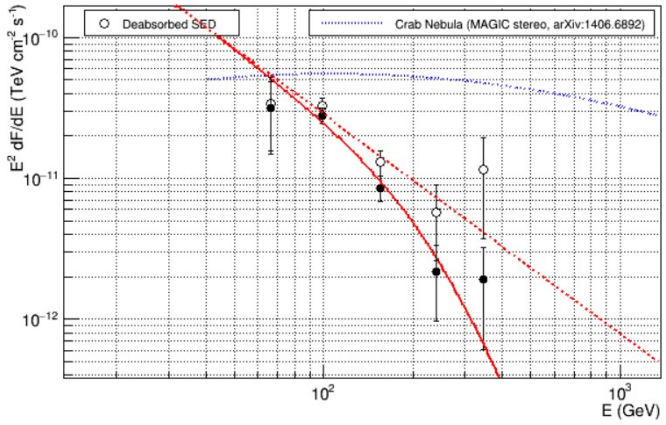

Figure 3.12: SED of PG 1553+113 produced using fold. The full circles are the observed points, while the empty ones are the deabsorbed bins usnig z=0.433 and EBL model DOminiguez 2011.

The results of the fit performed by fold are shown in Tab. 3.4. Another useful plot, in order to check if the fit is correct or not is the one showing the residuals, this is shown in Fig. 3.13. The fit actually shows good results, as it can be seen from both residuals and reduced χ^2.

$f_0 \cdot 10^{-9}$	p1	Normalization energy (GeV)	χ^2	dof	reduced χ^2
1.12 ± 0.12	3.3 ± 0.3	130.95	7.6	10	0.76

Table 3.4: Fit results from fold of PG1553+113 during the ST.03.12 period

3.2 ST0311

The ST.03.11 period is extends from the 1^{st} of January 2018 up to the 15^{th} of September 2019. No significant changes were done from the previous period. During this work a lot of focus was given to the data observed during those months, due to the fact that the source

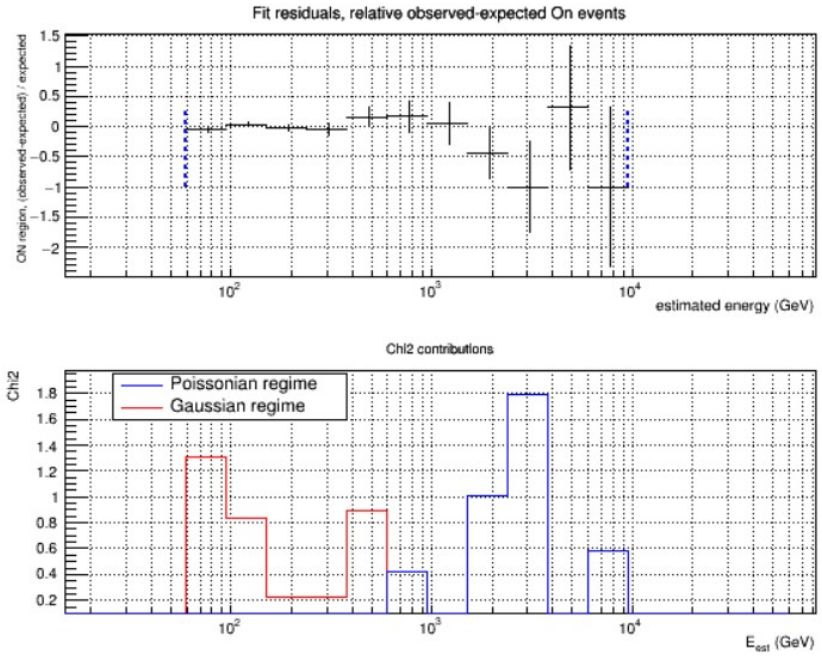

Figure 3.13: Residuals of the fit of the PG 1553+113 SED during the ST.03.12 period, produced using fold.

had a flaring activity in April 2019, as expected from the periodicity of ∼2.2 yrs. During ST.03.11 the PG 1553+113 was observed for several days with a total amount of 37.7 hrs, but due to mostly moon observations and bad Transmission the cumulative observation time was reduced up to 19.7 hrs, the surviving days with the amount of hours are shown in Tab. 6.5

The following cuts were used in quate in order to select the good runs:

- Transmission at 9 km$>$ 0.8;
- Cloudiness $<$ 0.3;
- M2 DC $<$ 2200 μ A;
- L3 rates from 150*A up to 400*A, with A being $\cos(\mathrm{Zd})^{-0.35}$, a factor that takes into account the zenith angle dependency of the rates.

After having retrieved the superstar files from the PIC, the following step was to obtain the MCs. As it was done for the previous period, the files were of both types wobble ring mmcs 699 and wobble ring mmcs 6500, and then further separated in train and test MC. The zenith distribution of the MCs has been chosen to range from 5° up to 62° due to the fact that, as shown in Tab. 6.5, on the 25^{th} of June 2019 the obeservations were performed up to 55°, so MCs up to 62° are strictly needed. The data were chosen in order to be taken just on dark time, so both the analysis and the MCs could start from the superstar level. The selection was performed as for the previous period, with the difference that the number 1 and 2 have been switched between train and test, as shown in Tab. 3.5.

Then the selection of the OFFs was performed, considering the amount of time of the PG 1553+133, that is $\sim$ 6 times larger than the total time for the previous period, implying a larger amount of OFF time. In this case I selected the following sources: NGC1275, TXS2010+463, 3C-264, Perseus-MA, S50716+714, GRB181225A, NGC1068, xHWCJ1039+30, GRB230319, M87, FL8YJ1253.7, IC-190503, 2FHLJ2209.8, PKS1510-089, B2-2234+28A, B2-1420+32, CGRaBSJ0211+, HESSJ1943+21, S20109+22, PKS1413+135.

mmcs	Zenith range (deg)	train	test
699	5° - 35°	1	2
6500	5° - 35°	1	2
699	35° - 50°	2	1
6500	35° - 50°	2	1
699	50° - 62°	1	2
6500	50° - 62°	1	2

Table 3.5: Distribution of the MCs between test and train for the period ST0311. The label 1 and 2 is the same as the one done at the PIC.

The total amount of time for the OFFs before applying quate quality cuts, taht were the same as the ones for the PG1553+113, was of 77.5 hrs, while afterwards it was reduced to 50.0 hrs. The production of the RF was performed using coach with standard settings.

3.2.1 ST.03.11 Crab check

The data that were selected for the Crab check of the RF for the ST.03.11 period is shown in Tab. in the appendix. The observation dates covered almost all the ST.03.11 period, ranging from December 2018 up to April 2019, with a total amount of observation time after the quate cuts of 17.06 hrs. The filters imposed with quate are the same that were used for the PG1553+113. The the plots showing the significance were produced, so the θ^2 plot and the sky map, with respectively odie and caspar:

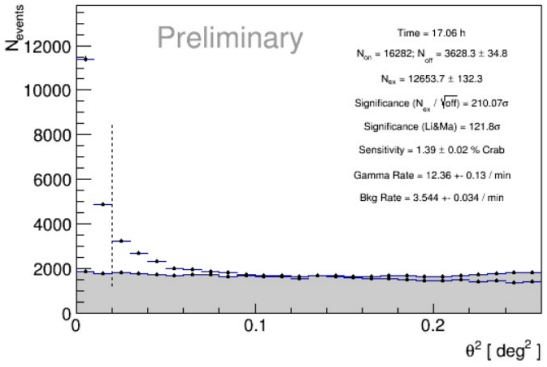

Figure 3.14: LE θ^2 plot for the Crab during the ST.03.11 period. Here all the observation are stacked.

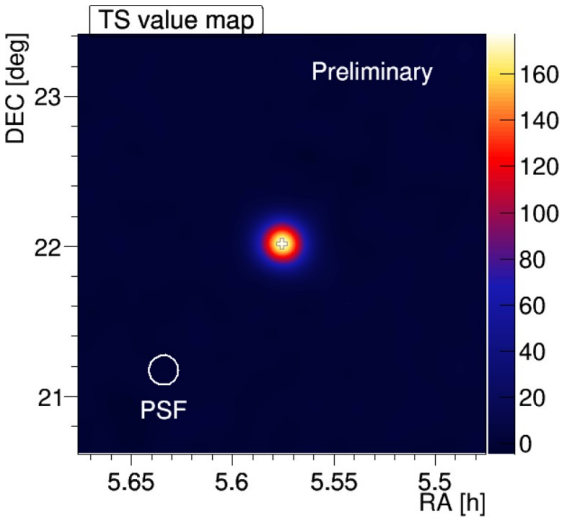

Figure 3.15: LE skymap for the Crab during the ST.03.11 period. Here all the observation are stacked

As it is possible to see from these two figures, the significance of the detection is extremely high ($\sim$ 120 σ), that is typical of the Crab nebula, especially if these many hours of observations are stacked together. Then the production of both LC and SED with flute allows to check the consistency of the emission with previous works

As it is shown in both figures, the emission of the Crab follows the expected models, meaning that the RF was correctly produced. The function used for the spectral shape was assumed

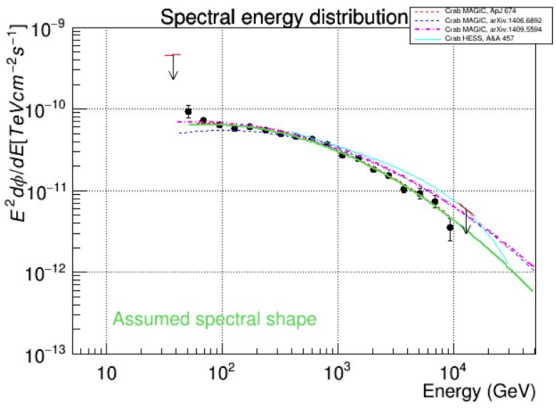

Figure 3.16: SED for the Crab during the ST.03.11 period

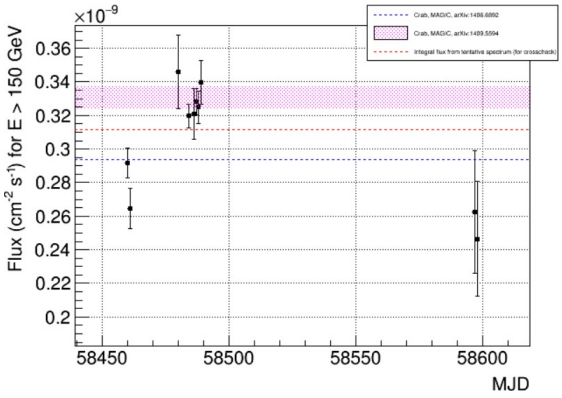

Figure 3.17: Lightcurve for the Crab during the ST.03.11 period

to be the same one as Eq.45 .

3.2.2 PG 1553+113 high level analysis

As soon as the correctness of the RF was confirmed through the Crab check, the further analysis of the PG 1553+113 superstar files was performed using melibea. Furthermore the θ^2 plots were produced.

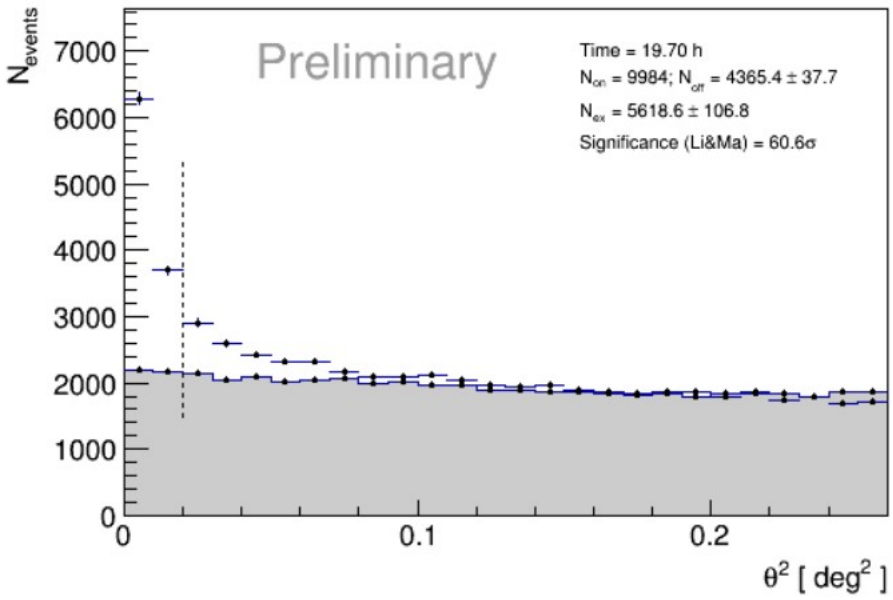

Figure 3.18: LE θ^2 plot for the PG 1553+113 during the ST.03.11 period. Here all the observation are stacked.

As shown in Fig. 3.18, the significance has increased by a factor 6 compared to the θ^2 plot of the previous period while the observation time has increased instead of a factor 5. This is due to the fact that a great weight in the significance computation has been given by the 5 days of flaring activity observed in April, 7-8-9-10-12/04/2019. In the next sections the attention on the analysis will go to these days due to the strong signal cause by the flare episode.
The caspar results showed, as expected, with a higher TS distribution compared to that of the previous period, as shown in Fig.

The next step was the production of the LC and SED with flute. The differences with

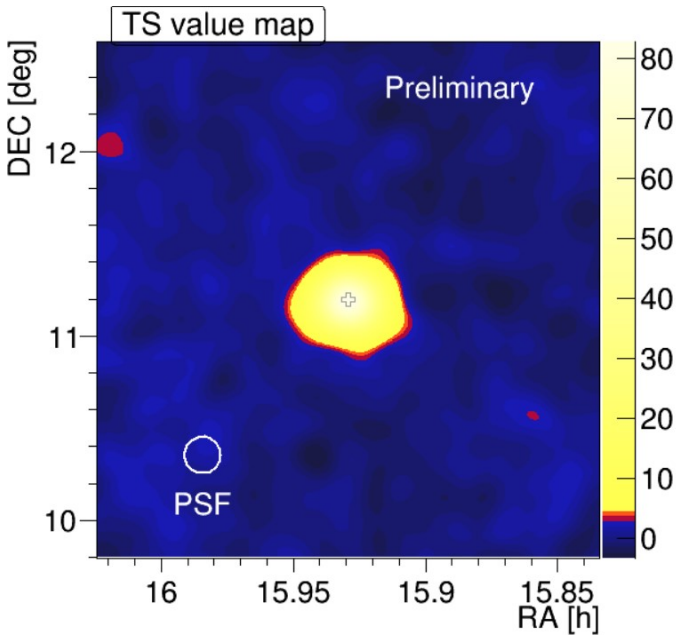

Figure 3.19: LE skymap for the PG 1553+113 during the ST.03.11 period. Here all the observation are stacked.

respect to the ST.03.12 period are evident in this case. As shown in Fig. 3.23, the number of energy bins has increased a lot, from 4 during the ST.03.12 up to 10 in this period. The assumed spectral shape is that of a power law, with spectral index of 3.5. The limits of the binning here is again due to the EBL absorption. The lightcurve, Fig. 3.24 is computed, as done previously, above 150 GeV. It is possible to observe not only many more days of observations, but even the flaring event in between MJD 58570 and 58600, so between the end of March and the end of April 2019.

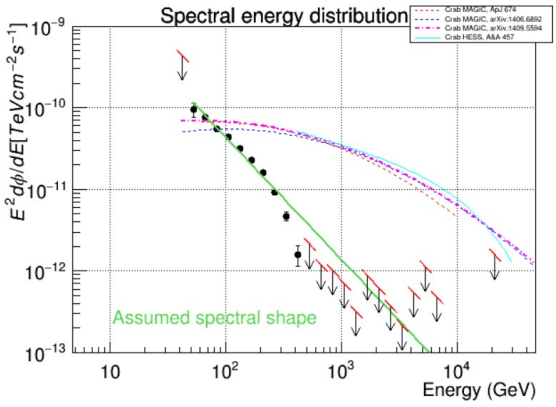

Figure 3.20: SED for the PG1553+113 during the ST.03.11 period. The assumed spectral shape is that of a power law with spectral index of 3.5

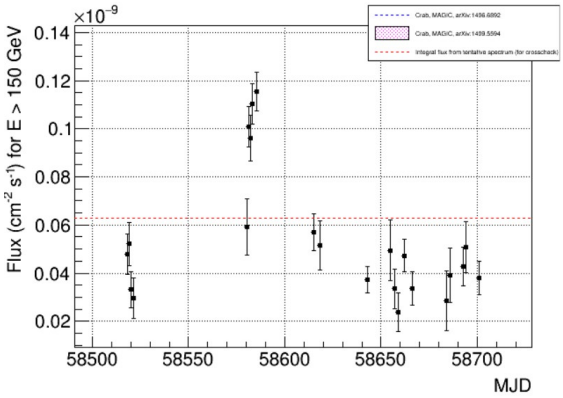

Figure 3.21: Lightcurve for the PG1553+113 above 150 GeV during the ST.03.11 period. The flaring episode of April 2019 is clearly visible comparing those days with the less active ones

In the MAGIC collaboration, it is common practice that an independent cross-check analysis is performed to verify to correctness of the results. In my case, the PG 1553+113 flute analysis of the ST.03.11 period, was already performed by Dr. Paolo Da Vela. As it can be seen in Fig. 3.24, the flux points produced by myself match very well with that of Dr. Da Vela. There are differences with some data points, in particular regarding the number of plotted nights. This difference is due to a difference in the quate cuts between my analysis

and that of Dr. Da Vela.

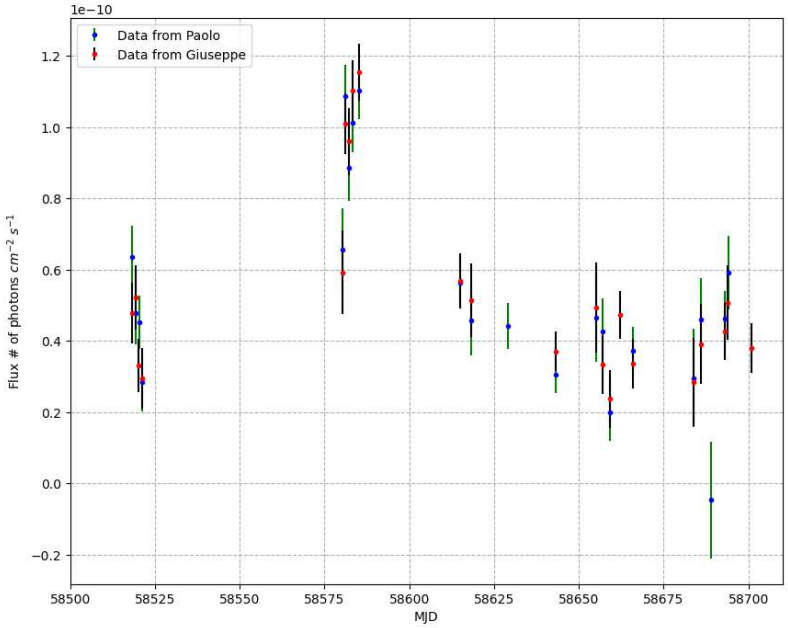

Figure 3.22: Comparison of LC above 150 GeV of PG 1553+113, produced by me (red points) and Dr. Paolo Da Vela (blue points). The match between these two analysis is good, but some data points differ due to a mismatch in the cuts on the observed runs.

The next step is the correction of the SED using the unfolding technique, using the program fold. The data was EBL deabsorbed with the same model as before, so Dominiguez 2011 and the same value of redshift, z=0.433. The power law model was used to fit the EBL corrected data points, as shown in Tab. 3.6, obtaining a good description of the unfolded SED.

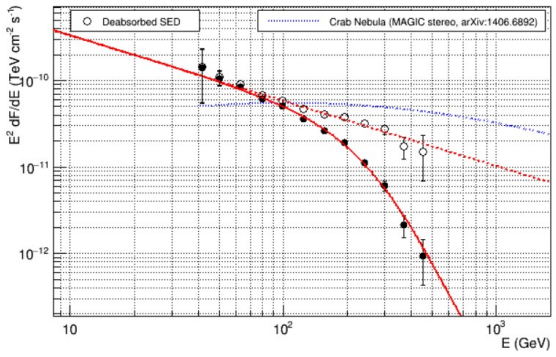

Figure 3.23: SED for the PG1553+113 during the ST.03.11 produced using the forward unfolding with the program fold. The data has been corrected for EBL absorption with redshift z=0.433 using the Dominguez 2011 model.

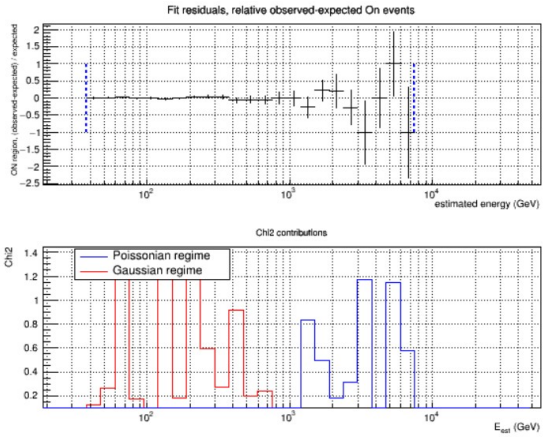

Figure 3.24: Residuals of the powerlaw fit of the SED of PG 1553+113 performed with the program fold

3.2.3 Comparison between the flaring and the quiescent days

The analysis shown previously, is performed on all the observation days stacked together. It is of great significance, not only to perform these type of analysis but even doing the same but day by day, in order to see the variability properties of the PG 1553+113. In particular, to check if the variability is in the spectral index or other parameters.

$f_0 \cdot 10^{-9}$	p1	Normalization energy (GeV)	χ^2	dof	reduced χ^2
2.56 ± 0.05	2.75 ± 0.05	134.95	11.81	21	0.6

Table 3.6: Fit results from fold on the data of the ST.03.11 period

First of all it is important to compare the days with the highest signal to those with the lowest, the full analysis has been done day by day for every date, but in this section just there will be a comparison between just the 12^{th} of April 2019 and the 30^{th} of July 2019 to show the differences between a flaring day and a day where no flare is detected.
Starting with the θ^2 plots of the two days

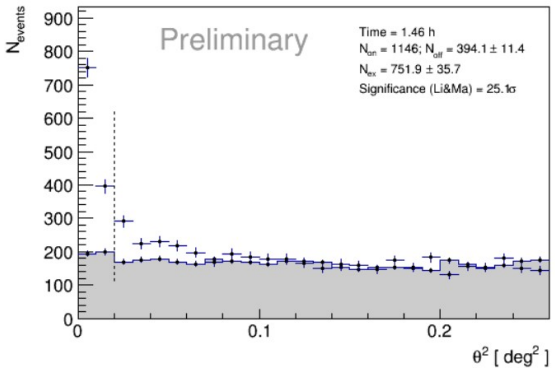

Figure 3.25: LE θ^2 plot for the PG1553+113 with the data taken on the 12^{th} of April 2019.

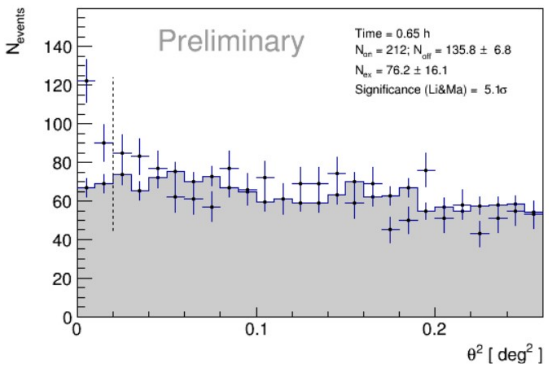

Figure 3.26: LE θ^2 plot for the PG1553+113 with the data taken on the 30^{th} of July 2019.

As it can be seen in both Fig. 3.25 and Fig. 3.26 the signal is still considerably high, compared to the time of the observations. The total time of the runs of the 12^{th} is ~ 2.5 that of the 30^{th} but the signal is 5 times more, meaning that the source was in a particularly high state. It is important to notice, and in the next sections it will be explained better, that the signal on the july date is not low at all, so the source is still active.

The next step is to check the SEDs and the LCs using flute. Regarding the former, as shown in both Fig. 3.27 and Fig. 3.28, number of energy bins for the flare day is way superior compared to the july observation, furthermore a difference lays in the spectral index of assumed power law. For the 12^{th} the value is 3.0 while for the 30^{th} is 3.5 a feature that is common for the flaring days.

Regarding instead the lightcurves the first difference that can be noticed from Fig. 3.29 and Fig. 3.30 is that the flux, as expected from a flaring state, is higher for the 12^{th} compared otthat of the 30^{th}. Another important aspect is that the time binning has been done run-wise instead of night-wise, this is done on order to check the signal evolution in smaller timescales. Furthermore the nigh-binning option sums and averages the signal from each run.

The last remaining step is to unfold the spectrum using fold. The fit results are shown in Tab. 3.7

Regarding the SEDs both are corrected for the EBL with the Dominiguez 2011 model for a redshift of 0.433. The difference between the two days, as it can be seen from the values of the normalization factor, is that the SED of the 12^{th} is higher compared to that of the other day. The spectral indices, unlike flute results, are compatible with the errors. This

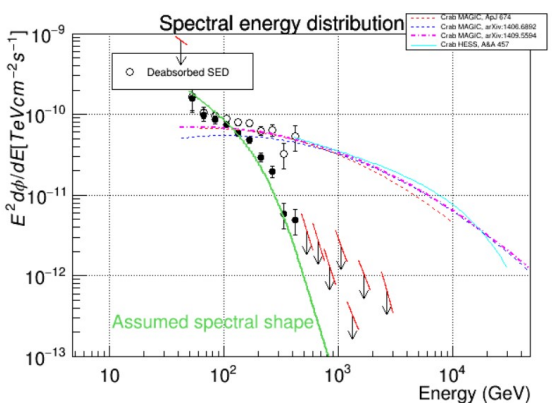

Figure 3.27: SED of the PG1553+113 with the data taken on the 12^{th} of April 2019.

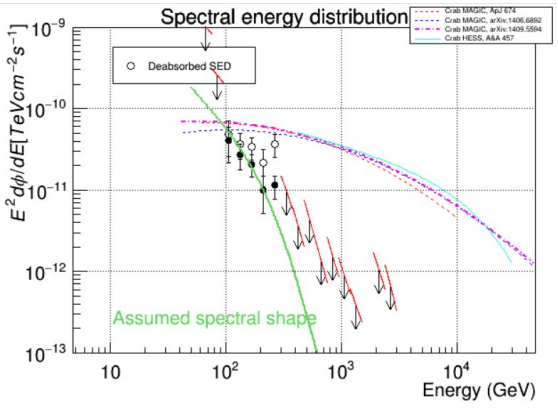

Figure 3.28: SED of the PG1553+113 with the data taken on the 30^{th} of July 2019.

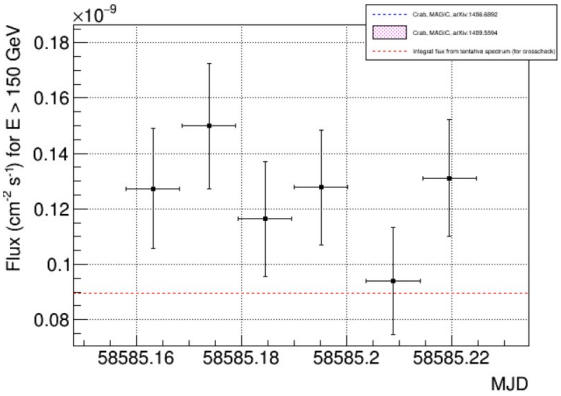

Figure 3.29: Run-wise lightcurve above 150 GeV of the PG1553+113 with the data taken on the 12^{th} of April 2019

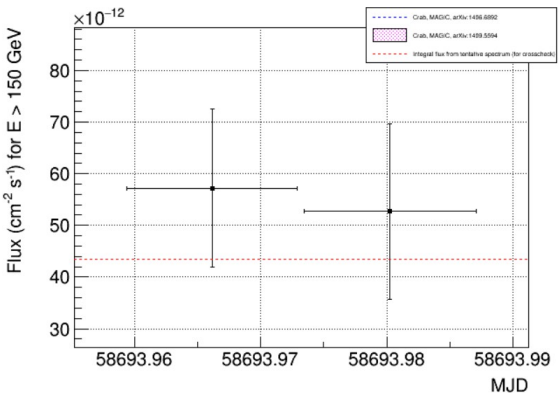

Figure 3.30: Run-wise lightcurve above 150 GeV of the PG1553+113 with the data taken on the 30^{th} of July 2019

is due to the fact that in flute, the spectral shape that is inputed is the intrinsic one, so before EBL correction, while fold fits the power law model on the deabsorbed data points.

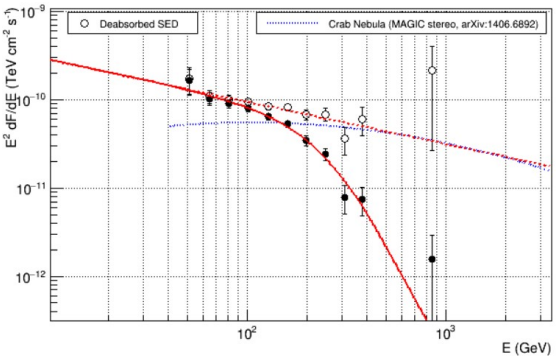

Figure 3.31: SED for the PG1553+113 using fold with the data taken on the 12^{th} of April 2019

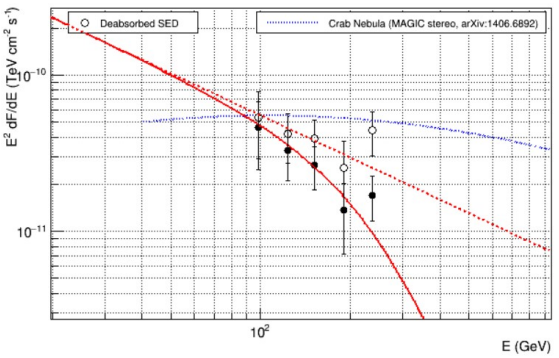

Figure 3.32: SED for the PG1553+113 using fold with the data taken on the 30^{th} of July 2019

3.2.4 Search for intranight variability

A characteristic of Blazars and AGN in general is their high variability, that can range from minutes up to years. It is of great importance to look for signs of intranight variability, so with timescales of either minutes or hours. In order to do so two there are two possible

day	$f_0 \cdot 10^{-9}$	p1	Normalization energy (GeV)	χ^2	dof	reduced χ^2
12/04/2019	4.9 ± 0.2	2.5 ± 0.1	130.95	13.05	17	0.77
30/07/2019	1.1 ± 0.2	2.9 ± 0.5	172.63	14.57	14	1.04

Table 3.7: Fit results from fold on the data of the 12^{th} and that of the 30^{th}

ways:

- Improve the telescope performances: this can be done by modifying the hardware (e.g. bigger telescope) or by having a better discrimination of events (e.g. neural networks);
- Observing a source: this means having a stronger signal, that translate in higher Signal to Noise ratio in the bins to better discriminate episodes of intranight variability.

In this work I used the latter, in the future even the former might be taken into account with the new LST telescopes. The first important thing that needs to be done in order to search for intranight variability is to lower the energy threshold as much as possible. This step is crucial, lowering the threshold too much means getting a lot of contamination from background, worsening the signal to noise ratio. In order to find the lowest energy threshold possible I used a ROOT macro, that, taking as input the configuration file of flute and the spectral index of fold, computes the number of γ events surviving the flute cuts binned with E_{est}. This histogram has a Gaussian peak that is fitted, and the mean value is the lowest energy threshold value. I applied a cross check with the values of effective area and background levels in order to see if the applied energy threshold was correct or not.
The lowest E_{thr} that has been applied to the flaring runs was of 75 GeV, and in order to check the presence of intranight variability I performed a constant fit of the data to see if there is a deviation from the constant model. To see a better evolution of the fit with a changing energy threshold I performed the fit for both $E_{thr} > 100$ GeV, with results shown in Tab. 3.8 , and $E_{thr} > 75$ Tab. 3.9.

date	p0 $\left(cm^{-2}s^{-1}\right) \cdot 10^{-10}$	χ^2	dof	reduced χ^2
07/04/2019	2.50 ± 0.28	2.8	1	2.8
08/04/2019	3.2 ± 0.2	1.3	3	0.43
09/04/2019	3.10 ± 0.21	8.8	2	4.4
10/04/2019	3.70 ± 0.19	5.5	3	1.83
12/04/2019	3.60 ± 0.18	6.4	5	1.28

Table 3.8: Fit values Lightcurve > 100 GeV for the flaring days

The day that is a good candidate for intranight variability is the 9^{th} of April. Its reduced χ^2 is considerably higher that the rest of the dates, reaching a value of 7.5 with a threshold of 75 GeV. The lightcurves of this night at both enrgy thresholds are shown in Fig. 3.33 and Fig. 3.34. There is a trend that is not constant as it can be seen even from the errorbars of the bins. In order to further prove the intranight variability it would be useful to perform these measurement with larger telescopes, that, with lower energy thresholds, will allow for a better discrimination of these types of events. Furthermore it would be very convenient to perform longer observations, in order to check for signs of variability.

date	p0 $\left(cm^{-2}s^{-1}\right) \cdot 10^{-10}$	χ^2	dof	reduced χ^2
07/04/2019	5.2 ± 0.5	0.98	1	0.98
08/04/2019	6.60 ± 0.36	0.74	3	0.25
09/04/2019	6.10 ± 0.37	15	2	7.5
10/04/2019	7.70 ± 0.34	3.3	3	1.1
12/04/2019	6.80 ± 0.31	7.6	5	1.52

Table 3.9: Fit values Lightcurve > 75 GeV for the flaring days

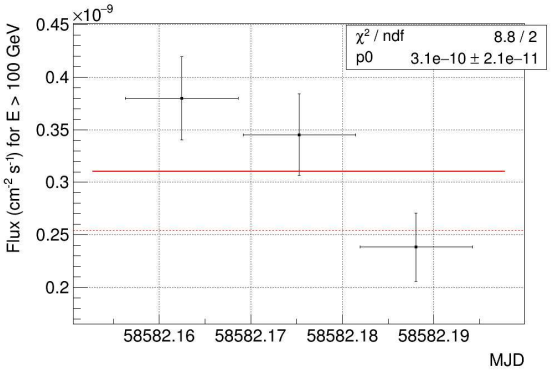

Figure 3.33: Run-wise lightcurve for the PG1553+113 above 100 GeV. The data was taken on the 9^{th} of April 2019 and fitted with a constant function. The fit results are shown on the legend

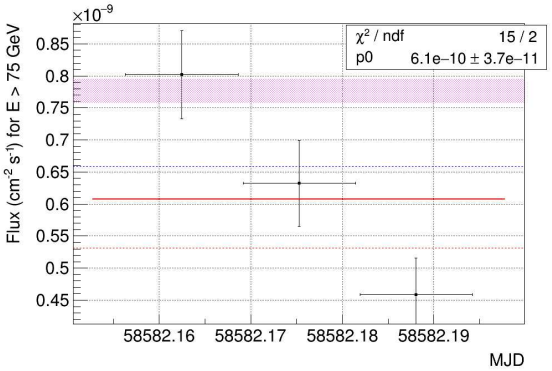

Figure 3.34: Run-wise lightcurve for the PG1553+113 above 75 GeV. The data was taken on the 30^{th} of July 2019 and fitted with a constant function. The fit results are shown on the legend

Chapter 4

Multiwavelength analysis

A crucial step needed for modelling the broad band emission of PG 1553+113 is the analysis of multiwavelength data. Due to the variability of the source, the multivawelength data need to follow a strict criteria, that of simultaneity. It means that the observations should be performed on the closest time window. This condition is very difficult to fulfill but it is necessary due to the variable nature of these objects. Furthermore it depends also on the time resolution of the instrument that makes the observations. In the following sections the wavelength data and instruments that have been used for the construction of the SED of PG 1553+113 will be discussed. This source, observed by MAGIC, has been monitored by several instruments thanks to a follow up proposal by the PI Dr. Elisa Prandini and Dr. Antonio Stamerra that coordinated the data taking.

4.1 Very High Energy γ rays

Regarding Very High Energy γ-rays the only instrument that has been used is MAGIC, and the data have been analyzed as discussed in the previous section. The analysis has been done day by day for each observation of PG 1553+113 up to the flux reconstruction level. The VHE SED data points have been EBL corrected, using the Dominigue 2011 model, and extracted using a ROOT macro. In Tab. 4.1 all the fit outputs of this level have been listed.

4.2 High Energy γ-rays

High Energy γ-ray data have been obtained using *Fermi*-LAT observations. As discussed in the first chapter of this thesis this instrument completes a whole coverage of the sky every three hours. This can be seen from the continuous follow up of PG 1553+113 whose lightcurve is shown in Fig. 4.1. The only problem with *Fermi* observations is that in order to build a significant signal it has to integrate over a time window of at least 3-days, resulting then in an averaging of eventual variability properties of the source on a shorter timescale. From the lightcurve, that in Fig. 4.1 is shown with data from 2009 up to current August 2023, it is possible to clearly see the periodicity of $\sim$2.2 yrs (Ackermann et al., 2015). The lightcurve has been retrieved from the NASA online tool ([1]) with both a 3 day and weekly bins. The SEDs value were not available, so the stadard *Fermi* analysis was performed on the data in order to obtain the spectra of this source. Two datasets were produced, one from the 7^{th} up to the 14^{th} of April 2019 and the other from the 12^{th} of June up to the 8^{th} of August 2019. The reason behind this division will be explained in the next section.

[1] https://fermi.gsfc.nasa.gov/ssc/data/access/lat/LightCurveRepository/

date	p0 $\cdot 10^{-9}$	p1	E_{norm} (GeV)	χ^2	dof	reduced χ^2
04/02/2019	1.7 ± 0.4	2.5 ± 0.3	140.3	9.2	14	0.7
05/02/2019	1.8 ± 0.2	2.5 ± 0.3	143.59	13	12	1.1
06/02/2019	2.7 ± 0.3	3.1 ± 0.3	119.43	16	14	1.14
07/02/2019	3.2 ± 0.5	3.5 ± 0.5	106.44	9.4	12	0.8
07/04/2019	5.1 ± 0.4	2.9 ± 0.2	114.06	9	13	0.7
08/04/2019	4.3 ± 0.2	2.6 ± 0.1	134.01	14	18	0.8
09/04/2019	4.9 ± 0.3	2.6 ± 0.2	125.06	7	12	0.6
10/04/2019	5.9 ± 0.3	2.7 ± 0.1	125.06	8.5	14	0.6
12/04/2019	4.9 ± 0.2	2.5 ± 0.1	130.95	12.7	13	0.98
12/05/2019	2.5 ± 0.2	2.5 ± 0.3	130.95	9.6	13	0.74
15/05/2019	0.85 ± 0.15	2.2 ± 0.5	193.7	9.28	14	0.7
09/06/2019	1.35 ± 0.13	2.6 ± 0.2	143.59	16.4	18	1.17
21/06/2019	1.6 ± 0.3	2.8 ± 0.4	134.01	14.3	13	1.1
23/06/2019	2.9 ± 0.4	3.6 ± 0.3	114.46	22.53	15	1.5
25/06/2019	0.37 ± 0.14	3.4 ± 0.8	198.21	5.4	14	0.4
28/06/2019	0.99 ± 0.12	2.3 ± 0.3	168.2	16.7	18	0.93
02/07/2019	1.16 ± 0.15	2.5 ± 0.4	153.86	13.5	15	0.9
20/07/2019	6.4 ± 1.7	3.3 ± 0.8	78.91	9.4	13	0.72
22/07/2019	1.2 ± 0.3	2.5 ± 0.8	140.32	16.8	11	1.5
29/07/2019	1.9 ± 0.2	2.9 ± 0.3	130.95	26.2	15	1.74
30/07/2019	1.5 ± 0.2	3.0 ± 0.5	157.44	7.57	14	0.54
06/08/2019	2.3 ± 0.2	2.8 ± 0.3	122.21	7	14	0.5

Table 4.1: Fit results from the MAGIC SEDs performed using a power law fit of the data from each day.

Both the SEDs from these two periods are shown in Fig. 4.2 and Fig. **??**, in particular the former has an upper limit, showed with the red line, meaning that the signal was not strong enough on that bin to determine its value.

4.3 X-rays

Regarding X-rays tI considered data from Neil Gehrels *Swift*'s X-Ray Telesope (XRT). First launched by NASA in 2004 as a part of the *Swift* satellite, its purpose is to produce spectra, lighcurves and fluxes of X-ray sources and GRBs. The instrument has a focal length of 3.5 m, effective area of $110cm^2$ at 1.5 keV and an energy range from 0.2 up to 10 keV. The lightcurve has been retrieved using an online tool [2] and it is shown in Fig. 4.4. The flux clearly peaks during April, something that is expected considering the high activity of PG 1553+113 in the X-rays. The telescopes operates in two modes:

- Photon Counting (PC) mode. It is used to count single photons, in particular their

[2] https://www.Swift.ac.uk/user_objects/

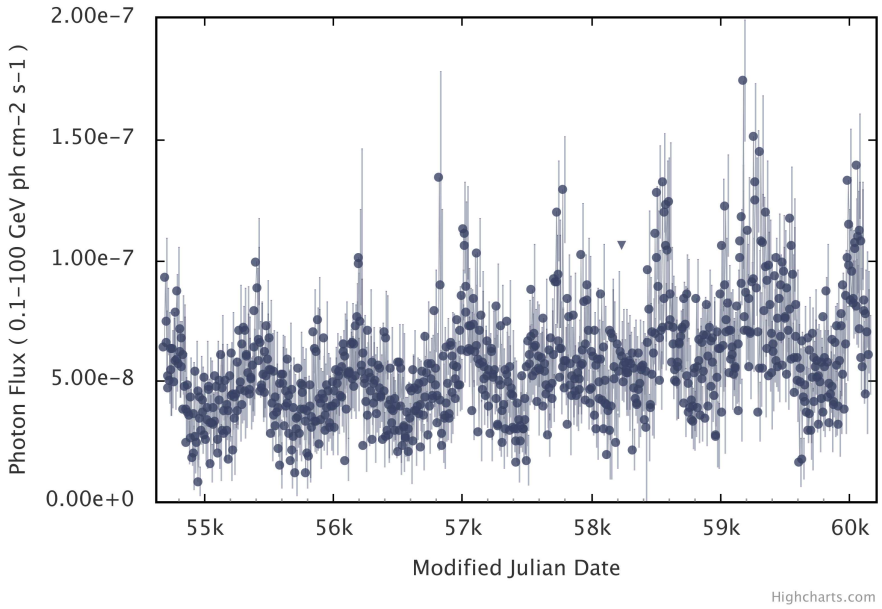

Figure 4.1: *Fermi* 3-days binned lightcurved. The time shown in the plot ranges from 2009 up to August 2023. It is possible to see the periodic behaviour of the source.

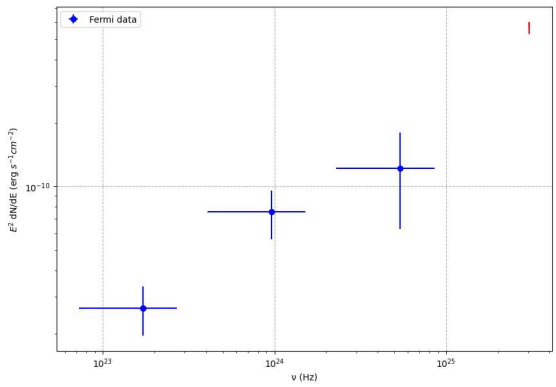

Figure 4.2: *Fermi* SED from averaged from the 7^{th} up to the 14^{th} of April 2019. The red line is an upper limit of the *Fermi* SED. Courtesy of Dr. Axel Arbet Engels.

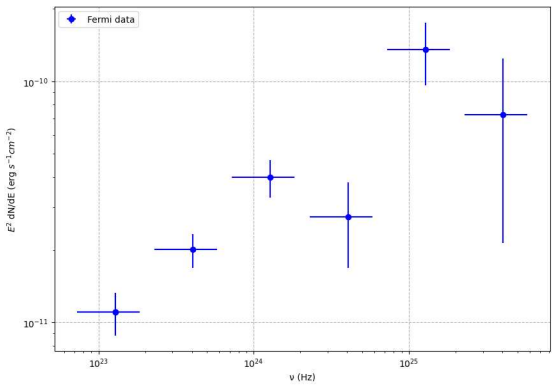

Figure 4.3: *Fermi* SED from averaged from the 12^{th} of June up to the 8^{th} of August 2019. Being averaged over a long period, it was possible to have more bins. Courtesy of Dr. Axel Arbet Engels.

energy and arrival time, in order to produce detailed spectra or to detect faint sources;

- Windowed Timing (WT) mode. The instrument becomes of the time-resolved type doing measurements on the time properties of the photons. This mode is often used in order to see fast variabilities of flaring sources.

During this work the XRT PC data have been analyzed.

Regarding the spectra, they were extracted using a different NASA online tool. The tool basically let you select the observation dates, produces a ds9 like image for each day, and then it is possible to select an ON region. By selecting the energy range, number of bins and the type of spectral shape, it was possible to extract the SEDs for each day. PG 1553+113 is a very bright source in the X-rays, meaning that its XRT observations were affected by the so called pile-up effect. It happens when more than one photon hits the same pixel with an arrival time shorter than the deadtime of the detector, meaning that two or more

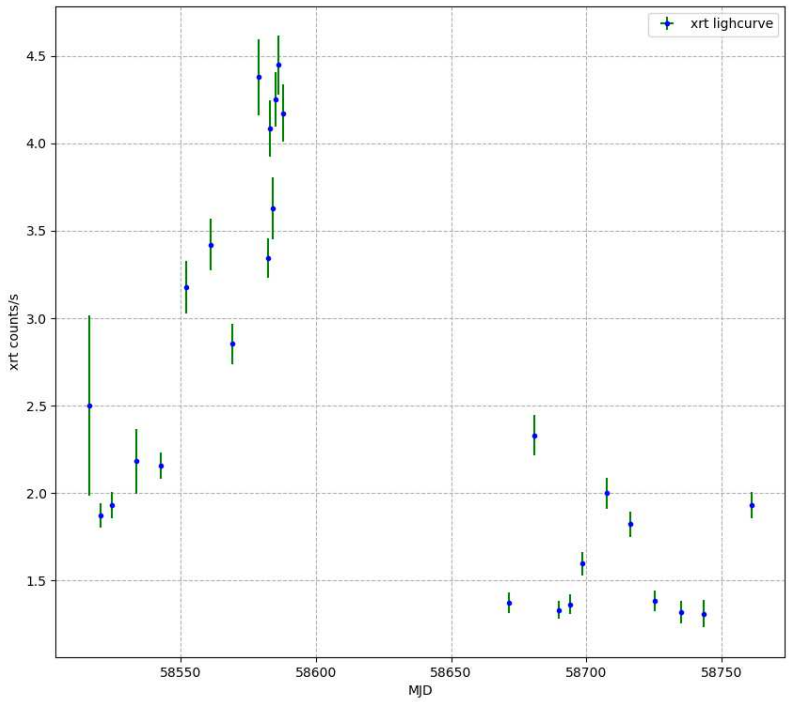

Figure 4.4: XRT lightcurve of PG 1553+113 ranging from January 2019 up to September 2019. The flaring episode is clearly visible during April 2019.

photons cannot be time-distinguished and are counted as a single, more energetic, one. The result is a wrong spectral shape. In order to correct this effect I took an annulus region as an ON, excluding the core pixels. The annulus ON region had an inner radius of 7 pixels and extended up to 30 pixels from the center of the image. The OFF region instead ranged from 70 to 120 pixels from the center. In the end the final SED will be costructed with less events, due to the exclusion of the core region, but will have a correct spectral shape. Another parameter that then was given as input is the mean number density of hydrogen column n_H, this parameter takes into account the absorption of the photons by the material between the source and the observer, with the hypothesis that this material is composed of only hydrogen. This quantity has been retrieved using a NASA online tool [3], resulting in a value for PG 1553+113 of $n_H = 3.6 \cdot 10^{20}\, cm^{-2}$. After having inputed this parameter, the tool needs the assumed spectral shape, the ranges for the flux and sed production, that have been chosen between 0.3 and 10 keV and lastly the number of energy bins. In the end the graphical output of the tool is shown in Fig. 4.5, the fit has been performed with a power law spectral shape including hydrogen absorption, the results are shown in Tab. 4.2. Furthermore the tool gives the value of the integral flux for the selected energy range, and the SED points with the number of bins of choice. In the case of the results shown in Fig. 4.5, the value of the integral flux is $1.03 \cdot 10^{-10}$ ergs/s/cm^2.
The following dates were chosen for the broad band SEDs construction:

- April 2019: 9-10-11-12;
- July 2019: 7-16-25-30;
- August 2019: 3-12;

No other dates were available that were coincident with MAGIC observations.

[3] https://heasarc.gsfc.nasa.gov/cgi-bin/Tools/w3nh/w3nh.pl

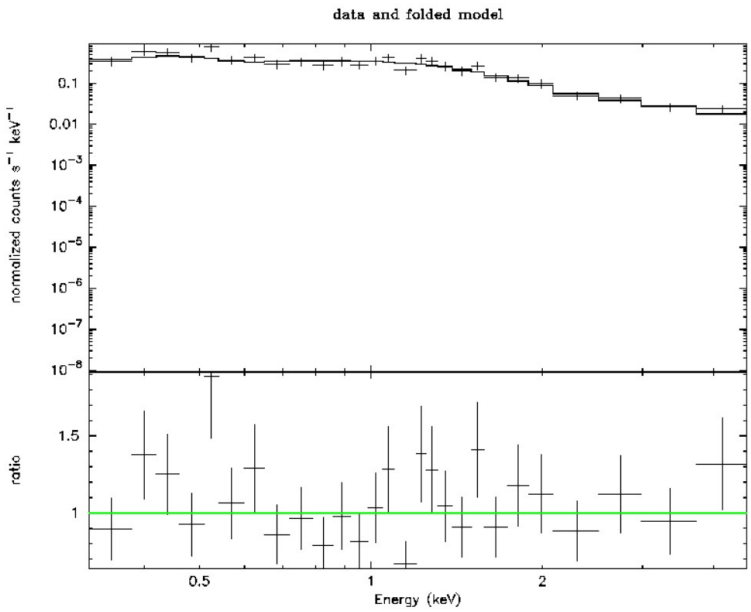

Figure 4.5: XRT integral flux of PG 1553+113 in normalized counts (top panel). This plot shows the observation of the 9^{th} of April 2019. The bottom panel shows the residuals of the fit.

$n_H \cdot 10^{22}$	Γ	Normalization factor ($s^{-1}keV^{-1}$)	χ^2	dof	reduced χ^2
$3.6 \cdot 10^{-2}$	2.20 ± 0.08	$(2.3 \pm 0.1) \cdot 10^{-2}$	25.3	25	1.01

Table 4.2: Results of the fit of the XRT integral flux of PG 1553+113. The fit is done with a power law spectral shape, taking into account the absorption due to the hydrogen column density.

4.4 UV/Optical band

For the UV and optical bands there were two instruments available: *Swift*/UVOT and KVA.

4.4.1 *Swift*/UVOT

Swift's UltraViolet/Optical Telescope (UVOT) [4]is the instrument on board the *Swift* satellite whose purpose is the production of spectra in both UV and optical wavelengths. It has a field of view of 17 x 17 arcmin and can observe objects with a brightness up to 7.4 mag. It has 7 filters, so it cannot produce a continous spectrum, with a wavelength detection from 650 to 170 nm.
The filters wth the respective frequencies, are the following:

- V with $\nu = 5.54 \cdot 10^{14}\, Hz$;
- B with $\nu = 6.91 \cdot 10^{14}\, Hz$;
- U with $\nu = 8.57 \cdot 10^{14}\, Hz$;
- W1 with $\nu = 1.15 \cdot 10^{15}\, Hz$;
- M2 with $\nu = 1.35 \cdot 10^{15}\, Hz$;
- W2 with $\nu = 1.47 \cdot 10^{15}\, Hz$;

[4]https://Swift.gsfc.nasa.gov/aboutSwift/uvotdesc.html

- White has a range that covers all the previous filters.

The effective area of each filter is shown in Fig. 4.6 In this work the observations of PG 1553+113 have been performed with just the first 6 filters. Regarding the analysis there is a NASA online tool that I tested, but the results showed a strange behaviour when plotted in the broad band SED. For this reason the UVOT data were analysed by Dr. Ilaria Viale and Dr. Antonio Stamerra. The available dates were:

- April 2019: 9-10-11-12;
- July 2019: 7-16-25-30;
- August 2019: 3-12.

The April observations where performed with just the UV filters (W1,M2,W2) while the July/August ones with every filter except for the white one.

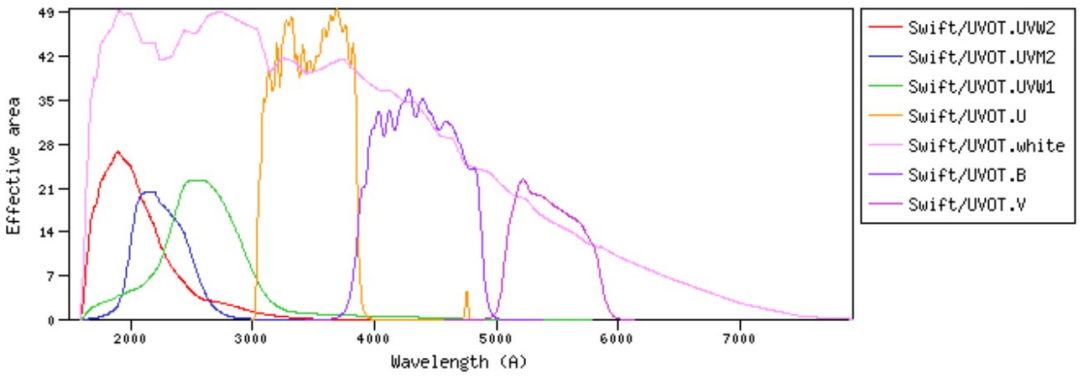

Figure 4.6: Effective area of the seven UVOT filters. 6 out of seven cover a small wavelength range while the white filter covers the range fro 1700 A up to 7000 A. Image taken from `http://svo2.cab.inta-csic.es/svo/theory/fps3/index.php?id=Swift/UVOT.white`

4.4.2 KVA

The Kungliga Vetenskapsakademien (KVA) telescope was located in La Palma on the Observatorio del Roque de los Muchachos. It was composed of telescopes, the first one of 60 cm in diameter and fork mounted while the second was 35 cm in diameter and connected to the first one. The smaller telescope had a FoV of 12x8 arcmin and a focal length of 3.91 m. The telescopes performed measurements in the optical band specifically in the R band, so with an average frequency of $\nu_R = 4.714 \cdot 10^{14}\, Hz$. The data were provided by Dr. Elisa Prandini, PI od a MAGIC multiwavelength proposal on the source which included KVA data,in the form of photometric measurements.

As it is possible to see from Fig. 4.7, plenty of observations were performed during the flare and post flare episode, having several coincident days with both MAGIC, XRT and UVOT measurements

4.5 IR band

Regarding the infrared band, the only instrument available for that period is the Rapid Eye Mount (REM) telescope [5]. It is a 60 cm diameter fast reacting telescope, placed at the ESO Chile Observatory. It consists of two instruments: REMIR that it is an infrared camera,

[5] http://www.rem.inaf.it/

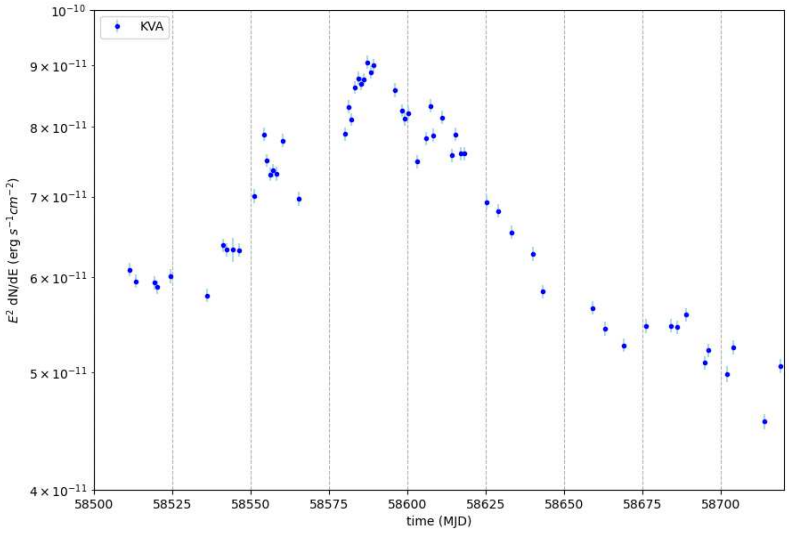

Figure 4.7: Optical spectral energy distribution of PG 1553+113 as a function of time. It is plotted from January 2019 up to September 2019. The peak during the flare is clearly visible. The single points can be converted and put in a broad band SED by substituing in the x axis the wavelength of the R filter.

and ROS2 an optical imager. In this work the observations of just the former instrument were considered with the following filters according to the 2MASS photometric system:

- J with $\nu = 2.6 \cdot 10^{14}\, Hz$;
- H with $\nu = 2.0 \cdot 10^{14}\, Hz$;
- K with $\nu = 1.5 \cdot 10^{14}\, Hz$.

The transparency, so the amount of light that can pass through the filter as a function of the wavelength, is plotted in Fig. 4.8.
The analysis was performed by Dr. Stefano Covino, also PI of the observations. The data were provided in terms of magnitudes, so they needed to be converted into flux units. In order to do so I created a python script that converted the magnitudes into fluxes in Jansky (Jy) units, using the formula:

$$F = 10^{0.4\cdot(\mathrm{zp_{band}}-\mathrm{mag})} \tag{4.1}$$

with F being the flux, mag the magnitude value that needs to be converted and $\mathrm{zp_{band}}$ being the zero point for each band. The error on the fluxes was retrieved using the error propagation formula, resulting in:

$$\sigma_F = 0.92 \cdot \sigma_{\mathrm{mag}} e^{0.92\cdot(\mathrm{zp_{band}}-\cdot\mathrm{mag})} \tag{4.2}$$

with σ_F and σ_{mag} being the errors on the flux and the magnitude. Then I converted both the values of the fluxes and their errors, from Jy to $\mathrm{erg \cdot cm^{-2}s^{-1}}$ using the following formula:

$$\mathrm{SED} = \mathrm{k} \cdot \nu_{band} \cdot \mathrm{F} \tag{4.3}$$

with SED being the value in correct units, k is a constant with a value of 10^{-20} in order to get the conversion of units, ν_{band} is the frequency of the band and F is the flux value. The same equation can be used in order to convert the errors of the flux in jansky in SED errors, by just substituing F with σ_F in the previous equation. After having performed these transformations the final IR SED was built for each day. The REM data were available

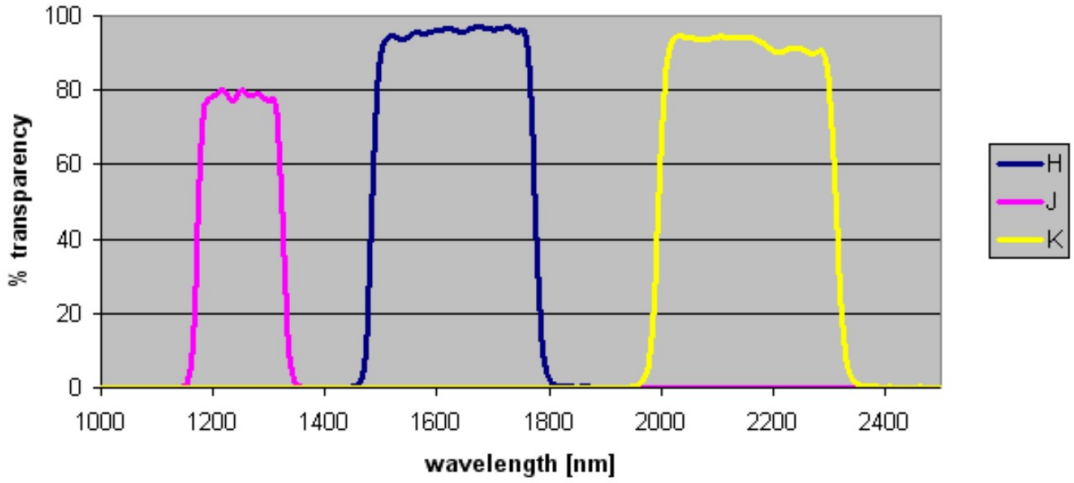

Figure 4.8: Transparencies of the H,J,K REM filters. Image from `http://www.rem.inaf.it/`

just for the April month in the following dates: 02-05-08-11-14-17-20. The averaging of the SED values, shown in Fig. 4.9 , has been performed on the data from the 8^{th} to the 14^{th} of April 2019.

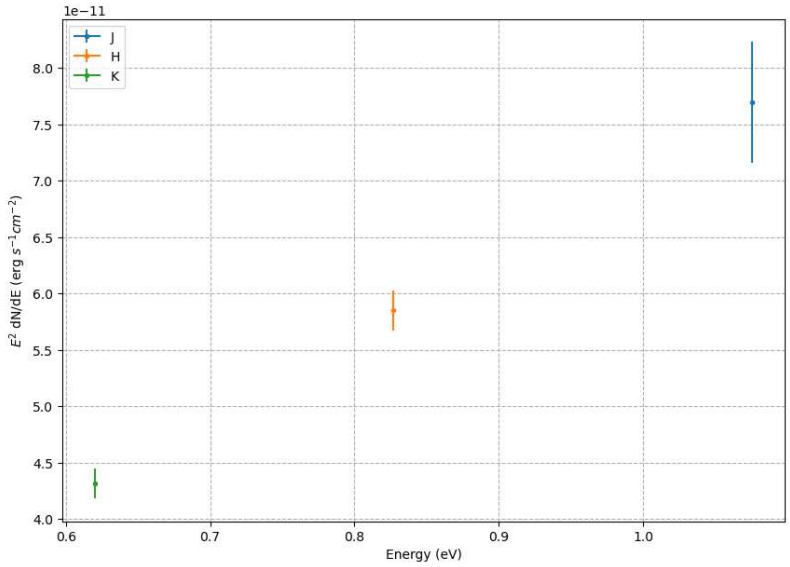

Figure 4.9: Average SED of PG 1553+113 in IR band computed using three different filters J,H and K. The averaging has been performed on the data collected on the $8^{th} - 11^{th} - 14^{th}$ of April 2019

4.6 Radio band

For the radio band the instrument that had observed the source in the period of intrest was the Owens Valley Radio Observatory (OVRO) [6]. Build in the 1960s with the purpose of detecting astrophysical neutrinos, it is a 40m in diameter telescope and has monitored over 5500 AGNs. The telescope performs radio measurements at a frequency of $\nu_{OVRO} = 1.5 \cdot 10^{10}\, Hz$. The lightcurve was obtained thanks to Dr. Elisa Prandini, that was already in possess of these data. After that, the conversion from Jy to ergcm^{-2}s^{-1} was performed using formula 4.1. Several observations have been performed on PG 1553+113:

[6] https://sites.astro.caltech.edu/ovroblazars/

- February 2019: 26;
- March 2019: 16-18-24-30;
- April 2019: 4-21-28;
- May 2019: 5-15-21-24-28;
- June 2019: 6-10-18-24;
- July 2019: 1-6-13-14;
- August 2019: 13-16;

Fig. 4.10 shows the spectra of PG 1553+113 as a function of the time. The April observations do not temporarly match that of the other bands, but, as it will be discussed later, it will not cause any problem.

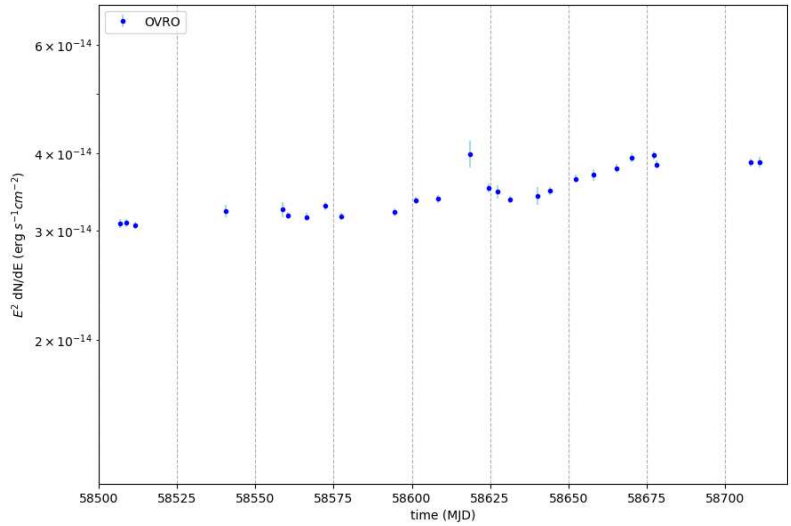

Figure 4.10: Lightcurve of PG 1553+113 in the radio band as a function of time. The data were collected by the OVRO telescope between February and August 2019.

4.7 MWL lightcurve

After the analysis of the individual wavelengths, it is important to superimpose the lightcurves at all energy bands in order to highlight ?? of the source properties. This plot is shown in Fig. 4.11. The data points are plotted from the 17^{th} of January 2019 up to the 25^{th} of August 2019. The energies shown in the plot are displayed in an increasing easy from top to bottom panel, with the first upper panel having OVRO lightcurve, while the last one is the MAGIC lighcruve above 150 GeV. All the data shown in the plot is daily binned, with th exception of *Fermi*, that instead is weekly binned. It is possible to see the clear daily variability of the source at almost all the energies, except for the HE range. The flaring event is clearly visible at all frequencies, except for *Fermi* and REM, the former likely due to the weekly binning of the flux points, for the latter this is due to the missing observations before and after the flare. In the radio band, as it is possible to see from the first panel, the increase in flux happened with a delay of a couple months compared to that at other wavelengths, in agreement with previous results by the *Fermi*/LAT collabration. Furthermore this plot shows the main difficulty in performing a strictly multiwavelength campaign, and is that of the simultaneity of the observations. From this problem the necessity of dividing the data into different periods, in order to produce SEDs that are

representative of the state. A drawback of this approach is the loss of interday variability information.

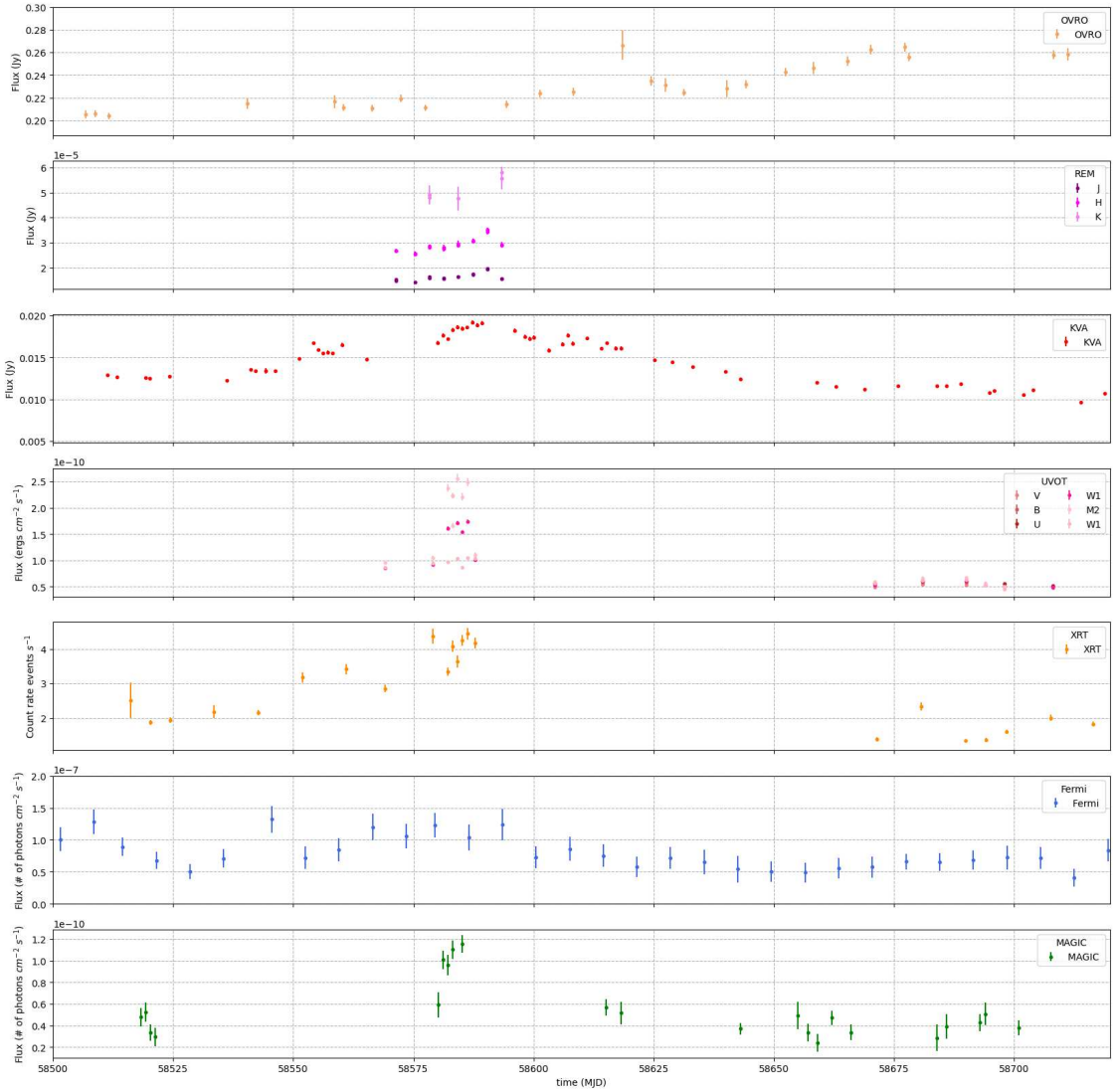

Figure 4.11: Multiwavelength lightcurve of PG1553+113. The energy measured by each instrument increases from top to bottom. The flaring episode is clearly visible at all wavelengths, except for *Fermi* due to its weekly binning.

Chapter 5

SED modelling and interpretation

The next step after the collection of the available multiwavelength data is the modelling and the interpretation of SED. First it is important to divide the dataset into subgroups depending on the period and the fluxes. For this reason and considering that I focused more on the MAGIC analysis, I divided the data into two periods:

- Flaring state: with flux $> 0.5 \cdot 10^{-10}$ $cm^{-2}s^{-1}$. In this category there are just the April 2019 data;
- Enhanced state: with $0.3 \cdot 10^{-10}$ and $0.5 \cdot 10^{-10}$ $cm^{-2}s^{-1}$. In this category there are the data from June to August;

The latter group is called "Enhanced" and not "low state", for the simple reason that its average flux is higher than the one during a low state, as can be seen in Fig. 5.1. The red dashed line shows the average flux between June and August 2019, the lighcurve instead covers a period from 2015 up to August 2019, allowing to check how low the VHE emission from PG1553+113 can get. This demonstrates that the period after the flaring episode is not a low state but is still an active time for the source. The May 2019 observations and those of the ST.03.12 (from MJD 58742 to MJD 58901) period are not included in this work because there were not multiwavelength data taken during those days, meaning that the modelling cannot be attempted.

After the separation of these two datasets, it was necessary to average the data at each band, in order to compute the SEDs for both the enhanced and the flaring state. For MAGIC data this was done directly using the standard analysis, so dividing the melibea files for those periods, and then generating the respective flute and then fold outputs accounting already for EBL absorption. Regarding *Fermi* instead, they were directly produced with the analysis. Lastly for the remaining bands, the weighted average on the data points was performed, so the formula used was:

$$E^2 \frac{dN}{dE}_{avg} = \frac{\sum_i \frac{F_i}{\sigma_i^2}}{\sum_i \frac{1}{\sigma_i^2}} \tag{5.1}$$

with F_i being the single SED point and σ_i its error.
The error on the weighted instead is computed using:

$$\sigma_w = \frac{1}{\sqrt{\sum_i \frac{1}{\sigma_i}}} \tag{5.2}$$

with the previous meanings.

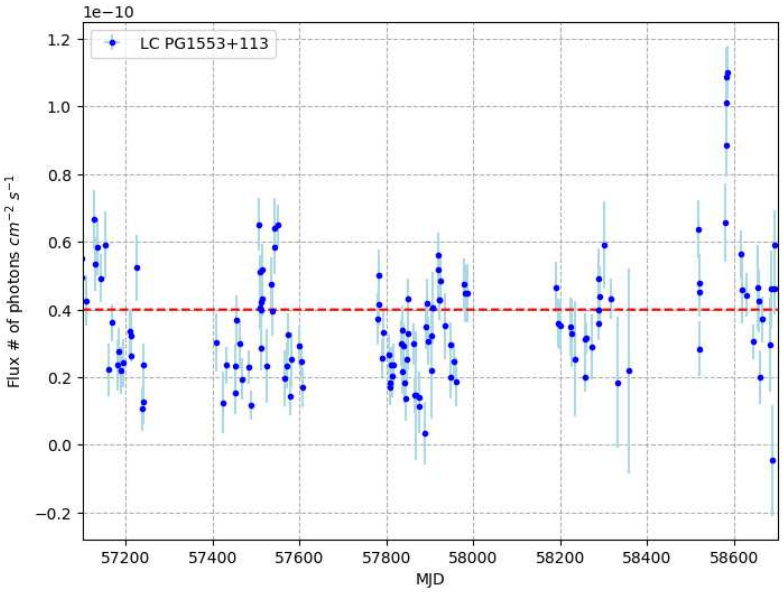

Figure 5.1: Multi year VHE lightcurve of PG1553+113 above 150 GeV, as measured with the MAGIC telescopes. The plot comprehends data from 2015 up to August 2019. It is possible to see three flaring episodes (from MJD 58578 up to MJD 58586) including the one discussed in this work. The dashed red line represents the average value of the flux during the June-August 2019 period, its value is $\sim 0.4 \cdot 10^{-10}\, cm^{-2} s^{-1}$

5.1 AGNpy

`Agnpy` ((Nigro et al., 2022)) is an open-source Python package with the purpose of modelling the SEDs of AGNs. It is built using other Python packages like astropy, Scipy and Numpy and uses data analysis tools from sherpa and gammapy. Agnpy has different modules that serve several purposes, first of all one that characterizes both thermal and non-thermal emitters, these modules are `agnpy.emission_regions` and `agnpy.targets`. The former describes the electron energy distribution (EED), as a function of the Lorentz factor γ' of the electrons and positrons that are accelerated by the source. The EED emitting the photons is considered to to be located in a spherical blob of plasma in the jet. The primed quantities are in the reference frame comoving with the blob. `agnpy.targets` instead is used to give a description of those parts, e.g. lines or thermal emitters, that are the target for either IC or $\gamma\gamma$ interactions. These targets are the following:

- Cosmic Microwave Background (CMB);
- a point source that emits in a monochromatic way and is located behind the jet;
- Shakuya & Sunayev accretion disk (Shakura and Sunyaev, 1973);
- broad line region that is modelled with an infinitesimally thin sphere that absorbs and then re-emits monochromatic photons;
- dusty torus that is modelled as a ring that absorbs and re-emits black body radiation at fixed T.

Furthermore other components can be taken into account while modelling the SED, for example the multiple black body emission in the optical/UV or the IR emission from the dusty torus.
Other modules instead have the purpose of describing the radiative processes of the AGN emission. The only limiting factor is that these modules can characterize just leptonic

processes, hadronic models are currently being developed. `agnpy.synchrotron` computes self-absorbed synchrotron spectra, assuming the electron distribution to be in a large scale chaotic B field. `agnpy.compton` is used to characterize the Inverse Compton with both synchrotron photons, so synchrotron-Self Compton model (SSC), or with an external photon field External Compton (EC). The former model considers the target photons as a uniform blob, while for the latter the electron distribution is boosted in the comoving frame of the target photon field and its energy distribution gets convolved with that of the radiation. The last module regarding the radiative processes is `agnpy.absorption`, it models the $\gamma\gamma$ absorption with emission lines and other thermal emitters. Furthermore it can compute even the EBL absorption with three different models: Dominiguez 2011, Franceschini 2008 (Franceschini et al., 2008) and Finke 2010 (Finke et al., 2010).

The last set of modules has the purpose of constraining the parameters of the electron energy distribution time evolution. This is done by the module `agnpy.constraints`, that applies bounds to the parameters in order for them to be self-consistent. This module uses three different timescale: cooling, acceleration and ballistic (or dynamical). The first one describes the cooling timescale of the electrons due to either synchrotron or IC in Thompson regime, this timescale is described by:

$$t'_{cool} = E' / \left(\frac{dE'}{dt'} \right)_{cool}, \quad \text{with} \left(\frac{dE'}{dt'} \right)_{cool} = \frac{4}{3} \sigma_T c u' \gamma'^2 \tag{5.3}$$

with σ_T being the Thompson cross section, u' is the magnetic energy density in case of synchrotron emission or that of the radiation field for IC. The acceleration timescale is defined as:

$$t'_{acc} = E' / \left(\frac{dE'}{dt'} \right)_{acc}, \quad \text{with} \left(\frac{dE'}{dt'} \right)_{cool} = \frac{E'}{R_L} \epsilon c \tag{5.4}$$

with E' being the electron energy, R_L the Larmor radius and ϵ the acceleration parameter. Lastly the ballistic timescale that is used in order to derive the escape time of the photons from the blob. It is defined as following:

$$t'_{bal} = \frac{R'_b}{c} \tag{5.5}$$

with R'_b being the radius of the blob. A schematics of the modules of `agnpy` is shown in Fig. 5.2

Regarding the fit of the SED, with `agnpy.fit` it is possible to choose two packages, the first one being `sherpa` and the other being `gammapy`. For this work the former has been used.

5.2 SED modelling

In order to perform the modelling of a source with `agnpy` is it first necessary to create a .ecsv file. This type of files are used to specify the SED units, in this case ergs/s/cm^2, and it is composed by several columns for the energy in eV, SED values, their errors and the instrument used for each measurement. The latter is written in the files because agnpy can compute the systematics of the individual instruments by adding a percentage of the value to the errorbars. This varies among instruments, for example MAGIC has an error on each SED point of 30%, *Fermi* of 10% and UVOT of 5%.

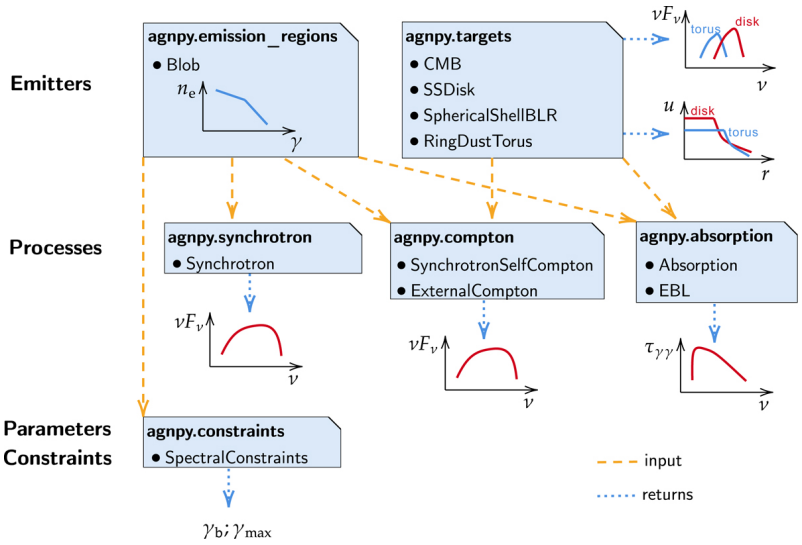

Figure 5.2: `agnpy` schematics. The plot shows the three different aims of the modules and their relationships

After the separation of the data into two different .ecsv files, one for the flaring state and the other for the enhanced state, we are finally ready to start modelling the SED emission. For BL Lacs, like PG 1533+113, the typical SED model is a SSC, with the synchrotron-Self Compton, so the synchrotron photons are scattered by the same electrons that produced them. The reason why for BL Lacs this is the common way of emitting high energy photons and not by the External Compton, this is due to the fact that this category of blazars doesn't have a particularly strong external photon field.

5.2.1 One-Zone SSC model

The first model that has been applied to both data sets is the so called one-zone SSC model. It is based on the hypothesis that there is just one population of electrons responsible for both synchrotron and SSC emission. The model that has been used to describe the electron energy distribution is that of a broken power law, due to the peak profile of the SED. `agnpy` takes as input several parameters, in order to perform a fit it is necessary to obtain some constrains on them, unfreezing just the necessary quantities. In this case the radius of the emitting region has been obtained by inputing the variability timescale (Eq. 21) that has been retrieved using X-ray measurements, its value has been set to 1 day. The redshift has been set to the value found in the Dorigo Jones paper of 2021, and freezed to a value of 0.433. Regarding instead the spectral indices p1 and p2, the former has been constrained using REM data, while the latter using *Fermi* data. The values of γ_{min}, γ_{max} and γ_b have been determined by the shape and width of the synchrotron hump. The Doppler factor δ_D instead is found using the positions of both peaks.
After having determined some constraining values for most of the parameters, it is possible to proceed with the fit of the broad band SED. The fit has been performed using the `sherpa` class Fit. It is a class that takes as input: the SED points, the energy range for the fit, instrumental systematics, the model, and then which method to use in order to fit the data points. In particular the minimization of χ^2 has been used optimizing through the Levenberg-Marquardt algorithm. Fig. 5.3 shows the fit of the broad band SED of the flaring state. It is possible to notice in this plot that the OVRO data point has been omitted, the reason behind this choice is that, the radio emission happens later in another independent zone. From a visual inspection, the fit describes in a good way the synchrotron part of the emission but clearly fails to describe the more energetic component, this is a problem

that will be addressed later. The result of the regression is shown in the second column of Tab. 5.1. The same procedure has been applied to the SED of the enhanced state. The data of this period instead misses, as previously discussed, IR observations. In order to fit the SED of the enhanced state, a softer value of p2 was needed, so from 3.3 during the flaring episode up to 3.45 during the lower state.

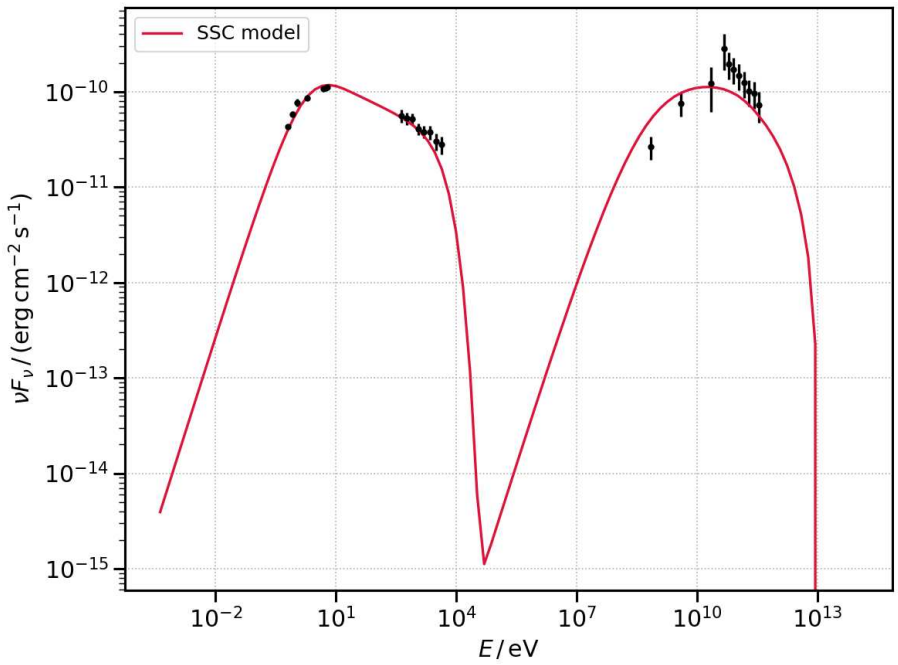

Figure 5.3: Fit of the broad band SED of PG 1553+113 flaring state. The data have been fitted using a one-zone synchrotron self compton model.

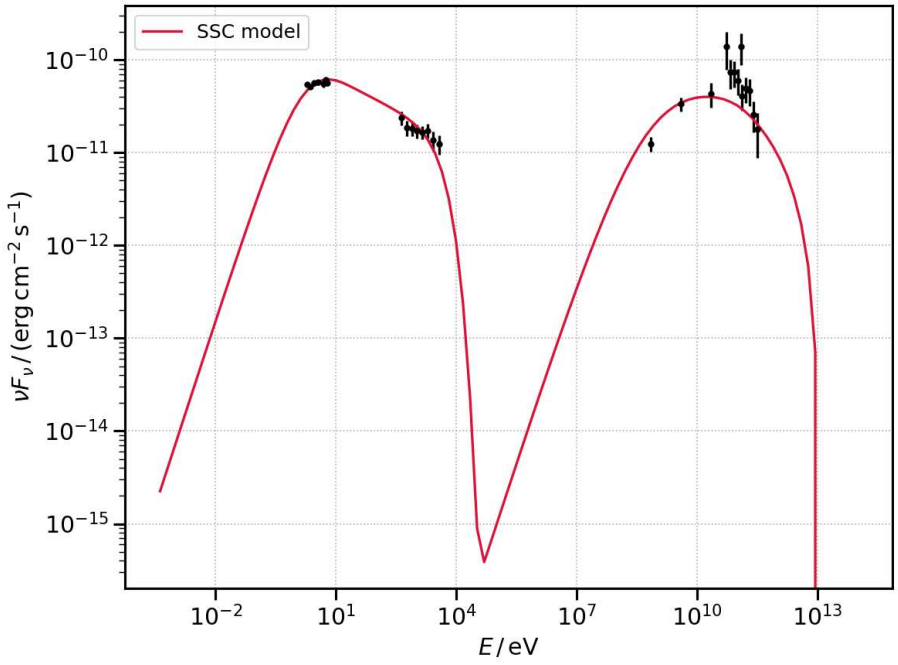

Figure 5.4: Fit of the broad band SED of PG 1553+113 enhanced state. The data have been fitted using a one-zone synchrotron self compton model.

Fig. 5.4 shows the fit obtained with the enhanced state data set, the result of this regression is displayed in the third column of Tab. 5.1. The main noticeable difference between

these two states is the height of the SED peak, for the flaring period it is of the order of $\sim 10^{-10}$ ergs/s/cm^2 while for the other one is about $\sim 6 \cdot 10^{-11}$ ergs/s/cm^2.

Other important differences are obtained by comparing the fit results for both states shown in Tab. 5.1. The three parameters that differ are: γ_b, B and k. The latter is the one with the most significant difference compared to the other two. This difference can indicate the fact that the phenomenon that is responsible for the flaring episode increased the magnetic field and electron number density, while lowering the γ_b. The possible explanation can be that of a shock wave, that compresses the blob making it more dense and increasing B, and, at the same time, increasing the Lorentz factor of lower energy electrons meaning a lower γ_b.

	parameter	flaring period	enhanced period	2012 flare
	z	0.433	0.433	0.4
	δ_D	60	60	40
	γ_{min}	8000	8000	3700
	γ_{max}	$5.2 \cdot 10^6$	$5.2 \cdot 10^6$	$8 \cdot 10^5$
	$log_{10}\gamma_b$	4.15 ± 0.03	4.27 ± 0.03	4.6
	p1	1.5	1.5	1.6
	p2	3.3	3.3	3.83
	t_{var}	1 day	1 day	0.8 days
	$log_{10}k$	$-5.53 \pm 0.07\, cm^{-3}$	$-6.00 \pm 0.07\, cm^{-3}$	$1.3\, cm^{-3}$
	$log_{10}B$	$-1.74 \pm 0.02\, G$	$-1.80 \pm 0.02\, G$	$-1.35\, G$

Table 5.1: Agnpy parameters of the fit of both flaring (2^{nd} column) and enhanced (3^{rd} column) state one zone SSC. The fourth column shows the results of the 2012 flare obtained by (Aleksić et al., 2015).The difference between the two states is in the γ_b, electron number density and magnetic field.

This model has some problems regarding some values like the Doppler factor of 60. It is a very high value, even compared to previous paper results (Aleksić et al., 2015) shown in the fourth column of Tab. 5.1. The parameters used for the modelling of the 2012 flare of PG 1553+113, seem to significantly differ from the ones found in my work, except for p1 . This disagreement is most likely due to the behaviour of this source, that changes the shape of the emission in timescale of years. This means that another model might be more correct. In the following, I propose a study of the correlation between bands, which can be very useful as an input for more sophisticated models.

5.2.2 Correlation studies

Correlation studies are a comparison between the fluxes from different wavebands. The conditions that are imposed on them are: to be simultaneous in a predefined time range, and unique. It can happen, depending on how many consecutive observations have been performed with an instrument, that multiple fluxes of one frequency (e.g. HE) are associated to the same one at another energy (e.g. X-rays). Thanks to the last condition this situation is avoided. These plots, performed for every energy range available in this work, except for IR and UV, due to small sampling problem, and radio data points, due to the fact that is not included in the modelling. In order to perform the correlations, I've created a python script that, taking as input two lightcurves at different energies, performs the conditions

described above with a simultaneity range of ±1 MJD. This condition is different in case of correlations with *Fermi* lightcurve, where I adopted a time range of ±1.5 MJD due to the fact that the *Fermi* flux is 3-days binned and the simultaneity range cannot be shorter than the time binning of the lightcurve. In order then to see if two energies are correlated or not, I've computed Spearman coefficients and the corresponding p-values. The reason for this choice is that it is more suited to test correlation between lightcurves than the Person coefficient. The Spearman test can take into account a non-linear relationship of the data, is less sensitive to outliers and is more efficient for monotonic relations compared to Pearson coefficient. Moreover, the same test was adopted in a recently work of the MAGIC collaboration focused on the characterization of the variability patterns in PG 1553+113 up to 2017.

	Band 1	Band 2	Spearman coefficient	p-value
	VHE	X-rays	0.90	0.03
	VHE	HE	0.49	0.052
	HE	X-rays	0.42	0.035
	VHE	R	0.79	0.0002
	X	R	0.94	4.4E-07
	HE	R	0.39	7.7E-19

Table 5.2: Correlation between different bands. The statistical tool to control the correlations is the Spearman coefficient (3^{rd} column). The p-value of the Spearman coefficient (last column) shows how the correlation is.

The results of the correlation studies are listed in Tab. 5.2, while Fig. 5.5 up to Fig. 5.10 are the plots relative to each correlation. The strongest correlations are between VHE with X-ray, X-ray with R-band and VHE with R, while HE vs the other bands does not show strong correlation. This problem could actually be due to the wide binning of *Fermi* data, making more difficult to find any correlation. In order to avoid such a hindrance, a solution could be that of taking multi-year lightcurves. So the only reliable correlation, as even shown by the p-value, is HE vs R, that contains lightcurves from several years.

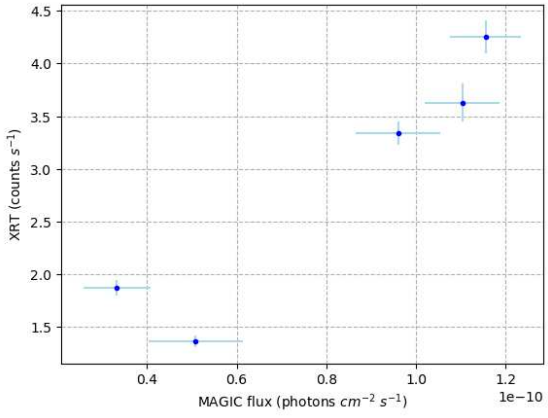

Figure 5.5: XRT flux vs MAGIC flux. The number of points is not large, as it was expected due to the sparse observations performed by both instruments. From the Spearman coefficient the correlation between these two bands is strong.

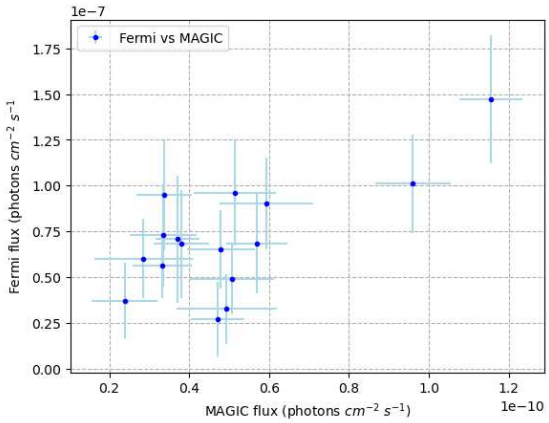

Figure 5.6: *Fermi* flux vs MAGIC flux. The *Fermi* lightcurve is 3-days binned. From the Spearman coefficient the correlation between these two bands is low.

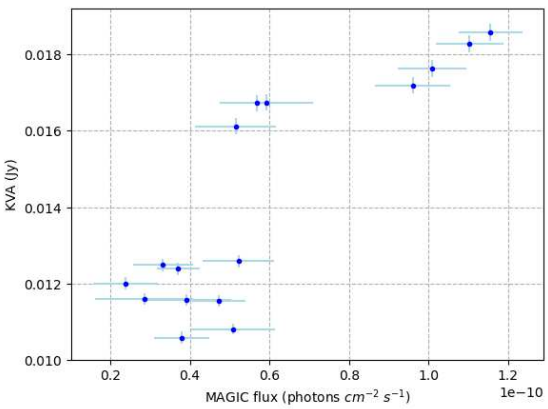

Figure 5.7: KVA flux vs MAGIC flux. From the Spearman coefficient the correlation between these two bands is strong.

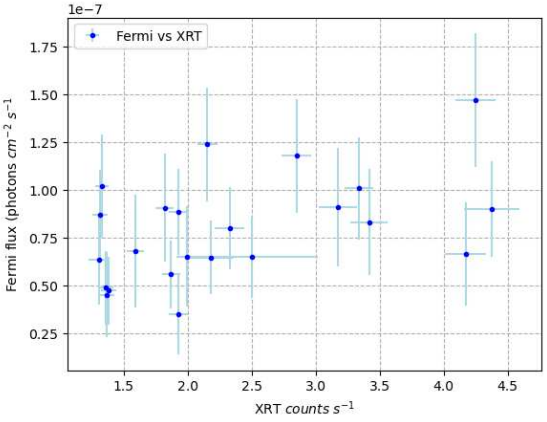

Figure 5.8: *Fermi* flux vs XRT flux. The *Fermi* lightcurve is 3-days binned. From the Spearman coefficient the correlation between these two bands is low.

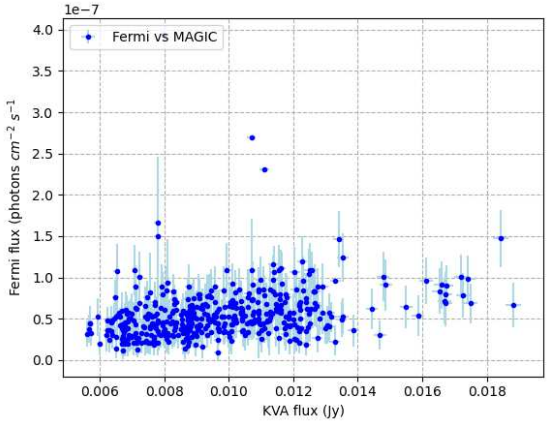

Figure 5.9: *Fermi* flux vs KVA flux. The *Fermi* lightcurve is 3-days binned. From the Spearman coefficient the correlation between these two bands is low.

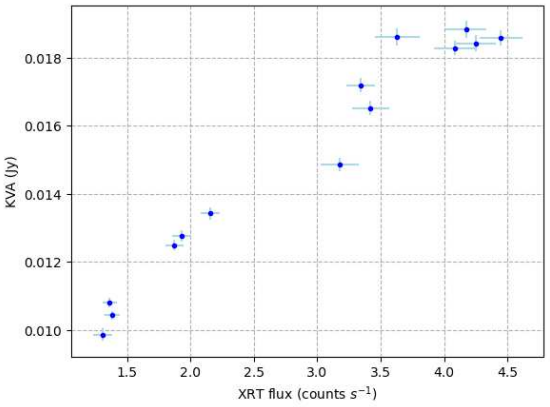

Figure 5.10: KVA flux vs XRT flux. From the Spearman coefficient the correlation between these two bands is very strong.

The presence of some bands not correlating implies that the one-zone SSC model might not be the correct one. The reason is that, in this type of emission, every band should correlate with each other, due to the fact that they are emitted by the same electron population. Then the model that will be discussed in the next section is that of a two-zone SSC emission.

5.2.3 Two-zone SSC model

The two-zone SSC model describes the SED of a source considering two independent electron populations responsible for different parts of the emission. For example there could be one zone responsible for both low energy and HE radiation, and another which emits in X-rays and VHE, from now on they will be noted respectively zone 1 and zone 2. With `agnpy` the way of modelling two zone SSC is similar to that for the one zone. First the datasets are divided for each electron population, then they are fitted and in the end they are summed together in order to obtain the final SED. The only issue with a two-zone SSC is that the number of parameters are doubled compared to the previous model. This means that while the fit can more easily describe the SED due to larger number of degrees of freedom, there will probably be a degeneracy on the obtained parameters. Furthermore, due to the

high number of parameters for the model, while summing the two zones, a correction of the parameters is needed in order to fit well the data. The separated fit of both electron populations during the flaring state are shown in Fig. 5.11 and Fig. 5.12 while the results of the fit are the first two columns of Tab. 5.3. The zone 1 has been modelled using a power-law electron energy distribution, while zone 2 using a broken power-law. The reason behind this difference is that the γ_{min} for the zone 2 needed to be high, but `agnpy` sets a maximum value of this parameter to be 10000. So in order to input a higher value it was necessary to use a broken power law model, with $\gamma_{min} = 10000$, spectral index p1 = 1, while γ_b represents the actual initial value of the Lorentz factor distribution, simulating a power-law spectral shape. From the fit of zone 1 it is possible to see that the fit does not necessary need to describe perfectly the emission, the zone 1 model alone does not describe the HE. The important characteristic is that the sum of the emission from the two zones follows the data points.

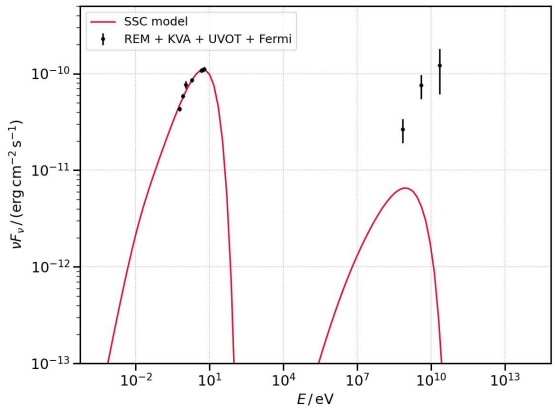

Figure 5.11: Fit of the SED of zone 1 using a power law spectral shape for the electron energy distribution. The data shown were taken during the flaring state.

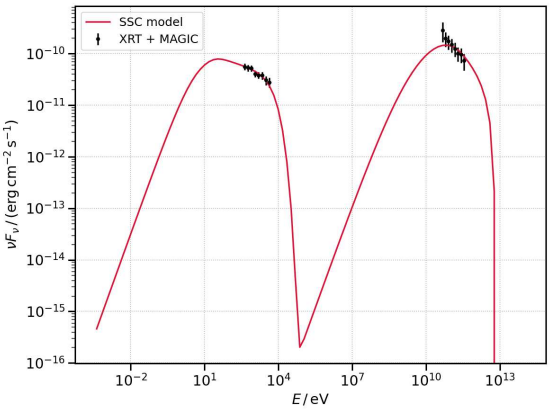

Figure 5.12: Fit of the SED ofzone 2 using a broken power law spectral shape for the electron energy distribution. The data shown were taken during the flaring state.

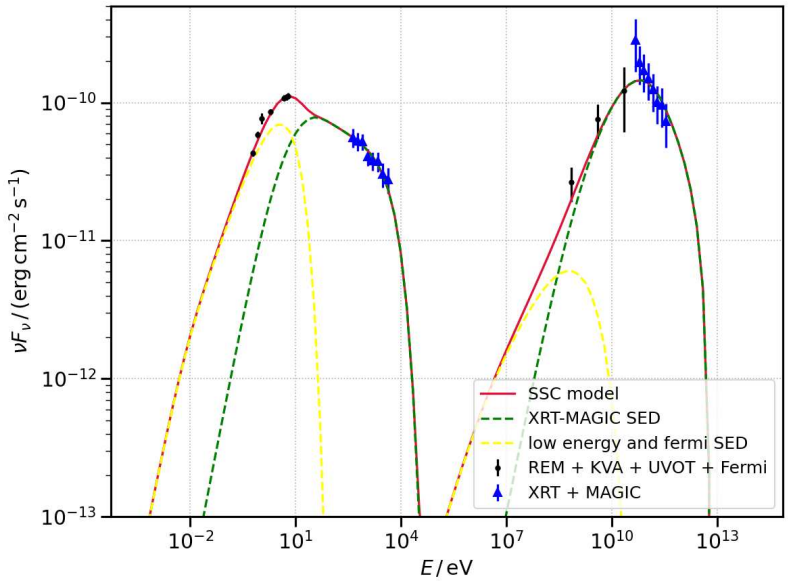

Figure 5.13: Total SED of the flaring state of PG 1553+113. The red full line is the sum of the fit of zone 1 (yellow dashed line) and of zone 2 (green dashed line).

The summed SED describing the broad band emission during the flaring episode is shown

in Fig. 5.13. It is possible to see that, in this model, the main component at all energies, except for the optical/IR part is the one emitted by zone 2 (green dashed line). The zone 1 emission instead is mostly in the optical/IR part with negligible contributions from X-rays up to VHE, with a slight increase at the low part of the *Fermi* energy.
Regarding instead the enhanced state SED, the fit has been performed trying to keep the fixed parameters as close as possible to the ones of the flaring state. In Fig. 5.14 and Fig. 5.15 the fit of zone 1 and zone 2 is shown. The fit results instead are shown in the fourth and fifth columns of Tab. 5.3. The same power law and broken power law model has been used to describe both zones, the only difference lies in the zone 2 p2 spectral index, that from 3.3 has been increased up to 3.5 while for zone 1 the difference is in the value of k and B that has been tuned just after the sum of the zone 1 and 2 SED.

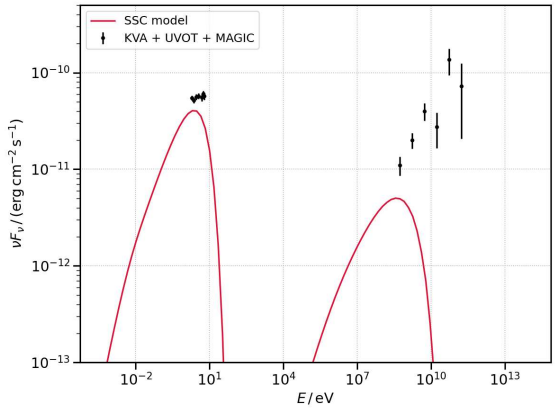

Figure 5.14: Fit of the SED of zone 1 using a power law spectral shape for the electron energy distribution. The data shown was taken during the enhanced state.

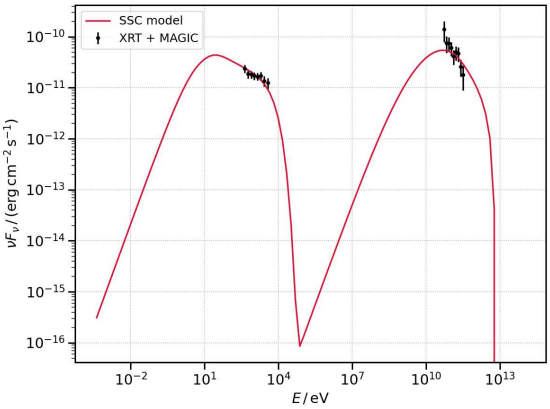

Figure 5.15: Fit of the SED of zone 2 using a broken power law spectral shape for the electron energy distribution. The data shown was taken during the enhanced state.

As it is possible to see from Tab. 5.3 there's a change in parameters from zone 1 and 2 between flaring and enhanced state. In particular this difference rises when considering the electron number density and magnetic field for both zones during the two different states. Furthermore there is a difference in spectral index regarding just zone 2. Another important difference between the two zones, that has been kept for both states, is the variability timescale. For zone 1 is of 3 days, while for zone 2 is of just 1. The reason for that is due to the fact that *Fermi* data has 3 days binning so this is the minimum t_{var} possible for zone 1, while from XRT data it was possible to say that the second zone has a variability of 1 day. This difference means that the emitting regions have different sizes, with zone 1 being bigger than zone 2.
The two-zone SSC model, even though it describes the SED in a very good way, still does not explain part of the correlation studies results. In particular there is the problem of the non correlation of the *Fermi* flux with the other bands. In a typical two-zone SSC HE and optical correlate very well, because the optical photons are those that will scatter and produce HE radiation. But this correlation hs been found to be weaker than expected. Furthermore this model has the problem of the increase, from enhanced to flaring state, of both zones. While in a typical two-zone model the flaring component is just one of the two zones. It is important to notice that this work is performed on data taken in a very narrow time range, just one year. The properties of this source seem to change in different periods. An example can be taken from the behavior described in (Middei et al., 2023). In this paper the X-ray polarization of PG 1553+113 during 2023 has been measured, finding it to be stronger than that in the optical. This phenomenon suggests a low level of correlation between X-rays and optical, but it is in contrast with what found in previous papers and in

Parameters	Flaring state		Enhanced state	
	zone 1	**zone 2**	**zone 1**	**zone 2**
z	0.433	0.433	0.433	0.433
δ_D	35	35	35	35
γ_{min}	500	1×10^4	500	1×10^5
γ_{max}	18 000	5.2×10^6	18 000	5.2×10^6
γ_b		3×10^4		3×10^4
p1	1.45	1	1.45	1
p2		3.3		3.5
t_{var} (days)	3	1	3	1
$log_{10}k\,(cm^{-3})$	−0.4	−5.79(4)	−0.24	−5.94(5)
$log_{10}B$ (G)	−1.2	−1.35(2)	−1.38	−1.39(3)

Table 5.3: Fit parameters of flaring and enhanced state of the two zones. The differences are on values of the magnetic field, electron number density and p2.

this work. So the behavior of this source is particularly complex to model and it would require work that goes beyond the purposes of this project.

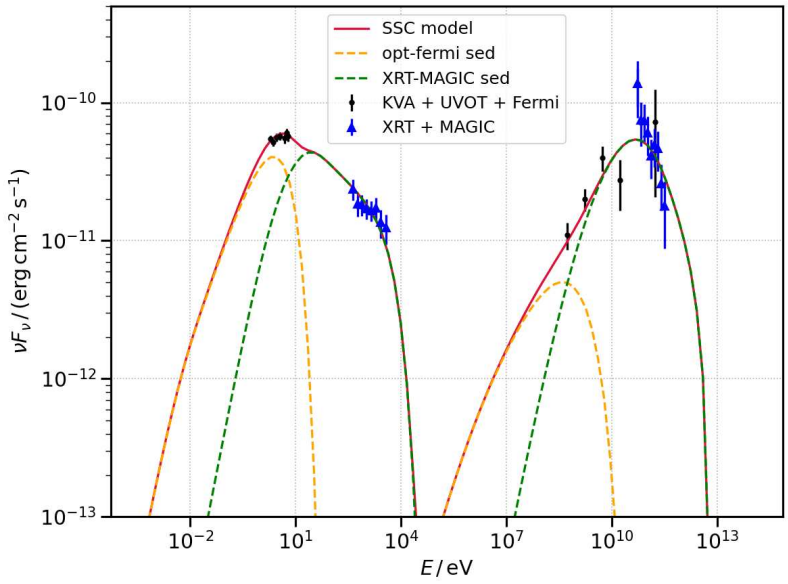

Figure 5.16: Total SED of the enhanced state of PG 1553+113. The red full line is the sum of the fit of zone 1 (orange dashed line) and of zone 2 (green dashed line).

5.2.4 Wobbling jet

Another hypothesis that has been tested is that the flaring episode could be due to a wobbling jet. It would mean that the increase in the flux could be due to a smaller angle of the jet compared to our line of sight, meaning a higher value of the Doppler factor. In order to test this hypothesis I froze the parameters obtained for the enhanced state, then I used them for electron energy distributions of the two zones during the flaring episode, performed a separate fit just of the Doppler factor and then summed the two SEDs. The

fit of zone 1 and 2 is shown in Fig. 5.17 and Fig. 5.18, while the summed SED is displayed in Fig. 5.19. The change in Doppler factor is different for the two zones, regarding zone 1 it increases from 35 to 37, while for zone 2 from 35 up to 39.7 ± 0.03. While this model fits very well the data, the its main problem is due to optical polarization measurements. As discussed in (Abe H., 2023), the hypothesis of a wobbling jet does not describe the distribution of polarization in the optical band.

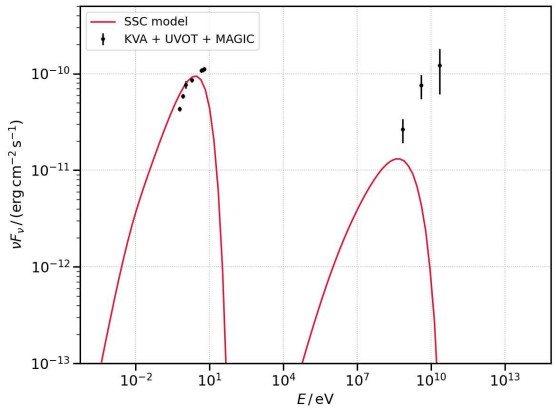

Figure 5.17: Fit of the SED of zone 1. The only parameter that is fitted is the Doppler factor. The data shown were taken during the flaring state.

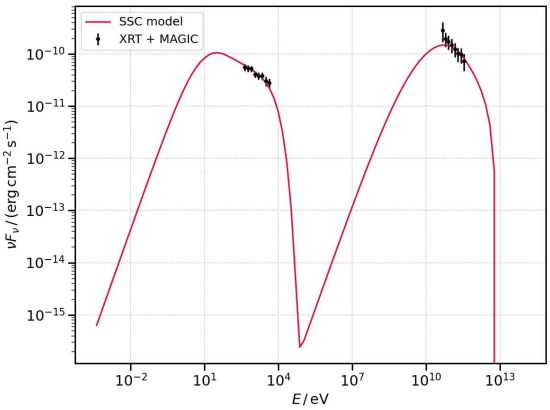

Figure 5.18: Fit of the SED of zone 2. The only parameter that is fitted is the Doppler factor. The data shown were taken during the flaring state.

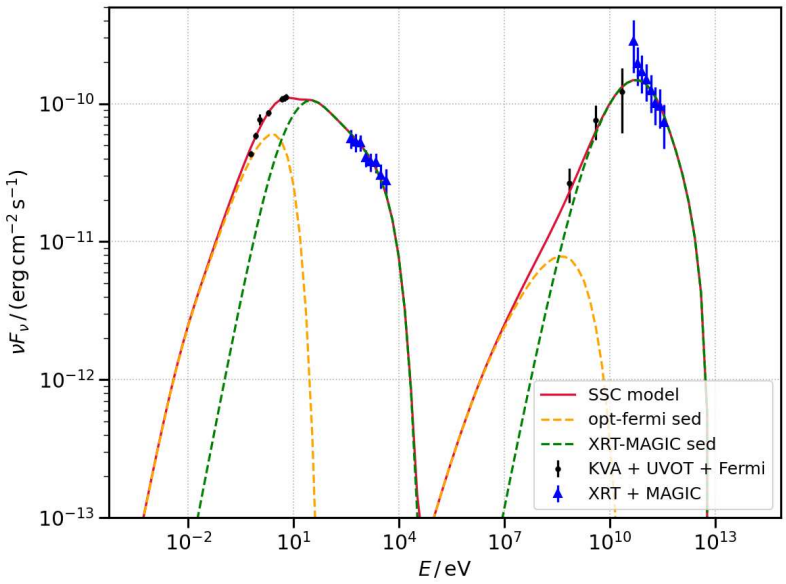

Figure 5.19: Total SED of the flaring state of PG 1553+113. The red full line is the sum of the fit of zone 1 (orange dashed line) and of zone 2 (green dashed line).

Chapter 6

Analysis of 2023 data of PG 1553+113

During March and April 2023, I had the chance of performing the flare advocate duty, meaning that I was in charge of quick-look analysis of the data from extragalactic sources showing a promising results in the real-time analysis. It consists of creating a Random Forest for that period, and, in case of a fast target of opportunity (fast ToO), doing the fast analysis of the data. This is done in order to check the significance of the signal and the flux of the source. In the very same period, PG 1553+113 entered its periodic flaring activity. So I did the analysis of the data taken in the ST.03.18 period. The time spanned by this period is from the 10^{th} of June 2022 up to the 31^{st} of August 2022, but since, at the time, the newest MC production was not available I used the MC from this period to analyze 2023 data. As it will be seen in the next sections, the MCs still represents quite well the system, even though they are not fully representing the performances of the current period. Several observations were performed in this temporal range, namely:

The data selection was applied with the following criteria:

- Cloudiness < 0.4;
- M2 DC < 2200 μA;
- L3 rates from 150*A up to 400*A, with A being $\cos(\mathrm{Zd})^{-0.35}$, a factor that takes into account the zenith angle distribution.

The Transmission cut was not applied due to a malfunctioning of the LIDAR, making its measurements not reliable. Then I have retrieved the MC simulations from the PIC servers. The ones chosen by me were of the wobble ring mmmcs699 and mmcs6500 type with zenith angles ranging from 5° up to 70°. The reason for the choice of this peculiar zenith range is that the RF was created in order to perform a fast analysis. So it needed to cover the widest range possible.
The MC simulations were retrieved already in the superstar format, for a total of 16 files, divided into 8 for the training and 8 files for the test. Tab. 6.2 shows how the files were split, with 1 and 2 having the same notation as explained in chapter 3.

Then the OFF data selection was performed, the following sources were chosen: PSRJ1402+13, GRB 220617A, 4FGL J1723.5-, OP 313, IC 20220624A, BL Lac, GRB 220706A, PKS 1749+096, Off2-GC, 1ES 0229+200, Galactic Cent, B3 2247+381. The total amount of observation time before quality cuts were applied is of 45.3 hrs, after the cuts were performed is reduced to 24.7 hrs. The RF was produced using the program coach with standard settings.

6.1 2023 Crab check

For the Crab check of the RF I chose the observations performed on the 14^{th} of March 2023. I chose this day to control how much of a difference, using a RF for the ST.03.18 period would make on data of another period. The total amount of time for this observation was of $\sim$ 1 hour. The plots showing the significance, the θ^2 plot and the skymap, are shown in Fig. 6.1 and Fig. 6.2.

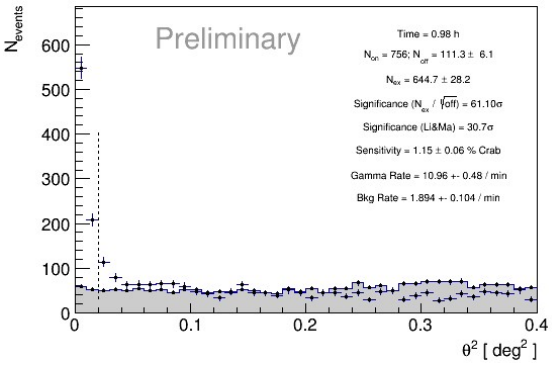

Figure 6.1: LE θ^2 plot of the Crab Nebula.

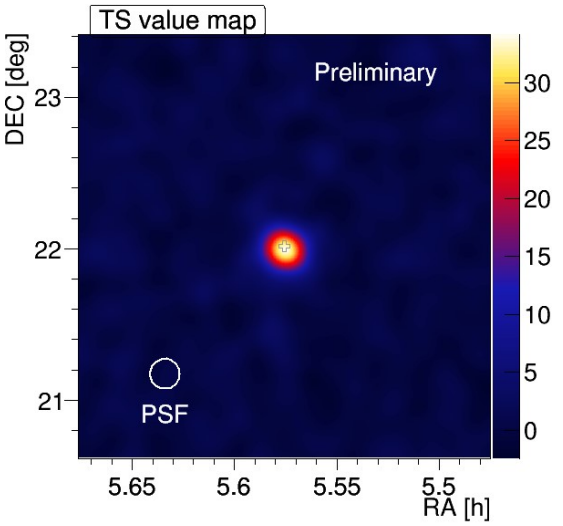

Figure 6.2: LE skymap of the Crab Nebula.

The significance shown in the θ^2 is consistent with what expected by Crab observations taking into account the observation time.
Then both SED and lightcurve were produced using flute, and are shown in Fig. 6.3 and Fig. 6.4. As it is possible to notice from the SED, the data follows nicely the expected trend, with only a slight mismatch at TeV energies, but it is normal considering the MC problem previously explained. The lightcurve instead is as expected, so this RF can be used even though the MC are not of the same period.

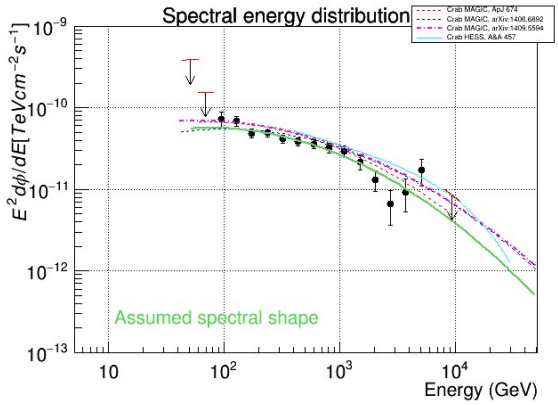

Figure 6.3: VHE SED of the Crab nebula produced with flute. The emission has been modelled using a Log Parabola function.

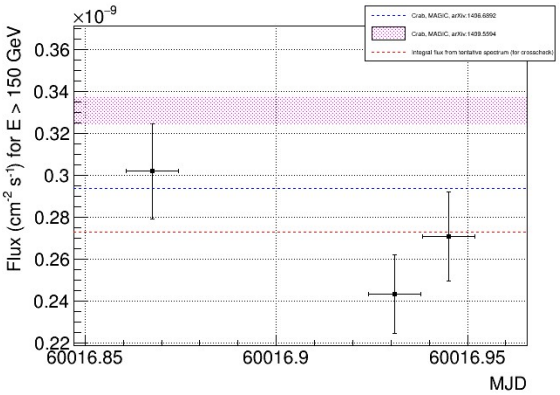

Figure 6.4: Run-wise lightcurve of the Crab nebula produced with flute. The shown day is the 14^{th} of March 2023.

6.2 PG 1553+113 2023 high level analysis

In this section, I report the results of the high-level analysis of PG 1553+113 data. Fig. 6.5 shows the θ^2 plots for all the stacked observations.

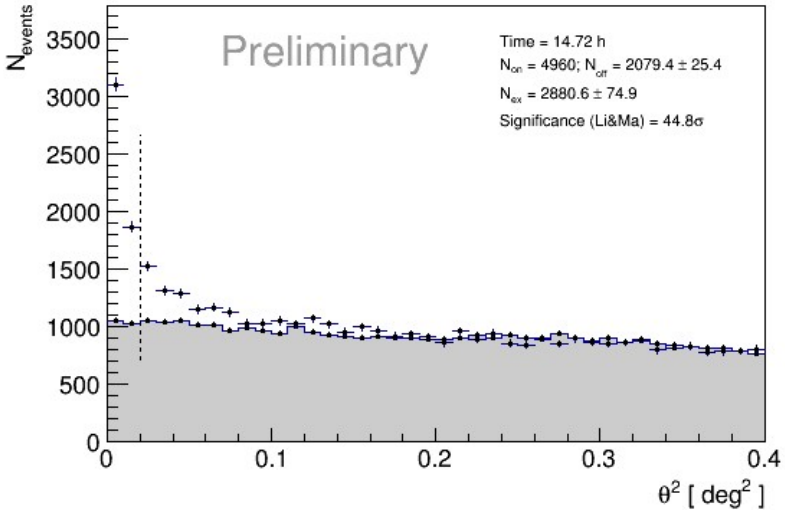

Figure 6.5: LE θ^2 plot of PG 1553+113.

The significance of the observation is quite high, this is due to the fact that in May 2023 the source was in flaring state. The only problem, as it will be possible to see in the lightcurve, is that just two days of the observations are in flaring state. The reason for not taking more data during this period is that during those days there was bad weather and there were some hardware problems.
Then, as displayed in Fig. 6.6, the skymap was produced. After the skymap, the next step was the lc and SED production using flute. The data were modelled with a power law spectral shape, with a spectral index of 3. Fig. 6.7 and Fig. 6.8 show respectively the SED and lightcurve of PG 1553+113. The cross check of the data is currently ongoing by Alberto Sciaccalunga.

The SED produced by flute shows both the values of the observed (filled) and EBL corrected values (open markers). In the lightcurve above 150 GeV it is possible to see the flaring event of May 2023. The previous data points show that this episode actually started in April and continued to grow until May. Then due to both bad weather and hardware problems, there are no further observations.
As a final step of the analysis I performed the unfolding procedure with fold on the stacked data. Fig. 6.9 and Fig. 6.10 display respectively the unfolded SED and the residuals of the powerlaw fit performed on the data points. The results of the fit are shown in Tab. 6.3. As it was previously done, the SED points have been deabsorbed using a redshift of z=0.433 and the Dominiguez 2011 EBL model.

Lastly it is of great relevance to highlight that the spectral shape is compatible between the 2023 flaring state and that of 2019, instead the fluxes during May 2023 reach higher values compared to those of April 2019 but are still compatible within the errorbars.

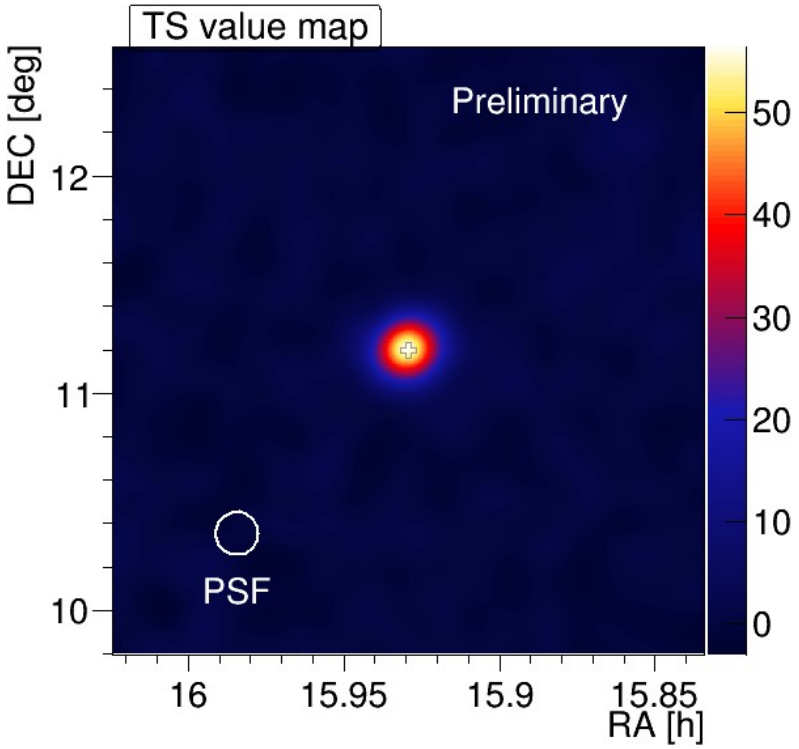

Figure 6.6: LE skymap of PG 1553+113.

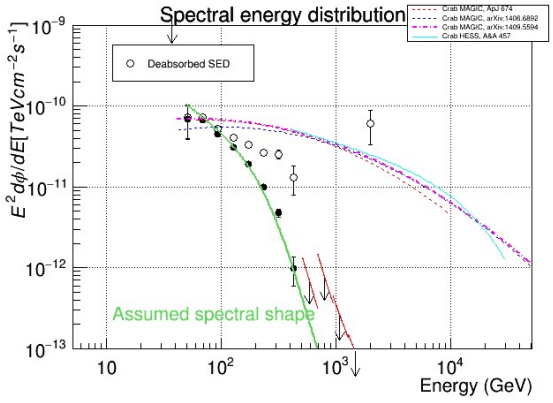

Figure 6.7: VHE SED of PG 1553+113 produced with flute. The emission has been modelled using a powerlaw function.

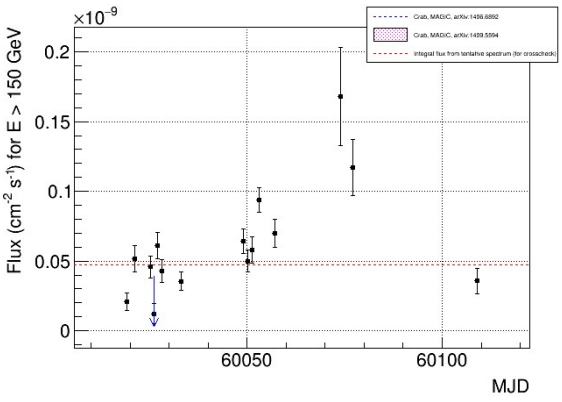

Figure 6.8: Night-wise lightcurve of PG 1553+113 produced with flute. The flaring episode that happened in May is clearly visible.

date	Zenith range (deg)	Observation time (hrs)
10/06/2022	20° - 40°	~ 1.2
18/06/2022	20° - 25°	~ 1
18/07/2022	30° - 45°	~ 1
03/08/2022	25° - 35°	~ 1
23/08/2022	35° - 45°	~ 1
29/08/2022	40° - 45°	~ 0.4
21/01/2023	35° - 50°	~ 1
27/01/2023	25° - 35°	~ 1
25/02/2023	40° - 60°	~ 1.2
14/03/2023	35° - 45°	~ 0.9
16/03/2023	20° - 25°	~ 1.0
18/03/2023	25° - 40°	~ 1.2
22/03/2023	20° - 30°	~ 1.4
23/03/2023	15° - 25°	~ 1
24/03/2023	25° - 40°	~ 1
25/03/2023	15° - 25°	~ 1.1
30/03/2023	25° - 35°	~ 1.2
15/04/2023	15° - 20°	~ 1.5
16/04/2023	20° - 35°	~ 1.6
17/04/2023	20° - 35°	~ 1.1
19/04/2023	20° - 30°	~ 1.4
23/04/2023	20° - 30°	~ 1.1
10/05/2023	20° - 20°	~ 1.7
13/05/2023	20° - 35°	~ 1.3
14/06/2023	20° - 25°	~ 1

Table 6.1: Most recent observations of PG 1553+113 (MAGIC observation period ST.03.18 and 2023 data). The second column shows the zenith angle distribution while the third shows the time of the observation.

mmcs	Zenith range (deg)	train	test
699	5° - 35°	1	2
6500	5° - 35°	1	2
699	35° - 50°	2	1
6500	35° - 50°	2	1
699	50° - 62°	1	2
6500	50° - 62°	1	2
699	50° - 62°	1	2
6500	50° - 62°	1	2

Table 6.2: Distribution of the MCs between test and train. The label 1 and 2 is the same as the one done at the PIC.

$f_0 \cdot 10^{-9}$	p1	Normalization energy (GeV)	χ^2	dof	reduced χ^2
2.17 ± 0.06	2.73 ± 0.07	137.13	19.6	17	1.15

Table 6.3: Fit results from fold on the data of the ST.03.18 period and 2023.

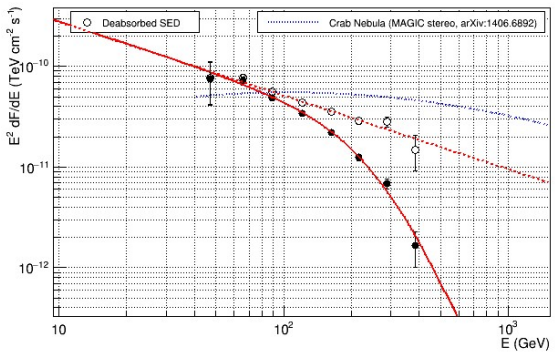

Figure 6.9: VHE SED of PG 1553+113 produced with fold. The fit has been performed using a powerlaw function.

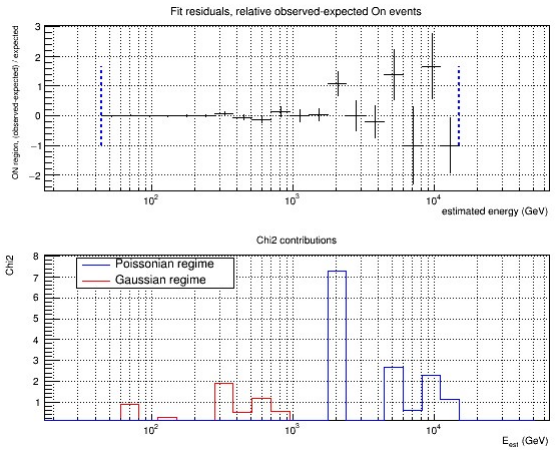

Figure 6.10: Residuals of the fit of PG 1553+113 spectrum performed by fold.

Conclusions

PG 1553+113 is a BL Lac located at z=0.433 in the constellation of Serpens. Its main characteristic, apart from the typical blazar variability, is a periodicity of 2.2 years in the *Fermi* HE gamma-ray energy band with a significance of 3σ. In this work first the analysis MAGIC data of this source has been performed with the purpose of characterzing its flux and variability in the VHE gamma-ray band. The analyzed data comes from two different analysis periods, ST.03.12 and ST.03.11, corresponding to the years 2020 and 2019. A flaring episode happened during the latter. Interestingly, a hint of intra-nigh variability was found during the flaring state which deserve further studies.
To properly characterize the simoultaneous broad-band emission from PG 1553+113, multiwavelength data were collected, obtaining: radio, infrared, optical, ultraviolet, X-ray, HE and VHE data. The dataset was then divided into two states, flaring and enhanced, according to the integral flux measured in the VHE band. This was done in order to distinguish the different behaviour of the source with the final aim of distinguishing the physical properties of the emitting region during different source states. I proceeded with modelling the broad band SED of PG 1553+113 using a one-zone synchrotron self Compton model. This model consist of having just one population of electrons responsible for the overall emission, with synchrotron electrons scattering the photons that they emitted up to the highest energies. I would say: The SSC model applied to to the two states can well reproduce the low energy synchrotron peak and only marginally reproduce the highest energies. Moreover, both the physical parameters resulting from the fit and the intra-band correlation study performed on the data, reveal that this model fails in describing all the properties of the emission.
I therefore attempted a two-zone model, in this case instead of having one zone emitting the broad band radiation there are two, that I called zone 1 and 2, with the former being responsible for the low energy and *Fermi* radiation while the second zone is responsible for X-rays and VHE γ rays. This model fits the data better than the previous one but still does not explain why *Fermi* data does not correlate with optical, X and VHE. The modelling of this source is very complex, this is due not only to the peculiar shape of the emission, the synchrotron peak is especially broad and the IC one is narrow, but even due to the fact that the behaviour of PG 1553+113 changes over time, as also supported by other works, e.g. a very recent paper from the IXPE collaboration.
This work will be continued by myself in the next years, with an extended dataset. Furthermore, new instruments, like the LST telescopes prototypes of the future CTA, will be able to observe the source at lower energies, enabling us to perform more precise measurements and provide more data for the modelling.

Appendix

date	Zenith range (deg)	Observation time (hrs)
04/02/2019	25° - 40°	~ 1
05/02/2019	25° - 35°	~ 0.7
06/02/2019	25° - 35°	~ 0.8
07/02/2019	25° - 40°	~ 1
07/04/2019	15° - 20°	~ 0.5
08/04/2019	20° - 35°	~ 1.2
09/04/2019	15° - 20°	~ 1
10/04/2019	25° - 35°	~ 1
12/04/2019	15° - 30°	~ 2
12/05/2019	15° - 20°	~ 1.1
15/05/2019	35° - 50°	~ 1
09/06/2019	20° - 45°	~ 2
21/06/2019	15° - 20°	~ 0.5
23/06/2019	25° - 40°	~ 1.2
25/06/2019	35° - 55°	~ 0.8
28/06/2019	25° - 45°	~ 1.5
02/07/2019	30° - 40°	~ 1
20/07/2019	20° - 25°	~ 0.4
22/07/2019	35° - 50°	~ 0.5
29/07/2019	20° - 30°	~ 1.5
30/07/2019	35° - 50°	~ 1
06/08/2019	20° - 35°	~ 1.3

Table 6.4: Dates of PG 1553+113 data chosen for the ST.03.11 period

date	Zenith range (deg)	Observation time (hrs)
08/12/2018	35° - 55°	~ 2.8
09/12/2018	35° - 55°	~ 1.6
28/12/2018	5° - 15°	~ 1
01/01/2019	20° - 40°	~ 5
03/01/2019	35° - 45°	~ 0.7
04/01/2019	5° - 45°	~ 4.6
05/01/2019	18° - 31°	~ 0.7
06/01/2019	17° - 24°	~ 0.5
16/01/2019	10° - 30°	~ 1.4
01/03/2019	50° - 60°	~ 1
23/04/2019	55° - 60°	~ 0.9
24/04/2019	55° - 60°	~ 0.5
25/04/2019	50° - 60°	~ 0.4

Table 6.5: Dates of Crab3 data chosen for the ST.03.11 period

Bibliography

Aartsen, M., Ackermann, M., and Jenni Adams, e. a. (2018). Neutrino emission from the direction of the blazar TXS 0506056 prior to the IceCube-170922a alert. *Science*, 361(6398):147–151.

Aartsen, M. G., Ackermann, M., and et. al, J. A. (2019). Neutrino astronomy with the next generation icecube neutrino observatory.

Abdollahi, S., Acero, F., and et al., L. B. (2022). Incremental fermi large area telescope fourth source catalog. *The Astrophysical Journal Supplement Series*, 260(2):53.

Abe H., e. a. (2023). The variability patterns of the tev blazar pg 1553+113 from a decade of magic and multi-band observations. Unpublished proposal.

Abeysekara, A. U., Albert, A., and et al., R. A. (2017). The 2hwc HAWC observatory gamma-ray catalog. *The Astrophysical Journal*, 843(1):40.

Abreu, P., Aglietta, M., Albury, J. M., and et al., I. A. (2022). Arrival directions of cosmic rays above 32 eev from phase one of the pierre auger observatory. *The Astrophysical Journal*, 935(2):170.

Ackermann, M., Ajello, M., and A. Albert, e. a. (2015). MULTIWAVELENGTH EVIDENCE FOR QUASI-PERIODIC MODULATION IN THE GAMMA-RAY BLAZAR PG 1553113. *The Astrophysical Journal*, 813(2):L41.

Aharonian, F. (2000). TeV gamma rays from BL lac objects due to synchrotron radiation of extremely high energy protons. *New Astronomy*, 5(7):377–395.

Aharonian, F., Akhperjanian, A. G., Bazer-Bachi, A. R., Beilicke, M., Benbow, W., Berge, D., and Bernlöhr, K., e. a. (2006). Evidence for VHE γ-ray emission from the distant BL Lac PG 1553+113. , 448(2):L19–L23.

Albert, J., Aliu, E., and et al., H. A. (2006). Detection of very high energy radiation from the BL lacertae object PG 1553113 with the MAGIC telescope. *The Astrophysical Journal*, 654(2):L119–L122.

Aleksić, J., Ansoldi, S., Antonelli, L., Antoranz, P., Babic, A., Bangale, P., Barceló, M., and et al., J. B. (2016). The major upgrade of the MAGIC telescopes, part i: The hardware improvements and the commissioning of the system. *Astroparticle Physics*, 72:61–75.

Aleksić, J., Ansoldi, S., and Antonelli, L. A. e. a. (2015). Probing the very high energy γ-ray spectral curvature in the blazar PG 1553+113 with the MAGIC telescopes. , 450(4):4399–4410.

Auger, P., Ehrenfest, P., Maze, R., Daudin, J., and Fréon, R. A. (1939). Extensive cosmic-ray showers. *Rev. Mod. Phys.*, 11:288–291.

Begelman, M. C., Blandford, R. D., and Rees, M. J. (1980). Massive black hole binaries in active galactic nuclei. , 287(5780):307–309.

Biland, A., Garczarczyk, M., Anderhub, H., Danielyan, V., Hakobyan, D., Lorenz, E., and Mirzoyan, R. (2007). The active mirror control of the magic telescope. *Proc. 30th Int. Cosmic Ray Conf.Vol. 3 (OG Part 2), 1353-1356 (2008).*

Bonnoli, G., Ghisellini, G., Foschini, L., Tavecchio, F., and Ghirlanda, G. (2010). The -ray brightest days of the blazar 3C 454.3. *Monthly Notices of the Royal Astronomical Society*, 410(1):368–380.

Broadhurst, T., Chen, C., Liu, T., and Zheng, K.-F. (2023). Binary supermassive black holes orbiting dark matter solitons: From the dual agn in ugc4211 to nanohertz gravitational waves.

Cao, Z., Aharonian, F. A., An, Q., and et al. (2021). Ultrahigh-energy photons up to 1.4 petaelectronvolts from 12 -ray galactic sources. *Nature*, 594(7861):33–36.

Cao, Z., della Volpe, D., Liu, S., Editors, :, Bi, X., Chen, Y., and et al., B. D. P. (2022). The large high altitude air shower observatory (lhaaso) science book (2021 edition).

Cooray, A. (2016). Extragalactic background light: Measurements and applications.

Cowan, C. L., Reines, F., Harrison, F. B., Kruse, H. W., and McGuire, A. D. (1956). Detection of the free neutrino: a confirmation. *Science*, 124(3212):103–104.

Domí nguez, A., Primack, J. R., Rosario, D. J., and et al., F. P. (2010). Extragalactic background light inferred from AEGIS galaxy-SED-type fractions. *Monthly Notices of the Royal Astronomical Society*, 410(4):2556–2578.

Donato, D., Ghisellini, G., Tagliaferri, G., and Fossati, G. (2001). Hard x-ray properties of blazars*. *A&A*, 375(3):739–751.

Dorigo Jones, J., Johnson, S. D., Muzahid, S., Charlton, J., Chen, H. W., Narayanan, A., Sameer, Schaye, J., and Wijers, N. A. (2022). Improving blazar redshift constraints with the edge of the Ly α forest: 1ES 1553+113 and implications for observations of the WHIM. , 509(3):4330–4343.

Finke, J. D., Razzaque, S., and Dermer, C. D. (2010). MODELING THE EXTRAGALACTIC BACKGROUND LIGHT FROM STARS AND DUST. *The Astrophysical Journal*, 712(1):238–249.

Fossati, G., Maraschi, L., Celotti, A., Comastri, A., and Ghisellini, G. (1998). A unifying view of the spectral energy distributions of blazars. , 299(2):433–448.

Franceschini, A., Rodighiero, G., and Vaccari, M. (2008). Extragalactic optical-infrared background radiation, its time evolution and the cosmic photon-photon opacity. *Astronomy &amp Astrophysics*, 487(3):837–852.

Fruck, C., Gaug, M., Zanin, R., Dorner, D., Garrido, D., Mirzoyan, R., and Font, L. (2014). A novel lidar-based atmospheric calibration method for improving the data analysis of magic.

Giavitto, G., Bonnefoy, S., Ashton, T., Backes, M., Balzer, A., Berge, D., Brun, F., Chaminade, T., Delagnes, E., Fontaine, G., Fuessling, M., Giebels, B., Glicenstein, J.-F., Gräber, T., Hinton, J., Jahnke, A., Klepser, S., Kossatz, M., Kretzschmann, A., Lefranc, V., Leich, H., Lenain, J.-P., Lüdecke, H., Lypova, I., Manigot, P., Marandon, V., Moulin, E., de Naurois, M., Nayman, P., Ohm, S., Penno, M., Ross, D., Salek, D., Schade, M., Schwab, T., Shiningayamwe, K., Stegmann, C., Steppa, C., Thornhill, J., and Toussnel, F. (2018). Performance of the upgraded h.e.s.s. cameras. In *Proceedings of 35th International Cosmic Ray Conference — PoS(ICRC2017)*. Sissa Medialab.

Gini, C. (1921). Measurement of Inequality of Incomes. *The Economic Journal*, 31(121):124–125.

Green, R. F., Schmidt, M., and Liebert, J. (1986). The Palomar-Green Catalog of Ultraviolet-Excess Stellar Objects. , 61:305.

Hess, V. F. (1912). Über Beobachtungen der durchdringenden Strahlung bei sieben Freiballonfahrten. *Phys. Z.*, 13:1084–1091.

Hillas, A. M. (1985). Cerenkov Light Images of EAS Produced by Primary Gamma Rays and by Nuclei. In *19th International Cosmic Ray Conference (ICRC19), Volume 3*, volume 3 of *International Cosmic Ray Conference*, page 445.

Li, T. P. and Ma, Y. Q. (1983). Analysis methods for results in gamma-ray astronomy. , 272:317–324.

Mangano, S. (2017). Cherenkov telescope array status report.

Mannheim, K. (1993). The proton blazar.

Mannheim, K. and Biermann, P. L. (1992). Gamma-ray flaring of 3C 279 : a proton-initiated cascade in the jet ? , 253:L21–L24.

Middei, R. and et al., M. P. (2023). Ixpe and multi-wavelength observations of blazar pg 1553+113 reveal an orphan optical polarization swing.

Middei, R., Perri, M., Puccetti, S., and Liodakis, e. a. (2023). IXPE and Multiwavelength Observations of Blazar PG 1553+113 Reveal an Orphan Optical Polarization Swing. , 953(2):L28.

Nigro, C., Sitarek, J., Gliwny, P., Sanchez, D., Tramacere, A., and Craig, M. (2022). agnpy: An open-source python package modelling the radiative processes of jetted active galactic nuclei. *Astronomy &amp Astrophysics*, 660:A18.

Park, N. (2015). Performance of the veritas experiment.

Rachen, J. P. and Mészáros, P. (1998). Photohadronic neutrinos from transients in astrophysical sources. *Phys. Rev. D*, 58:123005.

Richards, J. L. e. a. (2011). Blazars in the Fermi Era: The OVRO 40 m Telescope Monitoring Program. , 194(2):29.

Rybicki, G. B. and Lightman, A. P. (1979). *Radiative processes in astrophysics*.

Shakura, N. I. and Sunyaev, R. A. (1973). Black holes in binary systems. Observational appearance. , 24:337–355.

Urry, C. M. and Padovani, P. (1995). Unified Schemes for Radio-Loud Active Galactic Nuclei. , 107:803.

Acknowledgements

This research has made use of data from the OVRO 40-m monitoring program (Richards, 2011), supported by private funding from the California Institute of Technology and the Max Planck Institute for Radio Astronomy, and by NASA grants NNX08AW31G, NNX11A043G, and NNX14AQ89G and NSF grants AST-0808050 and AST- 1109911.
The MAGIC Collaboration is acknowledged for allowing the use of proprietary observational data. MAGIC results presented in this thesis have not undergone the internal review procedure of MAGIC publications.
The Tuorla Observatory blazar monitoring team is acknowledged for allowing the use of observational data reported in `https://users.utu.fi/kani/1m/`.
The *Fermi* team is acknowledged for allowing the use of observational data reported in `https://fermi.gsfc.nasa.gov/ssc/data/access/lat/LightCurveRepository/`.
The Swift team is acknowledged for allowing the use of observational data reported in `https://www.ssdc.asi.it/mmia/index.php?mission=swiftmastr`.

As I begin this section of acknowledgments, I want to express my gratitude to all the people who helped me along the way. This thesis wouldn't have been possible without their support.
In primis I would like to thank my parents for their constant involvement through my studies, even though we live far away from each other they have always shown their support and caring with meaningful gestures throughout my university career.
I am really thankful that my thesis made me meet amazing people from the MAGIC/CTA collaboration, both in Padova and Munich, and I am really glad to keep working with them. I hope this PhD will allow me to give back the support and the kindness that I've received from this group. In particular, I would like to thank Elisa and Davide, firstly for their constant help, but also for the meaningful relationship that we have build.
I am grateful to my friends in Palermo, from both high school and Telimar. In particular I would like to thank Fausto, Nicolò and Valerio for having always been there since I was 14.
At the university I was able to meet an amazing group of people, the *Mocha*. With them I have shared almost all the university experiences, in particular with Edoardo and Javier for being my flatmates.
Last but not least, I want to obviously thank her, my fantastic girlfriend Emma. You have been there as my source of stress ever since day 2, when you asked for an explanation of the hypotheses of a triangular matrix. I hope to continue sharing these moments with you. Thank you very much Emmi.